Microwave Surface Waves on Metasurfaces with Planar Discontinuities

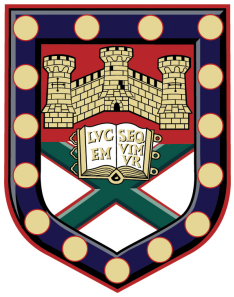

Simon James Berry

School of Physics

University of Exeter

A thesis submitted for the degree of

Doctor of Philosophy

April 2014

Microwave Surface Waves on Metasurfaces with Planar Discontinuities

Submitted by Simon James Berry to the University of Exeter as a thesis for the degree of Doctor of Philosophy in Physics
2014

I certify that all material in this thesis which is not my own work has been identified and that no material has previously been submitted and approved for the award of a degree by this or any other University.

Simon James Berry
2014

I would like to dedicate this thesis to my wonderful wife Hannah, thank you for all your loving support.

Acknowledgements

There are so many people that have contributed to helping me through my PhD that it will be difficult to mention everyone in all the detail they deserve. It has been an interesting journey that has taught me a lot about myself as well as the subject matter. First mention has to go to Hannah for sticking with me through all the ups and downs of completing my PhD, especially the writing up. For all of the 'not too much longer then I will become a normal person again' I am grateful for all your support and I hope you enjoy having your husband back again.

Obviously I wouldnt have learnt anything without the constant help and challenging I received from my supervisors, Roy Sambles and Alastair Hibbins. Thank you for constantly pushing me to become a better scientist and making me question everything I did. Your support and encouragement has been a great help, even at 8.30 on a Monday morning! It has been wonderful to work with people who have such a passion for the science that they study and I hope I never lose that.

Of course a PhD wouldnt be the same without all the fellow students, past and present. Thank you to all of you I have had the privilege to work with over the years. Thanks go to Helen, Tom, Celia, Matt B and Lizzy for welcoming me into G31 and putting up with all my foolish first year questions. It was nice to have such a helpful and patient bunch of people to help me settle in and enjoy many a G31 BBQ. To Al, as my fellow new starter, it would appear you are following me wherever I go! The joint thesis suffering, especially the page count, helped keep me motivated. Thanks go to the basement crew, who kept appearing at points throughout the day rubbing their eyes at the bright sunlight, for the continual banter that ensued between us. Joe, Laura, Ben, Ruth and Gareth thank you for providing significant amounts of sport and banter throughout our time together. I will enjoy coming back as the FF victor to see Joe when Man City lose the title.

A particular mention must also be given to Matt L and Ian for their help mixed with mild abuse throughout my PhD. Providing Matt with much entertainment discussing theology whenever he was bored will stick in my memory for a long time. Ian would simply roll his eyes at this point but patiently helped whenever I needed, even if the question was stupid. You never did learn not to 'go home' via the lab; it invariably meant you were there for much longer than planned. Also to Nick for always having the solution to my technical problems and never telling me to go away when I needed

something made post-haste.

Another fantastic group of people are the friends that I made outside of my work, most of them still kicking around in Exeter from our undergraduate days. Thank you to Si who kept me company throughout my undergraduate but decided not to join me in the adventure of a PhD. It has been great to have someone to chat through anything from physics to theology, usually over a pint. Thanks must go to Clare and Vicky for entertaining my wife on many an evening and being such a laugh, if a little silly at times! Will and Chris must also be mentioned as a great couple of guys to meet, chat, drink wine and usually off-load on, thanks a lot guys. Along with many other people who have supported and entertained me throughout my time at Exeter, Matt R, Rosie, Rosemary, Paul and Ellie, Bev and Alastair, Alex and many more.

Final thanks must go to my parents who have been incredibly supportive throughout my PhD both practically and emotionally. I hope I have made you proud.

Abstract

The work presented within this thesis details the experimental investigation of the surface waves supported on metasurfaces. Particular attention has been given to the reflection of these surface waves from planar discontinuities associated with these metasurfaces. Various experimental techniques have been developed throughout this work to characterise surface wave supporting metasurfaces. These include a new technique for measuring the dispersion of surface waves supported on metasurfaces, characterisation of the near-field associated with the surface waves, a device for launching planar phase front surface waves and finally a technique for measuring the surface wave reflection coefficient.

The dispersion of surface waves on a square array of square cross-section metal pillars has been fully characterised and compared to FEM modelling. The results show that a family of surface waves may be supported by pillar or crossed slit structures rather than just holes even though there is now no lowest cut-off frequency. A family of TM surface modes have been shown to exist with dispersions which asymptote to frequencies defined by the pillar heights (slit depth) and the refractive index of the material filling the slits.

Primarily this work focussed on the surface wave properties associated with a square array of square metal patches on a dielectric coated ground plane and a Sievenpiper 'mushroom' metasurface. The amplitude reflection coefficient of these surface waves has been studied for three distinct systems: Firstly for surface waves incident upon the termination of a these metasurfaces to free space, secondly for surface waves incident upon the interface between a dielectric coated and uncoated metasurface and thirdly for surface waves incident on the boundary between two metaurfaces.

The reflection coefficient of surface waves incident upon the termination of the metasurface to free space is found to increase significantly with the confinement of the surface mode. This confinement, and therefore the form of the reflection coefficient, is significantly different for the two metasurfaces considered due to their dispersions. This increase in the reflection coefficient is caused by both the momentum mismatch of the surface wave compared to the freely propagating modes and the different field distributions of the two modes.

The reflection coefficient of surface waves incident upon the boundary between a coated and uncoated metasurface has been experimentally characterised for the metal

patch array and Sievenpiper 'mushroom' metasurfaces. It is shown that the addition of a thin, significantly subwavelength, dielectric overlayer onto the metasurface vastly perturbs the surface wave dispersion. The reflection coefficient of the surface waves is found to depend on the dispersion of the mode supported on the coated and uncoated metasurface and the overlayer thickness. Most noticeably the thickness of the overlayer, by comparison to the surface wave decay length, has a significant effect on scattering to free space associated with the surface wave reflection.

The final system considered was designed to investigate the impedance approximation, often used to describe metasurfaces, and found it to be an incomplete description of the surface waves supported on the metasurfaces used within this study. In the impedance approximation the two surfaces considered are said to be 'impedance matched' at certain frequencies. It is demonstrated that the failure of the impedance approximation to accurately describe this system is due to the behaviour of the electric field within the metasurfaces. These are not analytically described in the impedance approximation and are required for an accurate description of the surface waves supported on these metasurfaces.

Contents

Contents

List of Figures

Chapter 1

Introduction

1.1 Aim of Research

Surface waves on metal-dielectric interfaces have been extensively studied throughout the electromagnetic (EM) spectrum starting with the discovery of the Wood's anomaly in 1902 [1]. Although this optical phenomena wasn't full explained until much later [2] surface waves at microwaves were extensively studied during this period [3–9]. The behaviour of these surface waves at microwave frequencies is dominated by the high conductivity of metals in this frequency range which leads to the exclusion of the electric field from within the metal. As such planar metal surfaces are considered not to support bound surface waves at microwave frequencies. This has been overcome by the addition of structure to the planar metal [5, 10–12], a phenomenon which has been experimentally investigated with a resurgence of interest [13–19] occurring after the prediction of tightly bound microwave surface waves with properties similar to those found at optical frequencies [20].

Controlling these surface waves has been of great interest in recent years in many new areas of technology including applications for surface wave suppression [21–25], improved antenna performance [25–31], wireless communication technologies and microwave circuits [24, 29, 30, 32] among others. The radar cross-section of a stealth aircraft has a significant contribution from surface wave mediated processes. Therefore, since the radar cross-section of military aircraft is a primary factor in their mission performance [33], a significant amount of research into non-reflecting surface wave absorbing materials has been performed [34, 35] (and references therein).

In this thesis the properties of these surface waves supported on thin structured surfaces, known as metasurfaces, have been experimentally characterised. Particular attention has been paid to developing a system capable of measuring the local electric field associated with these surface waves and determining their interaction with planar

interfaces in the metasurface.

1.2 Thesis Outline

The work in this thesis focusses on the experimental investigation of the reflection, transmission and scattering of microwave surface waves supported on metasurfaces. Initially a new type of surface wave supporting structure is characterised to determine the properties of the surface waves supported by such a structure. Secondly the reflection and radiation scattered to free space from the termination of a metasurface is experimentally determined. The techniques developed in characterising the surface wave and radiation scattered to free space are then applied to measuring the reflection, transmission and scattering of a surface wave incident on a dielectric overlayer and finally the interface between two metasurfaces.

A summary of the work previously undertaken in this research area is presented in Chapter 2, along with a discussion of the background theory dictating the behaviour of surface waves on metasurfaces. In particular the dispersion of the surface waves supported on the metasurfaces used within this thesis and their associated properties are fully discussed. A discussion of the impedance description of surface wave supporting metasurfaces and the effect of the lattice on the surface dispersion is performed.

Details of the experimental methods developed to characterise these surface waves and determine their reflection, transmission and scattering from discontinuities is presented in Chapter 3. Also theory dictating the detection of these microwave surface waves is explored and presented as it pertains to the methods employed within this study. A brief explanation of the techniques employed within the finite element method modelling to design the metasurface structures and determine the expected reflection coefficient is also given. The techniques developed to excite planar phase front surface waves and fully characterise the near-field associated with the surface waves are discussed.

In Chapter 4 the surface waves supported on a square array of square cross-section metallic pillars is experimentally characterised. Particular attention is given to the azimuthally independent nature of the modes supported due to the symmetry of the system. The dispersion of these surface modes is experimentally investigated using a new technique involving the use of parabolic mirrors to collimate the surface waves.

The reflection and scattering to free space of a surface wave incident upon the termination of a metasurface, presented in Chapter 5, is shown to be highly frequency dependent. The characterisation of the amplitude reflection coefficient is performed along with the form of the scattered radiation. The amplitude reflection coefficient is compared to that obtained from both an analytical model, utilising the impedance

approximation, and finite element method modelling. The validity of the impedance approximation in describing the metasurfaces considered is discussed. It is also shown that the orientation of the coaxial probe has a significant effect on the measured scattered radiation.

Investigation of the reflection, transmission and scattering to free space of a surface wave incident upon a finite thickness dielectric overlayer on a metasurface is presented in Chapter 6. The reflection of a surface wave incident upon the dielectric overlayer on a metasurface consisting of a square array of square metal patches is measured along with a dielectric overlayer on a Sievenpiper 'mushroom' structure. For the metallic patch array the reflection coefficient is studied both as a function of frequency, where the waveguide-like nature of the surface mode has significant effect, and as function of the overlayer thickness. The surface wave reflection coefficient for the dielectric overlayer on the Sievenpiper 'mushroom' array is explored as a function of frequency. It is shown that the addition of a dielectric overlayer leads to a frequency band where transmission as a surface wave is forbidden, particular attention is paid to this phenomena.

The final experimental results are presented in Chapter 7, where the reflection, transmission and scattering is investigated for the interface between two surface wave supporting metasurfaces. The impedance description traditionally used to describe surface wave supporting structures is investigated by designing a surface which is 'impedance matched' at a single frequency. At this condition the surface wave may be expected to experience no reflection when incident upon the discontinuity. However it is shown that for a metasurface matching of the impedance is not sufficient to eliminate the surface wave reflection, since the distribution of the electric fields within the two metasurface unit cells is significantly different in the two metasurfaces at the 'impedance matched' condition.

Finally in Chapter 8 the conclusions from this thesis are presented along with suggestions for future extension of this work.

Chapter 2

Surface Waves Supported on Metasurfaces

2.1 Introduction

In this thesis a study of surface wave reflection, transmission and scattering at microwave frequencies has been performed. Surface wave properties at microwave frequencies are predominately determined by surface structuring since all metals can usually be considered as perfect conductors. Subwavelength surface structure can confine the otherwise unconfined surface wave, often referred to as a surface current, by introducing a resonance of the electromagnetic (EM) field due to the structure. Recently the study of surface waves supported by structured surfaces has been revisited [20] and a resurgence of interest in this area has taken place [19, 36, 37]. In this chapter a general understanding of microwave surface waves is presented, with a particular focus on the effect of surface structure on the surface wave dispersion. In particular the surface wave properties of the metasurfaces used in this thesis are discussed.

2.2 Surface Waves Along Metallic Surfaces at Microwave Frequencies

The guiding of surface waves along a planar interface between dissimilar media has been studied as far back as 1902 [1, 3, 38, 39] and in all frequency bands ranging from the radio to the optical regime [40]. At optical frequencies guided modes supported at the interface of a metal and a dielectric are referred to as surface plasmon polaritons (SPP) whilst at radio frequencies surface structuring or dielectric coatings on the planar metallic surface are required to confine surface waves in a manner similar to

the localisation found at optical frequencies. It will be shown that guided modes can be supported at microwave frequencies on both a dielectric coated ground plane, section 2.3.1, and structured metallic surfaces, section 2.3.2. These confined modes are in contrast to the modes supported on a bare and unstructured metallic ground plane at microwave frequencies which are considered to be unconfined in the dielectric half space above.

It is possible to engineer the dispersion of surface modes at microwave frequencies by introducing subwavelength structure to the interface [10, 15, 20, 41–49]. An example of this is presented in which subwavelength corrugations of a metallic ground plane are shown to lead to a tightly confined mode close to a microwave frequency dictated by its surface geometry, section 2.3.2. A material whose subwavelength structuring determines its properties and whose thickness is a single unit cell is termed a metasurface. These metasurfaces have applications in controlling both surface waves and free space EM radiation. The unit cell of a metasurface must be significantly smaller than the wavelength of the radiation incident upon the metasurface in order for it to be seen as a homogeneous medium.

Surface modes at microwave frequencies were first investigated in the early 1900's and a comprehensive review article was published in 1953 [50] along with other more detailed sub-field reviews [51, 52]. The structures considered included coating a metallic ground plane with a dielectric and subwavelength corrugation of the metallic ground plane [5–7, 12, 53, 54]. Further investigation into the guided modes supported on a structured surface was performed by Cutler [12] and more recently a new metasurface was proposed which mimics optical plasmonics at microwave frequencies [20]. Low frequency plasmonic surfaces were quickly realised experimentally at both microwave [14] and terahertz frequencies [55–59]. Some of these results will be discussed in due course, but in summary, they all rely on a resonant surface behaviour, somewhat analogous to the resonant surface plasma of electrons in the plasmonic equivalent.

The experimental investigation into low frequency plasmon-like surface modes used an array of square waveguides [14]. These surface modes rely on the penetration of the electric and magnetic fields into the waveguides below their fundamental resonant frequency, known as the 'cutoff' frequency. The metallic boundary conditions imposed by the sides of the interior of the waveguide exclude propagating fields from existing within the waveguide below its fundamental resonant frequency. For frequencies below this cutoff the fields which penetrate within the waveguide are therefore exponential in character, mimicking the penetration of fields into a metal at optical frequencies. This exponentially decaying field penetration at microwave frequencies modifies the boundary condition of the surface such that the surface wave has a comparable dispersion to that of a SPP. This phenomenon inspired a plethora of research into surface wave

supporting metasurfaces [16, 17, 40, 60–70] two of which have been used extensively in this study [60, 71].

In this chapter a discussion of the physical principles dictating the behaviour of surface waves on metasurfaces is presented along with the behaviour of the surface modes supported on the particular structures employed within this thesis. A general derivation of surface waves guided by an interface is presented in section 2.3 with an extension to include the properties of surface waves guided by a dielectric overlayer. The concept of surface structure, section 2.3.2, is introduced along with its applications to the dispersion of a surface wave supported by metasurfaces, with particular attention paid to the structures used in this thesis, sections 2.5.2 and 2.5.3. The topic of this thesis concerns the propagation of surface waves on metasurface structures containing planar discontinuities. Particularity the reflection of these discontinuities will be studied and therefore an overview of the previous work undertaken on analytically determining the reflection coefficient of a surface wave incident upon a reflection discontinuity is presented.

2.3 Surface Waves at a Planar Interface

A derivation of the field solution for a surface wave can be made by considering the scattering of an EM wave incident onto a planar interface [72], figure 2.1. Consider a planar interface in the xy-plane at $z = 0$ between dissimilar media. The region above the interface, $z > 0$, is considered to be an isotropic material with relative material parameters ε_1 and μ_1 and the region below the interface, $z < 0$, to be an isotropic material with relative material parameters ε_2 and μ_2. A transverse magnetic (TM) polarised wave incident in the xz-plane at some angle θ_i to the z-axis possesses field components H_y, E_x, and E_z and a wavevector $k = \sqrt{\varepsilon_1\mu_1}k_0 = n_1k_0$ where $n_j = \sqrt{\varepsilon_j\mu_j}$ is the refractive index of region j and k_0 is the free-space wavevector, figure 2.1.

The reflection coefficient of such a system can be determined by the Fresnel equations written in terms of impedance, equation 2.1, which are simply derived from the continuity of fields across the interface between the two regions [73]. The bound modes of any system are determined by poles in the scattering matrix, which for a planar interface system are equivalent to poles in the reflection coefficient, i.e. when the denominator of equation 2.1 is equal to zero [74].

$$r_{12} = \frac{Z_2 - Z_1}{Z_2 + Z_1} \tag{2.1}$$

where r_{jk} is the amplitude reflection coefficient for a wave incident from region j to region k and Z_j is the relative impedance of the region indicated by the subscript. The

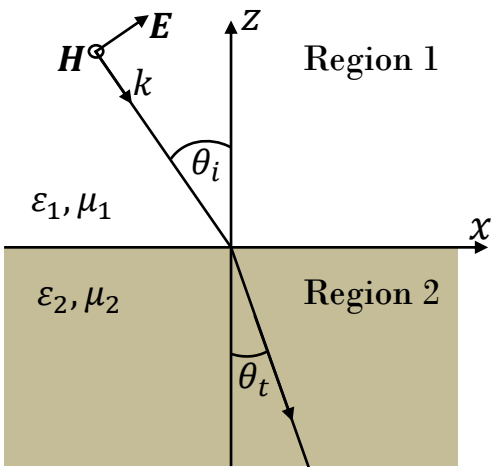

Figure 2.1: A TM polarised wave incident in the xz-plane onto a planar interface between two dissimilar media, with relative permittivities and permeabilities ε_1, μ_1 and ε_2, μ_2, for regions 1 and 2 respectively.

impedance is defined as the ratio of the E-field to the H-field which at the interface is simplified from the bulk impedance definition ($Z_{\text{BULK}} = \mathbf{E}/\mathbf{H}$), to take into account that only a single component of the total E-field is in the plane of the interface, E_x. Therefore the surface impedance can be written as $Z_{\text{SURF}} = E_x/H_y$ for TM waves. The surface impedance is simply a modified version of the bulk impedance which differs by the cosine of the incident angle, equation 2.2. This can be rewritten in terms of the wavevector of the incident field, 2.3.

$$Z_{\text{SURF}} = Z\cos(\theta) = \sqrt{\frac{\mu_r}{\varepsilon_r}}\cos(\theta) \tag{2.2}$$

$$Z_{\text{SURF}} = \sqrt{\frac{\mu_r}{\varepsilon_r}}\frac{k_z}{nk_0} = \frac{k_z}{\varepsilon_r k_0} \tag{2.3}$$

where ε_r and μ_r are the relative permittivity and permeability of the material respectively and $n^2k_0^2 = k_x^2 + k_z^2$. Substituting this into equation 2.3 for k_z we can solve the equation for the pole in the reflection coefficient, $Z_2^2 = Z_1^2$ where these are the surface impedances:

$$\frac{n_2^2k_0^2 - k_x^2}{\varepsilon_2^2}\left(\frac{1}{k_0}\right)^2 = \frac{n_1^2k_0^2 - k_x^2}{\varepsilon_1^2}\left(\frac{1}{k_0}\right)^2 \tag{2.4}$$

Rearranging for a solution to the in-plane wavevector, k_x, as a function of the angular frequency, ω, and the material properties of the two regions the generalised

dispersion for a bound surface mode is found:

$$k_x = \pm k_0 \sqrt{\frac{\varepsilon_1 \varepsilon_2 (\varepsilon_1 \mu_2 - \varepsilon_2 \mu_1)}{\varepsilon_1^2 - \varepsilon_2^2}} \tag{2.5}$$

If region 1 is vacuum and region 2 is a metal with relative permittivity ε then we obtain the dispersion for a TM surface wave on a metal surface, equation 2.6.

$$k_x = \pm k_0 \sqrt{\frac{\varepsilon}{\varepsilon + 1}} \tag{2.6}$$

The dispersion of these bound surface modes is determined by the dispersion of the material parameters which describes how the photon interacts with the material. In the case of the metasurfaces considered later in this chapter the dispersion of the effective material parameters describes how the mircowaves interact with the metasurface structure. Equation 2.5 is the general equation for the bound surface modes of a single planar interface system, and a similar analysis may be performed for a N-layer system since the Fresnel equations are well established for a multilayer system. Whilst the pole of the reflection coefficient is readily obtained analytically for a single planar interface system this analysis is not possible for the many interface system we will consider later.

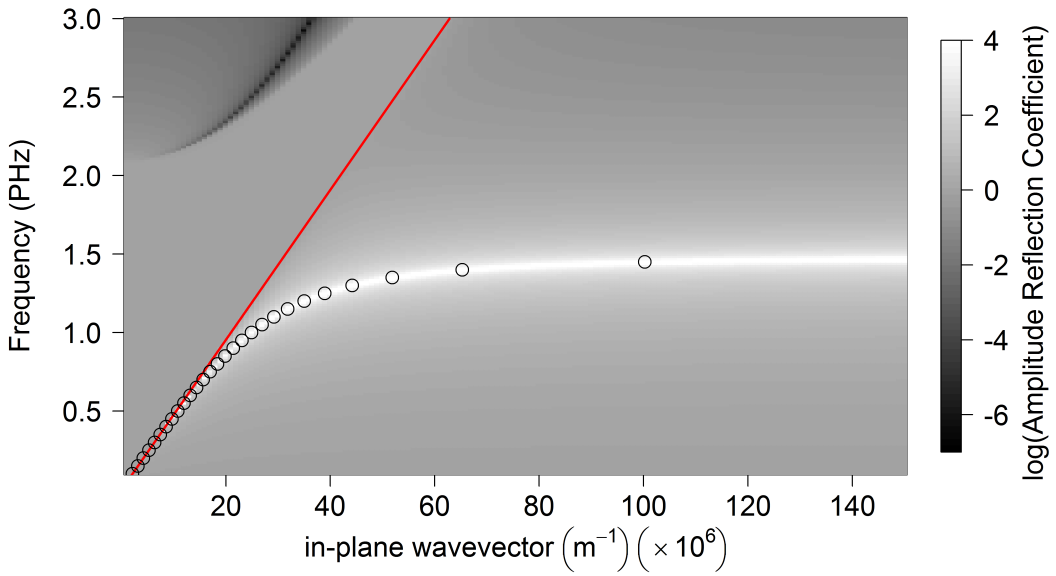

Figure 2.2: Comparison of the SPP dispersion on a silver-vacuum interface calculated using an analytical solution (black circles) with the pole in the reflection coefficient, plotted on a log scale (greyscale), obtained numerically. The light line is also shown for context (red line).

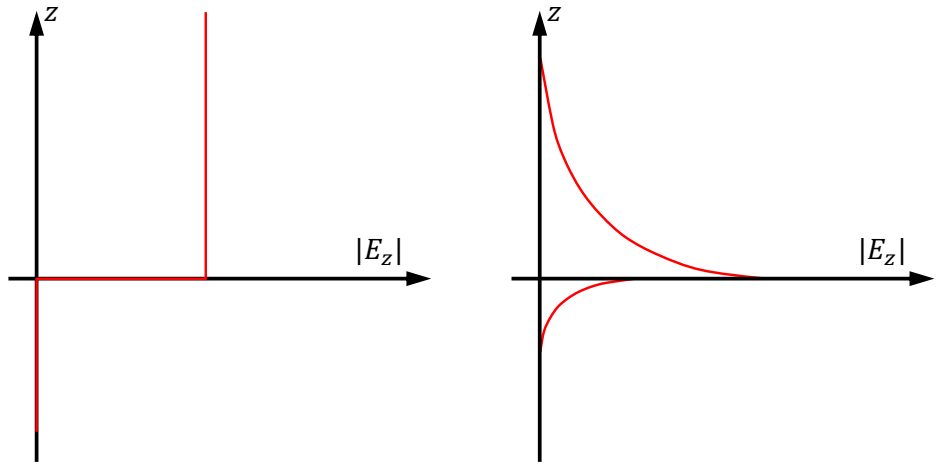

(a) Microwave Frequencies (b) Optical Frequencies

Figure 2.3: Schematic of the electric field normal to the metal dielectric interface at both microwave, where the mode is on the light line and photon-like, and optical frequencies, where the mode is away from the light line and plasmon-like.

A numerical solution is still possible for such a system, the reflection coefficient is determined and the dispersion of the bound modes determined from the maxima in the reflection coefficient. Beyond the light line the amplitude of the reflection coefficient clearly has no physical meaning as the 'incident' wave is decaying and we are only interested in the position of the maxima.

Verification of this method can be performed by comparing the analytical solution for a single interface system with the numerical solution for the same system. This was done for a surface plasmon polariton (SPP) supported on the interface between silver, modelled as a Drude metal, and vacuum in the optical regime where the SPP dispersion changes rapidly, figure 2.2. The greyscale shows the numerically determined reflection coefficient, where the bright band shows the solution for the SPP dispersion whilst the black circles are the analytical solution for the same system. The light line shows the maximum in-plane momentum possible for a freely propagating photon. The silver has been modelled using the form of the Drude model found in equation 2.7 with a plasma frequency of $\omega_\mathrm{p} = 1.32 \times 10^{16}$ Hz and a relaxation time of $\tau = 1.45 \times 10^{-14}$ s.

$$\varepsilon = 1 - \frac{\omega_\mathrm{p}^2}{\omega^2 + i\omega\tau} \tag{2.7}$$

where ω is the angular frequency of the EM radiation.

The dispersion of the SPP is on the light line at microwave frequencies and diverges from it at optical frequencies. This leads to a mode that is unconfined at microwave

frequencies. This is because the electric field is entirely excluded from the metal at these frequencies since it can be considered to act as a Perfect Electric Conductor (PEC), figure 2.3. However as the frequency of the radiation increases the PEC approximation becomes invalid and the field can penetrate into the metal with a finite decay length. This decay length induces a decaying field above the interface, to satisfy the boundary condition, leading to a bound mode at optical frequencies, figure 2.3. This occurs as the SPP dispersion diverges from the light line, with the confinement of this mode increasing the further the mode sits from the light line.

2.3.1 Guided Waves Supported by a Dielectric Coated Ground Plane

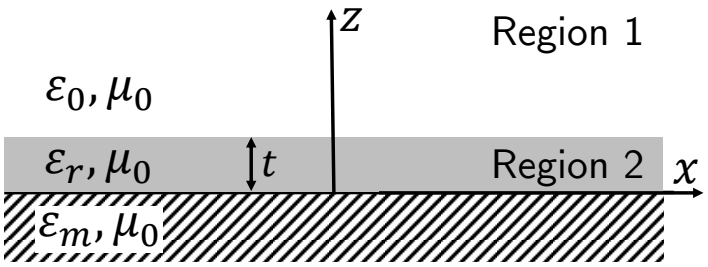

Figure 2.4: Dielectric coated metallic ground plane system, in which the dielectric coating has thickness t and relative permittivity ε_r.

Investigation of the surface waves supported on a dielectric coated ground plane at microwave frequencies is performed by extending the method used in the previous section. However as previously stated it is now not possible to solve this system analytically and as such a numerical approach will be taken. The amplitude reflection coefficient for a planar interface system with three regions is derived analytically in Appendix A equation A.4, and is given below:

$$r_{13} = r_{12} + \frac{t_{12}t_{21}r_{23}exp(2i\alpha)}{1 - r_{21}r_{23}exp(2i\alpha)} \tag{2.8}$$

Here t_{jk} is the amplitude transmission coefficient from layer j to layer k and r_{jk} is the equivalent amplitude reflection coefficient. Unlike the single interface system previously discussed it is not possible to analytically determine the poles of the scattering matrix. However it is still possible to determine the reflection coefficient by numerically solving the single interface reflection and transmission coefficients for a matrix of k_x and ω.

The dispersion of a surface mode supported on a metal ground plane coated with a lossless dielectric is obtained using this method, and is shown in figure 2.5. The chosen system has a dielectric overlayer with permittivity $\varepsilon_r = 2.2$ and a thickness of

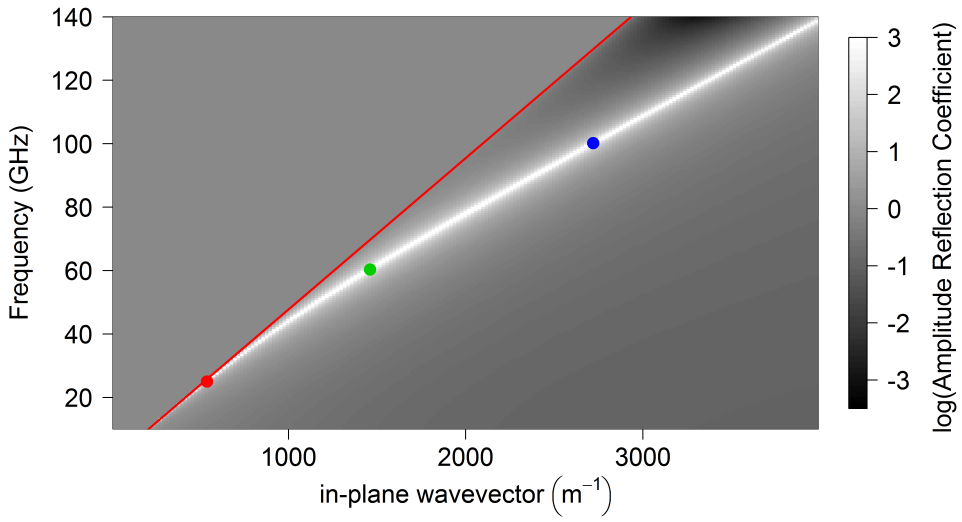

Figure 2.5: Amplitude reflection coefficient for a thin dielectric overlayer obtained numerically, plotted on a log scale (greyscale). The pole in the reflection coefficient shows the dispersion of the bound surface mode for this system. The light line is also shown for context (red line). Coloured circles indicate the position of the simulated fields in figure 2.6.

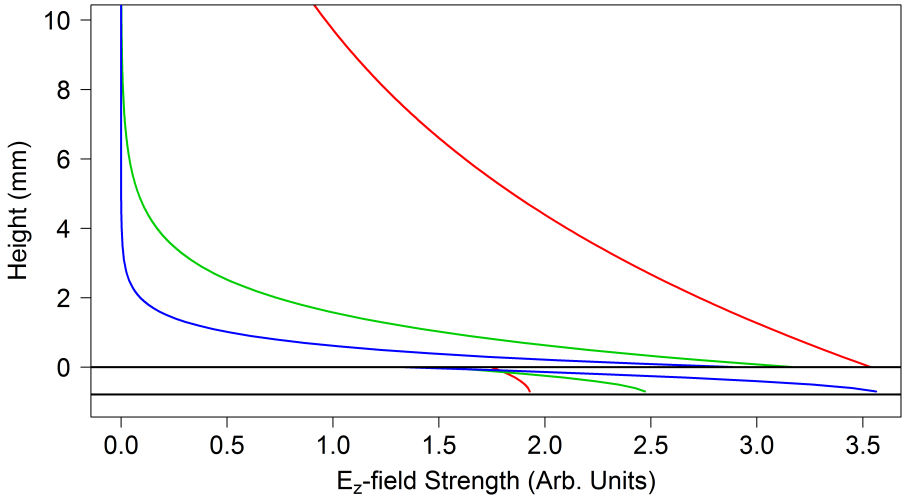

Figure 2.6: Simulated E_z field strength as a function of the height above the dielectric layer shown in figure 2.4 for three different frequencies shown in figure 2.5. The black lines indicate the position of the interface between the metallic ground plane and the dielectric overlayer and the half space above. The frequencies of the modes are approximately 25 (red), 60 (green) and 100 GHz (blue).

$t = 787\ \mu$m, corresponding to the printed circuit board (PCB) core material parameters, with the loss ignored, used later in this study. This illustrates that at low frequencies, where the optical thickness of the dielectric is much smaller than the wavelength, the dispersion is approximately that of a grazing photon. As the optical thickness of the dielectric increases the dispersion of the mode diverges from the light line. The limit of this divergence is given by the dispersion of a grazing photon supported at the planar interface of the metal and dielectric half space with the material properties of the dielectric overlayer. This dispersion of the light line of the infinite dielectric metal interface is linear but with a shallower gradient modified from the vacuum case by the refractive index of the dielectric.

The calculation of the fields within the dielectric overlayer and half space above is possible from the in-plane wavevector and the frequency of the radiation, both of which are extracted from the calculated amplitude reflection, figure 2.5. The electric field perpendicular to the interface, E_z, is extracted at the positions indicated by the red, green and blue points and plotted in the corresponding colours in figure 2.6. The confinement of the field in the z-direction increases as the mode diverges from the light line since the decay length away from the interface is inversely proportional to the imaginary part of k_z and that $k_0^2 = k_x^2 + k_z^2$, as the in-plane wavevector increase the magnitude of the imaginary part of k_z increases and hence mode confinement increases. Figure 2.6 shows that the electric field strength within the dielectric overlayer also increases as the mode diverges from the light line which leads to a greater proportion of the power flowing within the dielectric overlayer.

2.3.2 Surface Waves on a Corrugated Plane

Surface waves supported on a structured ground plane form the basis for understanding metasurface structures, one of the simplest forms of which is a corrugated metallic plane [5, 6, 75], figure 2.7. The modes supported on a corrugated metallic plane are considered here for the case where the metallic corrugations are considered to be infinitely thin and invariant in the y-direction, with a height, d, and a spacing, S.

The solution for a TM surface wave propagating in the x-direction is considered; this mode has a single component of the magnetic field, H_y, from which the two components of the electric field, E_x and E_z, can be derived. Since the structure is periodic the form of the H_y field is dictated by Floquet's theorem [76]. Above the corrugations, $z > d$, the form of H_y is given by:

$$H_y = \sum_{N=-\infty}^{\infty} A_n \exp\left[ik_z z + i\left(k_x + \frac{2N\pi}{S}\right)x\right] \tag{2.9}$$

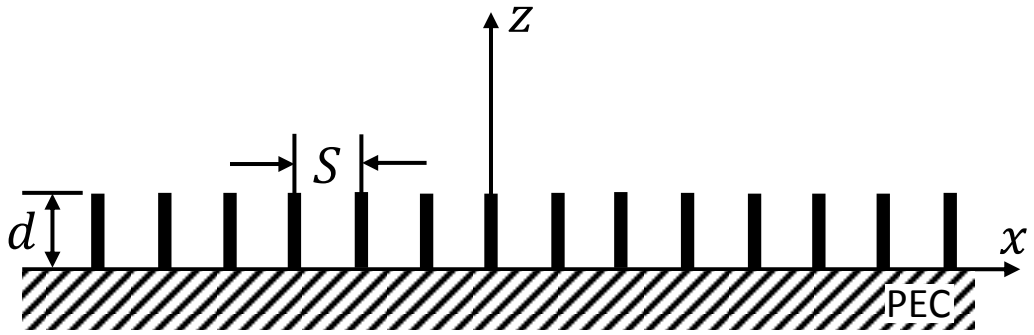

Figure 2.7: Schematic diagram of a corrugated metallic ground plane with infinitely thin perfectly conducting walls with height d spaced distance S apart.

where $k_z^2 = k_0^2 - (k_x + 2N\pi/S)^2$. In the corrugations, $0 < z < d$, the E_z component of the electric field must vanish at the corrugations and the E_x component must vanish at the ground plane, these boundary conditions dictate the form of H_y. Therefore within the corrugated region the magnetic field is:

$$H_y = \sum_{N=0}^{\infty} B_n \cos\left(\frac{N\pi x}{S}\right) \cosh(k_z z) \tag{2.10}$$

where $k_z^2 = k_0^2 - (N\pi/S)^2$. If we consider subwavelength corrugations, such that S is small by comparison to the wavelength, the only propagating mode supported between the corrugations is the transverse electromagnetic (TEM) mode, where $k_z = k_0$. All other k_z solutions are imaginary, forcing the field to decay exponentially in the negative z-direction. This behaviour is seen clearly in equation 2.10 since $k_z^2 = k_0^2 - (N\pi/S)^2$ if S is small enough then when $N = 1$ k_z will be purely imaginary and only the $N = 0$ mode, i.e. the TEM mode, will propagate between the plates.

A solution for k_x of the surface wave supported on top of the corrugations may be found by considering a semi-infinite parallel plate system, figure 2.8, where the spacing of the plates is S but the plates are infinite in the negative z-direction. Since the condition for a bound surface mode is that above the corrugations the field decays exponentially in the positive z-direction, $(k_x + 2N\pi/S)^2 > k_0^2$, the reflection coefficient at the interface for the parallel plate system must be 1. Since the reflection coefficient is equal to 1 a perfect standing wave is set up within the parallel plates and the E_x field vanishes at spacings of $\lambda/2$. A conducting ground plane may be placed at these positions and the field will be unperturbed, in this way the corrugated plane has been recovered and shows that this system is suitable for determining the value of k_x for the surface wave.

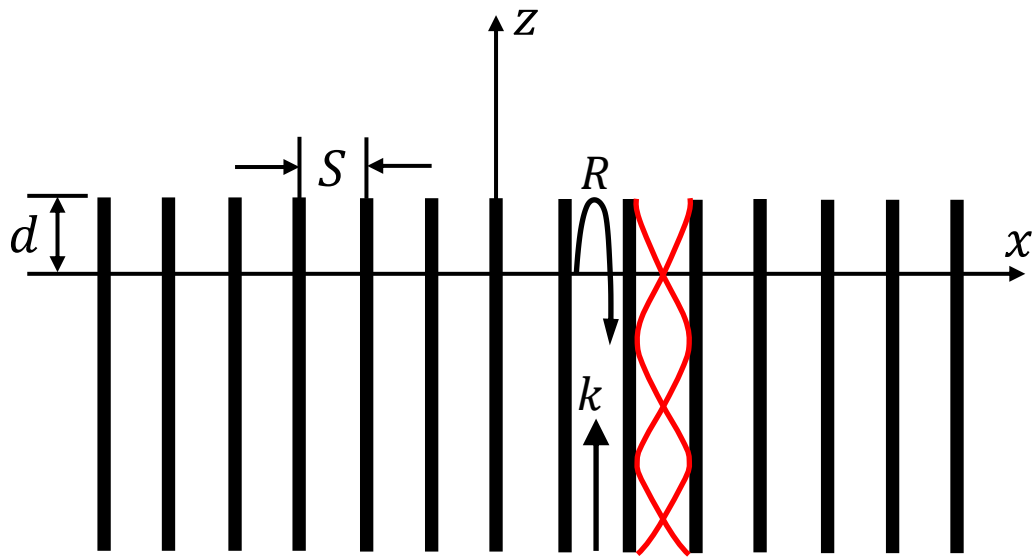

Figure 2.8: Schematic diagram of an array of parallel plate waveguides with infinitely thin perfectly conducting walls with height d in the positive z-direction and infinite in the negative z-direction, with a width S between the perfectly conducting walls.

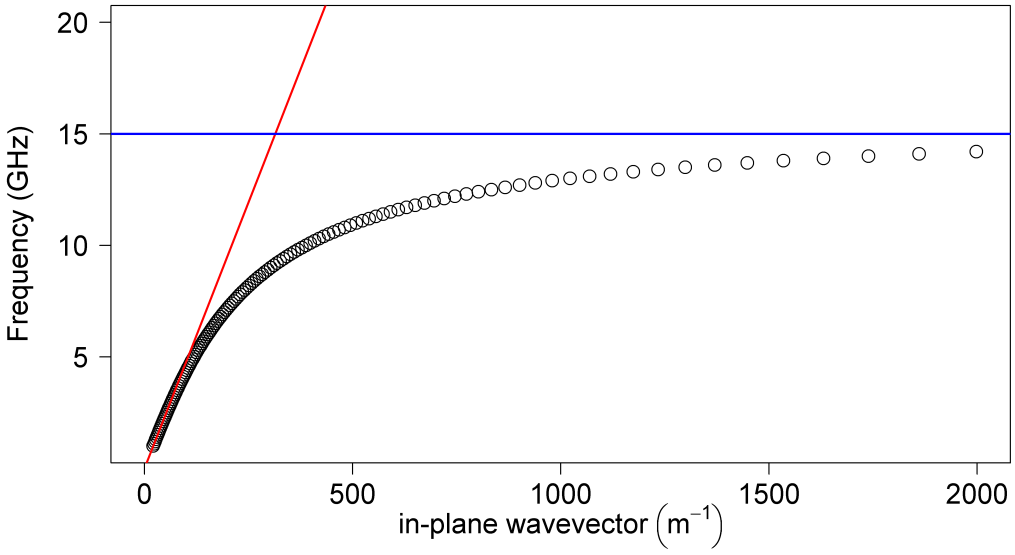

Figure 2.9: Fundamental surface mode dispersion for a corrugated metallic ground plane (black points), where $d = 5$ mm and $S = 1$ mm (figure 2.7), with the light line (red line).

The reflection coefficient of the TEM mode incident upon the termination of the parallel plate waveguides is defined by $R = e^{-i\phi}$. Therefore we can define the phase difference between the wave incident upon the boundary and the reflected wave at a distance, d, from the interface $\theta = \phi + 2k_0 d$. The conducting plane must be placed at distance d such that $\theta = N\pi$, since the electric field will vanish when the incident and reflected TEM waves are completely out of phase, and therefore:

$$2k_0 d + \phi = M\pi, \quad M = 1, 3, 5... \tag{2.11}$$

The reflection coefficient for a terminated parallel plate system can be calculated, however it is beyond the scope of this discussion to present it here [77]. For spacings, S, less than approximately $0.2\lambda_0$ the phase of the reflection, ϕ is given by:

$$\phi = 2\left(\tan^{-1}\left(\frac{k_0}{-ik_z}\right) - k_0\frac{S}{\pi}\ln(2)\right) \tag{2.12}$$

Substitution of 2.12 into 2.11 and solving for k_z gives:

$$-ik_z = k_0 \tan\left[k_0\left(d - \frac{S}{\pi}\ln(2)\right)\right] \tag{2.13}$$

Solutions for the in-plane wavevector can then be trivially determined by:

$$k_x = \sqrt{k_0^2 - k_z^2} \tag{2.14}$$

The dispersion of a surface wave guided by such an interface can now be calculated, figure 2.9, with a highly confined surface wave supported close to the $d = \lambda_0/4$ condition. At low frequencies where the depth, d, of the corrugations is much smaller than the wavelength of the radiation the surface mode is almost unconfined and can be considered to be a grazing photon. The confinement of the mode increases as the mode disperses from the light line and both the phase and group velocities of the mode decrease. These properties are typical of a surface wave supported on a metasurface at microwave frequencies.

2.4 Impedance Description of a Surface

The propagation of a surface wave on a metasurface is often described using a description of the surface impedance [78–81]. Here we will briefly introduce the surface impedance approximation used to calculate the surface wave reflection coefficient later in this thesis in chapters 5 and 7. The analysis will show that a TM surface wave is supported on a surface with an inductive surface impedance and will demonstrate how

this impedance approximation may be derived from the dispersion relation.

Consider a planar interface at $z = 0$ that is in the xy-plane which has a normalised surface impedance given by, $Z_s = R_s + i\chi_s$. The surface impedance may be normalised to the impedance of free space, Z_0. Since we are considering TM surface waves only the magnetic field has a single component, H_y, which can be written in the following form for the region above the interface, $z > 0$:

$$H_y = A\exp(ik_z z - ik_x x) \tag{2.15}$$

where $k_0^2 = k_x^2 + k_z^2$. The two electric field components, E_x and E_z, are easily derived from Maxwell's equations:

$$i\omega\varepsilon_0 E_x = \frac{\partial H_y}{\partial z} \tag{2.16}$$

$$i\omega\varepsilon_0 E_z = -\frac{\partial H_y}{\partial x} \tag{2.17}$$

The impedance of the incident inhomogenous plane wave is described as:

$$Z = \frac{\mathbf{E}}{\mathbf{H}} \tag{2.18}$$

In the plane of the interface only two components of the field are projected onto the xy-plane, H_y and E_x, so the surface impedance at $z = 0$ is given by:

$$Z_S = \frac{E_x}{H_y} = \frac{k_z}{\omega\varepsilon_0} = \frac{k_z}{k_0} Z_0 \tag{2.19}$$

Which must be equal to the incident wave impedance at $z = 0$ to satisfy the boundary condition. Here k_z/k_0 is the normalised wave impedance for the incident field and is therefore equated to the normalised surface impedance to give the solution for k_z:

$$k_z = k_0 Z_s = k_0 R_s + ik_0\chi_s \tag{2.20}$$

The in-plane wavevector is trivial to determine with the knowledge of k_z:

$$k_x = \sqrt{k_0^2 - k_x^2} = k_0\sqrt{1 + \chi_s^2 - R_s^2 - 2iR_s\chi_s} \tag{2.21}$$

Equation 2.20 indicates that in order for the field to exponentially decay in the z-direction normal to the interface the value of χ_s must be positive and R_s should be small. For the surfaces considered in this thesis it is assumed that the surface is lossless and therefore $R_s = 0$. When this is the case the equation for the in-plane wavevector

k_x reduces to:

$$k_x = k_0\sqrt{1+\chi_s^2} \tag{2.22}$$

It is clear that the impedance of the surface can be readily obtained from the dispersion of the mode, equation 2.22, if the surface is assumed to be lossless. The surface mode can also be characterised by considering the phase velocity of the wave with reference to the speed of light, an equivalent description to the refractive index, known as the mode index, n:

$$n = \frac{c}{v_p} = \frac{ck_x}{\omega} = \sqrt{1+\chi_s^2} \tag{2.23}$$

The surface impedance description can be used to describe the modes supported on the metasurfaces presented within this thesis and in doing so an analytical solution for the reflection coefficient of a surface mode incident upon a surface discontinuity is possible [82]. This thesis will consider the application of this surface impedance approximation to the problem of determining the reflection coefficient of a surface wave incident upon a variety of metasurface discontinuities.

2.5 Surface Waves Supported on Metasurfaces

In this section we will present an overview of the surface waves supported on the metasurfaces used in this thesis. Within this thesis a new class of metasurface has been experimentally characterised in chapter 4 and two structures, whose microwave surface wave properties are well known, have subsequently been employed; the first is a square array of square metallic patches on a dielectric coated ground plane [44] and secondly a Sievenpiper 'mushroom' array [71]. The surface wave properties of these metasurfaces is presented here along with the concept of a Brillouin Zone (BZ) boundary and its effect on the surface wave dispersion of these structures.

2.5.1 Brillouin Zone Boundaries

The BZ is the primitive unit cell of a lattice in reciprocal space, the boundaries of which contain points of high-symmetry. The first BZ boundary is formed by the perpendicular bi-sectors of the lattice vectors between nearest neighbours in reciprocal space followed by the next-nearest neighbours and so on, this is known as the Wigner-Seitz method [83]. All of the metasurfaces used within this thesis have square unit cells arranged in a square lattice and as such their reciprocal space lattice is also square. Therefore discussion of the BZ shall be limited to that in a square reciprocal lattice and its effects

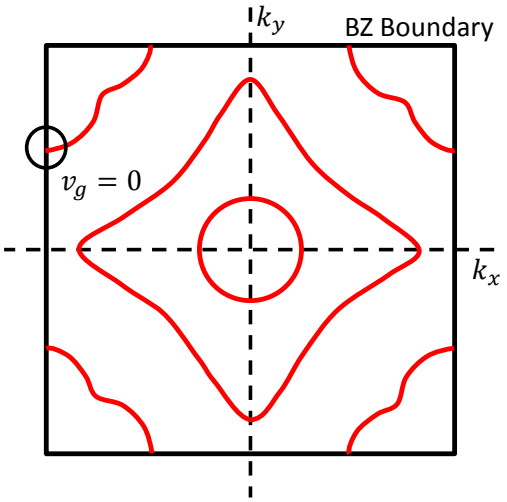

Figure 2.10: Schematic of the BZ boundary (black line) of a square lattice with example mode shapes shown (red lines) with increasing frequency as the mode approaches the BZ boundary. The crossing points are shown to be tangential indicating zero group velocity.

on the surface waves supported by such metasurfaces. For the square lattice the BZ boundary is a contour of high-symmetry, each edge of which is a mirror plane, with four more mirror planes through the center of the BZ and four-fold rotational symmetry.

Within this thesis the properties of surface waves propagating along either of the lattice vectors or at 45^o to them are investigated. This simplifies the discussion of the properties of these surface waves at the BZ boundary since they cross the BZ at the points of highest symmetry, figure 2.10. The surface waves with momentum along each lattice vector reach the BZ boundary at the center of the perpendicular bi-sectors, whilst the surface waves propagating at 45^o to the lattice vectors reach the BZ boundary at the corners of the BZ. Each of these points are high symmetry points at which the group velocity, v_g, of the surface wave must vanish. This is caused by the surface wave at the BZ boundary interacting with a counter propagating surface wave, which has been scattered by a lattice vector, to form a standing wave. Since the group velocity of the surface wave is directly related to its dispersion relation, equation 2.24, the interference between the two surface waves at the BZ boundary perturbs the surface wave dispersion. It can be seen that the surface wave dispersion must have zero gradient at the BZ boundary for all the square latticed metasurfaces used within this thesis for both lattice vectors and the 45^o directions of propagation.

$$v_g = \frac{\partial \omega}{\partial k} \tag{2.24}$$

2.5.2 Surface Waves Supported on a Metallic Patch Array

The first metasurface used in this thesis is a square array of square metallic patches spaced from a metallic ground plane by a dielectric overlayer, figure 2.11. The dimensions for the metasurface used in this study are as follows: $t = 787$ μm, $\lambda_g = 1.6$ mm and $a = 1.3$ mm. It shall be shown that the response of this metasurface is similar to that of a dielectric coated ground plane. The mode supported is fundamentally a waveguide mode within the dielectric, however the periodicity of the metallic patches perturbs the dispersion at in-plane wavevectors close to the BZ boundary, which for this structure is close to $\frac{2\pi}{\lambda_g} = 2000$ m^{-1}. This perturbation can be seen by the rapid change of the group velocity, tending towards zero, with respect to ω, at high in-plane momentum. The dispersion of the fundamental TM mode supported on the patch array is shown in figure 2.12.

The dispersion of the TM surface mode supported on this metasurface structure has several characteristics which make this surface wave ideal for the characterisation of surface wave reflection coefficients. Firstly the group velocity of the surface wave is $\sim 0.1c$ at 40 GHz, which combined with the low loss dielectric leads to propagation lengths of the surface mode of many metres. Experimentally there is no appreciable loss over a 60 cm long sample due to absorption within the metasurface. Secondly the decay length of the surface mode perpendicular to the surface is on the order of a wavelength or longer over a broad range of frequencies. This ensures that the overlap integral of the near-field of the surface mode and the near-field coaxial probe is large enough that the surface wave is readily coupled to by the near-field coaxial antenna used to measure the surface waves. The relative power flow within the dielectric core of the patch array structure is shown in figure 2.13. It can be seen that the amount of power flowing in the core only exceeds that of the air above approximately 35 GHz and

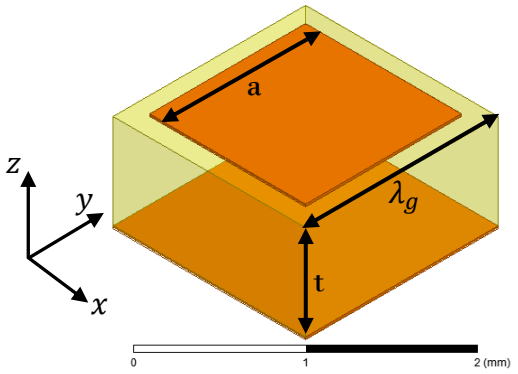

Figure 2.11: Schematic diagram of the metallic patch array metasurface unit cell showing the metal ground plane and patch (orange) and the dielectric layer (yellow).

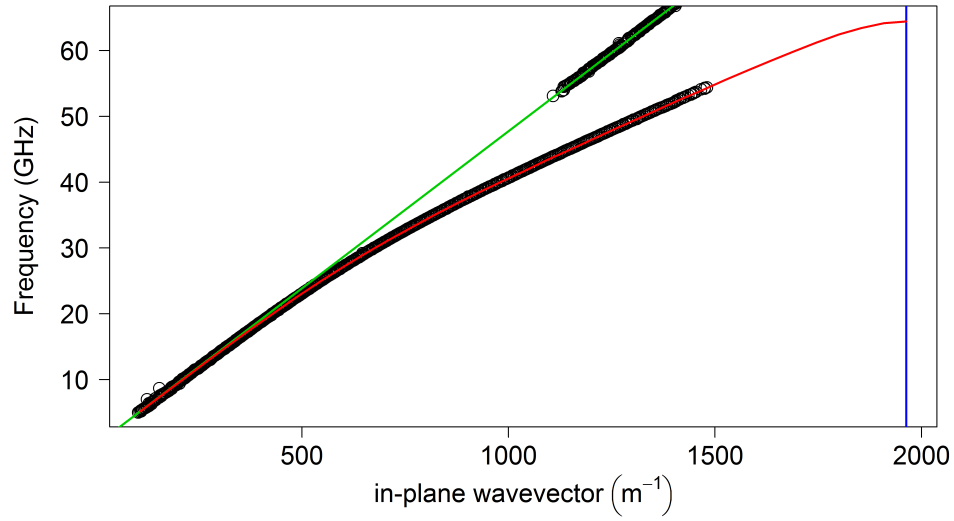

Figure 2.12: Dispersion relation of a square array of square metallic patches spaced from a metallic ground plane by a dielectric overlayer from FEM modelling (red line) and experiment (black circles), data taken by Joe Dockrey, with the light line (green line) and BZ boundary (blue line) shown.

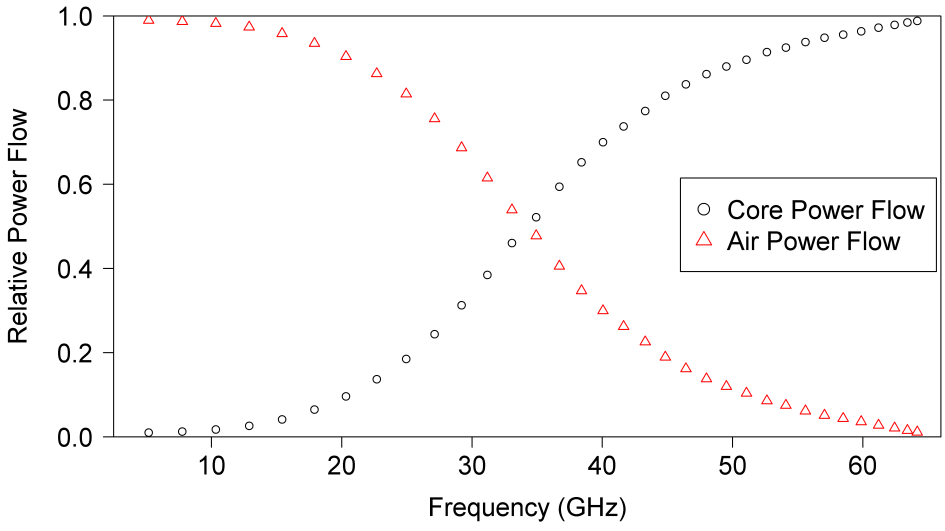

Figure 2.13: Relative power flow of the TM surface wave supported on a square array of square metallic patches on a dielectric coated ground plane. The amount of power confined within the dielectric layer is shown in the black points and the amount of power in the upper half space in red, values taken from FEM modelling.

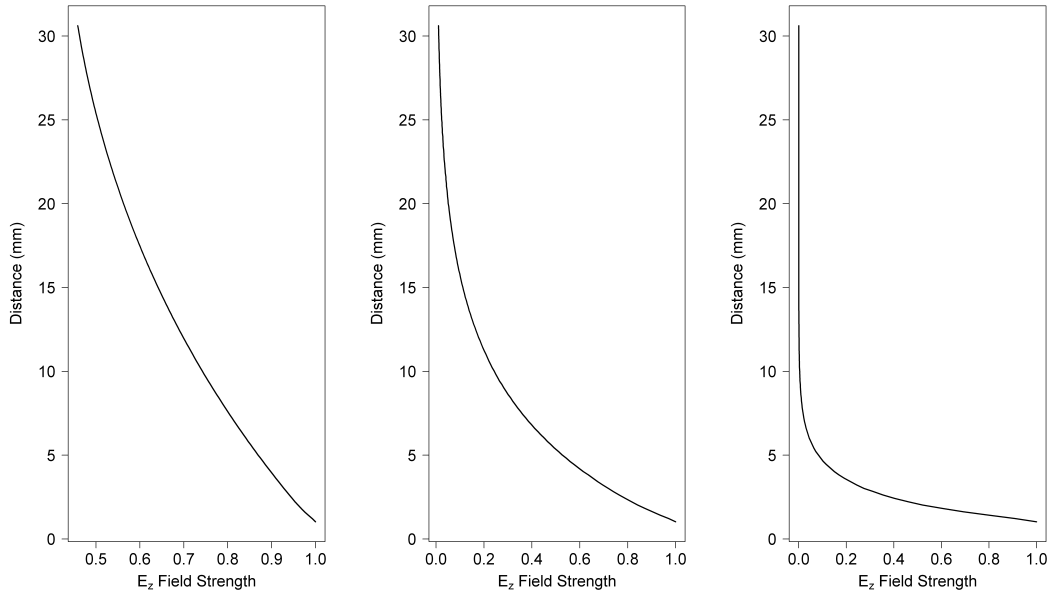

(a) 12.9 GHz (b) 24.9 GHz (c) 43.2 GHz

Figure 2.14: E_z field component of the near-field associated with the TM surface mode supported on the metallic patch array plotted along a line in the z-direction away from the metasurface in the center of the metal patch at a) 12.9 GHz, b) 24.9 GHz and c) 43.2 GHz.

there is still greater than 20% of the power flowing above the surface at 45 GHz. The power flowing within this metasurface has a large effect on the reflection coefficient of this surface wave from an interface as shall be shown in Chapters 5, 6 and 7.

The surface wave confinement of the modes is shown in the field profiles extracted from FEM modelling in figure 2.14. The near-field decay of the surface mode away from the surface (k_z) is strongly dependent on frequency: The confinement of the mode increases with increasing k_x (i.e. as the mode deviates from the light line). This confinement is defined by the k-vector perpendicular to the interface, k_z, which is directly related to the k-vector of the surface wave in the direction of propagation, k_x, since the total k-vector, k_0, is fixed by the frequency of the surface wave and $k_0^2 = k_x^2 + k_z^2$. The near-field of the fundamental TM surface mode supported on the metallic patch array is shown in figure 2.14 where the surface wave-like confinement of the mode in the upper half space is clearly seen. Note the rapid decay of the near-field of the surface wave fields at the highest frequency plotted, figure 2.14c, falling to 1/e over a distance of $\sim$3 mm. This, combined with the increased power flow within the dielectric core of the metasurface, increases the experimental difficulty in accurate determination of the surface mode propagation characteristics near at higher frequenies.

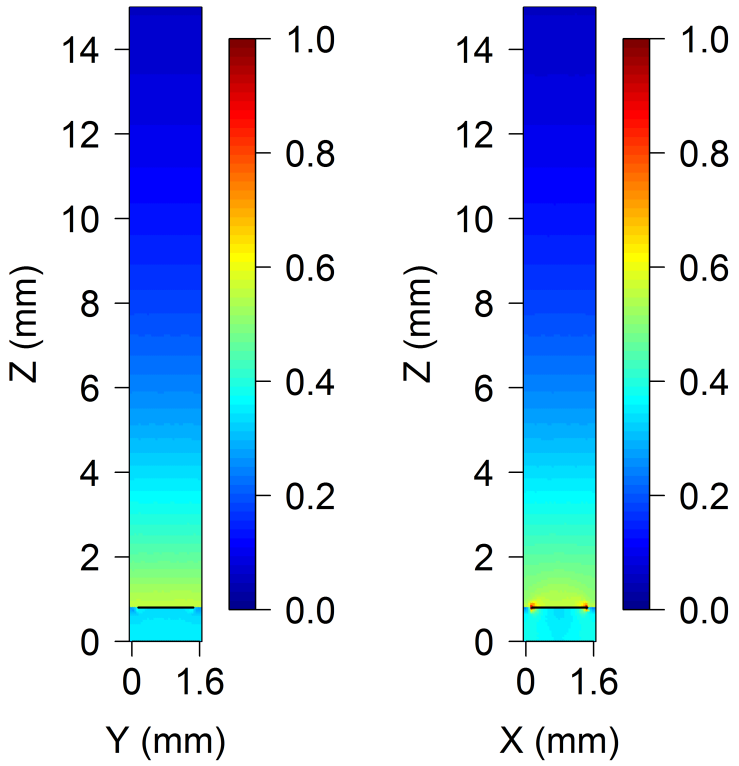

(a) yz-plane (b) xz-plane

Figure 2.15: Normalised E_z field component of the fundamental TM surface mode supported on the metallic patch array in a) the yz-plane and b) the xz-plane, at 24.9 GHz where the surface wave is propagating in the x-direction and the black represents the metal.

A cross-section of the patch array metasurface on which the E_z field component is plotted is shown in figure 2.15 where the mode is propagating in the x-direction. Figure 2.15a shows the waveguide-like nature of the mode within the dielectric core of the metasurface; the E_z field component has a near uniform field intensity within the dielectric. In contrast figure 2.15b shows the high field intensity and capacitative coupling between the nearest-neighbour metal patches. These high field intensities arise from the accumulation of charge at the edge of the patch. The charge accumulates at these edges because the electric field of the surface wave has a much longer wavelength than the dimensions of the patch. The electrons, which respond almost perfectly to the electric field (due to the approximately PEC properties of the metal) experience an electric potential gradient in the x-direction. The electrons accumulate at the edge of the patches since the applied electric potential is much stronger than the restoring

force associated with the imbalanced distribution of electrons within the patch. In both of the measurement planes, shown in figure 2.15, the near-field of the surface wave is shown to be uniform in the x- and y-directions in the upper half-space, except close to the edges where charge accumulates.

2.5.2.1 Patch Layer Effective Medium

Representation of both the metallic patch array and the Sievenpiper 'mushroom' array with an effective medium model is possible. In the effective medium model the structure of interest is replaced with an isotropic material whose parameters are determined from the structure. In both cases the effective medium model will be composed of two layers, one to represent the patch layer and another to represent either the via layer for the Sievenpiper 'mushroom' array or the dielectric layer below the metallic patch array. The patch array, if taken in isolation, is a frequency selective surface (FSS) the EM response of which is well known [84].

The FSS consisting of a square array of square metallic patches is shown in figure 2.16 and a TM polarised EM wave is considered incident upon the surface in the xz-plane. In this orientation the electric field in the plane of the surface, E_x, is excluded from the gaps (between the plates) whose direction is parallel to the x-axis. This is due to the metallic boundary conditions imposed by the metallic patches. As such the FSS may be approximated instead by a one dimensional array of strips, figure 2.16c, where the periodicity of the array is maintained in the x-direction. A full analysis of this structure has been performed by Clavijo et. al. [43], the results of which shall be reproduced here.

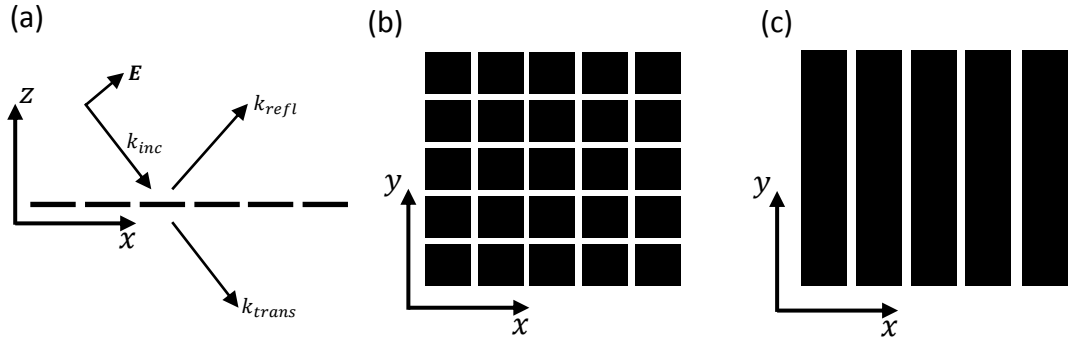

Figure 2.16: Schematic of the frequency selective surface created by a square array of square metallic patches where a) shows the geometry of the incident wave b) the square array and c) the reduction to a single set of strips possible due to the polarisation and plan of incidence.

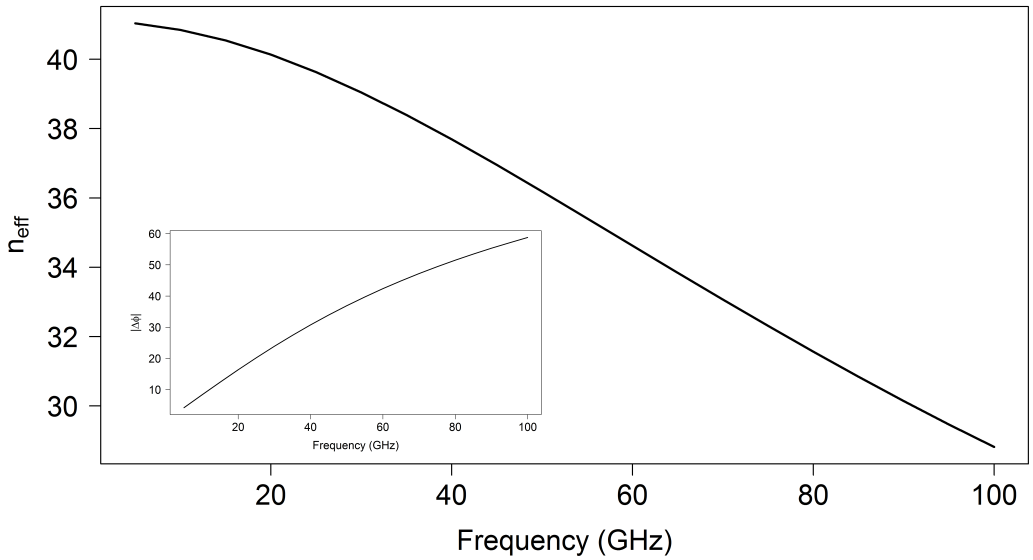

Figure 2.17: The effective refractive index of the thin layer in the effective medium model that represents the metallic patches calculated from the phase change through the reduced FSS. Inset: Phase change extracted from FEM modelling.

The effective medium material parameters needed to represent the FSS patch layer are found to be highly anisotropic such that the material parameters of interest are $\varepsilon_z = 1$, $\mu_y = 1$ with ε_x given by:

$$\varepsilon_x = \frac{2\lambda_\mathrm{g}}{\pi t_\mathrm{m}} \ln\left(\left[\cos\left(\frac{\pi(\lambda_\mathrm{g} - a)}{2\lambda_\mathrm{g}}\right)\right]^{-1}\right) \tag{2.25}$$

where t_m is the thickness of the metal and equivalently the thickness of the effective medium layer. This is derived from considering the transmission of a wave through the FSS layer, whose admittance is well know when reduced to a strip array [85], to free space. An increase in this permittivity is caused by the fact that the dielectric core has a permittivity which is larger than that of free space. The permittivity is increased by the average of the permittivity of the dielectric and that of free space.

Due to the highly anisotropic nature of the effective patch layer determining the refractive index from the permittivity and permeability of such a layer is not trivial. However the phase change of the EM wave transmitted through the FSS can be used to determine an estimate of the effective refractive index of the thin patch layer. This phase change, $\Delta\phi$, has been obtained using FEM modelling, figure 2.17.

$$n_\mathrm{eff} = \frac{\Delta\phi\, c}{2\pi t_\mathrm{m} f} \tag{2.26}$$

It can be seen in figure 2.17 that the refractive index of this layer is significant (> 30) and therefore even though the FSS layer is very thin a significant phase change occurs as the wave is transmitted through it. This phase change lowers the gradient of the dispersion of the surface wave supported on the metal patch array metasurface. This change of the gradient of the dispersion leads to an increased confinement of the surface wave than the equivalent for the simple dielectric coating.

2.5.3 Surface Waves Supported on a Sievenpiper Array

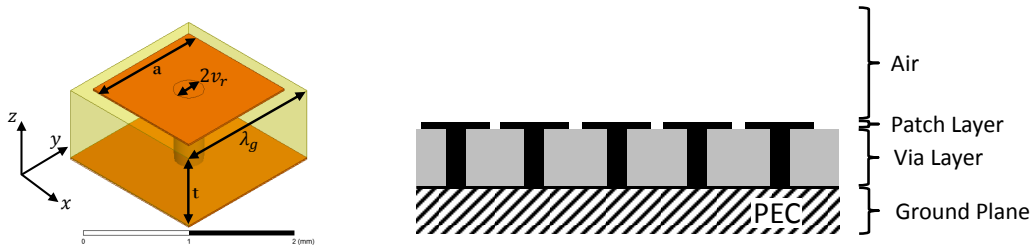

(a) (b)

Figure 2.18: Schematic diagram of the Sievenpiper 'mushroom' metasurface. a) Schematic diagram of the Sievenpiper 'mushroom' metasurface unit cell showing the metal ground plane, via and patch (orange) and the dielectric layer (yellow). b) Schematic diagram of the Sievenpiper 'mushroom' metasurface array showing the ground plane, via and patch layers.

The second metasurface discussed here, was first developed by Sievenpiper and consists of an array of metallic 'mushrooms' on a dielectric coated ground plane [71]. Each 'mushroom' consists of a square metallic patch connected to the ground plane via a metal cylinder, figure 2.18. The dimensions for the metasurface used in this study are as follows: $t = 787\mu$m, $\lambda_g = 1.6$ mm, $a = 1.3$ mm and $v_r = 150$ μm.

An effective medium approximation can be applied to the Sievenpiper 'mushroom' structure in the metasurface limit, when the unit cell is significantly subwavelength, the via array layer, figure 2.18b, can be considered to be a homogeneous highly anisotropic layer [43]. The effective permittivity in the direction normal to the surface of the metal ground plane is given by:

$$\varepsilon_z(\omega) = \varepsilon_d - \frac{1}{\omega^2 \varepsilon_0 \frac{\mu_d \mu_0 A}{4\pi} \left[\ln(\frac{1}{\alpha}) + \alpha - 1\right]} \tag{2.27}$$

where ε_d is the permittivity of the dielectric medium in the via layer, ε_0 is the permittivity of free-space, A is the cross-sectional area of the metallic patch and α is the ratio of the via cross-section to that of the unit cell. For this derivation the via layer is

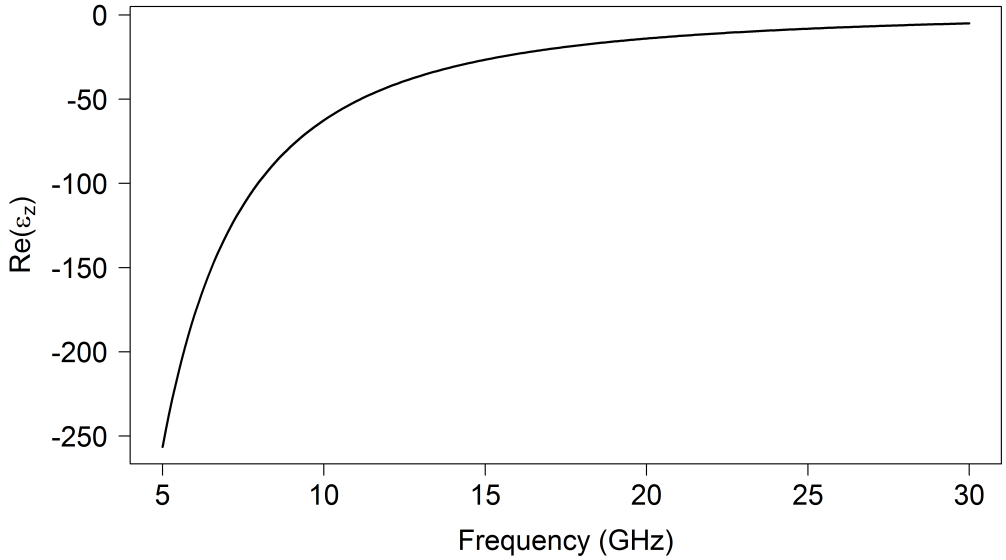

Figure 2.19: Real part of the effective relative permittivity of the via layer in the Sievenpiper 'mushroom' structure in the z-direction within the metasurface limit for the structure shown in figure 2.18.

considered to be a Brown's rodded medium with the consideration of the effect of the via radius since they vias are considered thin in the Brown's rodded medium [86, 87].

It is clear to see that the dispersion of the effective normal permittivity is Drude-like in its form [88], figure 2.19. In this way the Sievenpiper via layer for the electric field normal to the interface may be considered like a metal in the optical regime when there is a component of the E-field parallel to the vias and when the unit cell of the metasurface is significantly subwavelength. However for the electric field in the plane of the surface the via layer simply has a permittivity that is positive and approximately equal to that of the dielectric. The derivation of 2.27 is valid in the limit that the patch cross-sectional area occupies most of the cross-section of the unit cell of the metasurface. This is due to the fact that the material parameters for the via layer are calculated within a parallel plate waveguide, i.e. using a PEC boundary condition in place of the patch layer. If the patch is significantly smaller than the unit cell then the approximation that it can be considered as a continuous PEC boundary is invalid. The patch layer is also approximated as a FSS in the same way as for the metallic patch array that was discussed in section 2.5.2.1.

The dispersion of the TM surface mode supported on the Sievenpiper 'mushroom' structure used in this study is shown in figure 2.20. Several of the characteristics of this surface wave dispersion are of relevance in the study of surface wave reflection

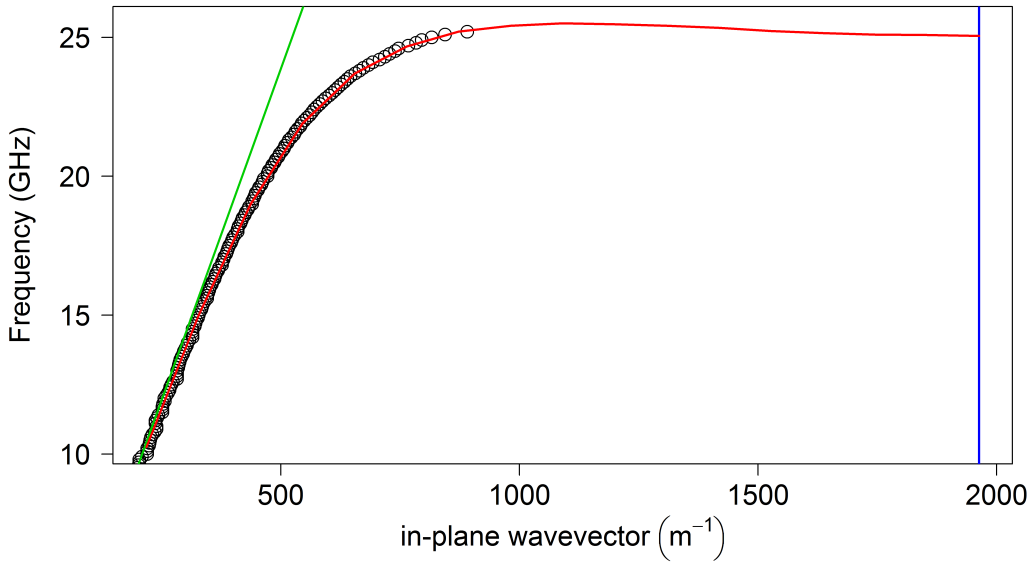

Figure 2.20: Dispersion relation of the TM surface mode supported on the Sievenpiper 'mushroom' metasurface from FEM modelling (red line) and experiment (black circles), data taken by Joe Dockrey, with the light line (red line) and BZ boundary (blue line) shown.

coefficients. Firstly, in contrast to the metallic patch array, the group velocity of the mode supported on the Sievenpiper array undergoes a change of sign in a very small frequency range. This change is such that in a small frequency band the mode has both positive group velocity and negative group velocity at the same frequency with different in-plane wavevectors. The range of in-plane wavevectors for which the group velocity of the surface wave is negative is associated with a condition when the power flow within the core of the metasurface is greater than that of the dielectric half-space above, figure 2.21. The direction of the power flow within the core of the metasurface is opposite to that in the half space above, indicated by the sign of the relative power flow, due to the negative effective ε_z, figure 2.19. Secondly above the asymptotic frequency of the mode there exists a surface wave stop band within which there are no surface waves supported on the structure. This stop band is of particular interest because it allows for the consideration of the reflection of surface waves at an interface that defines a surface on which modes are forbidden above a given frequency. This has been studied in both Chapter 6 and Chapter 7.

At frequencies close to the asymptote, the decrease in the group velocity of the mode increases the non-radiative losses experienced by the surface mode and as such its propagation distance is reduced. Interestingly, unlike the metallic patch array, at

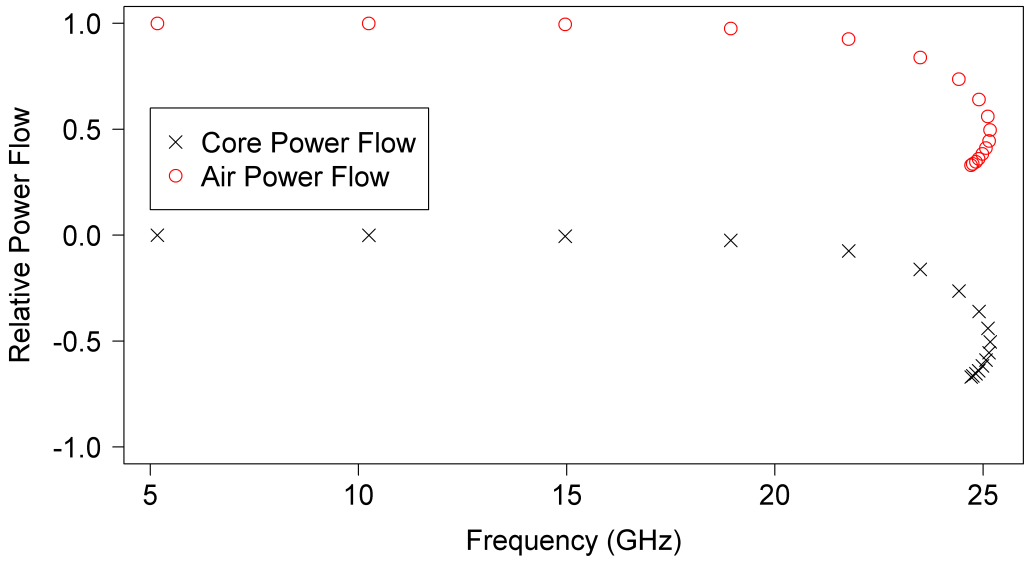

Figure 2.21: Relative power flow of the fundamental TM surface wave supported on a Sievenpiper 'mushroom' array. The amount of power confined within the dielectric layer is shown by the black crosses and the amount of power in the upper half space by the red circles, values taken from FEM modelling.

these frequencies most of the power flow is not confined within the via layer, figure 2.21. However, as for the metallic patch array, the confinement of the surface mode increases as the mode diverges from the light line. At frequencies close to the surface wave stop band, equivalently the asymptote of the TM surface mode, the decay length of the surface wave is ~ 2.5 mm, figure 2.22c

The E_z field component associated with the TM surface wave supported on the Sievenpiper 'mushroom' array is shown in figure 2.23 where the direction of propagation of the surface mode is along the x-axis. The E_z field component of the surface wave has a lower amplitude within the via layer than that found within the dielectric layer for the metallic patch array. It is clear from both the ratio of the power flow within the metasurface, figure 2.21, and the distribution of the E_z field component, figure 2.23, that the TM surface mode supported on the Sievenpiper 'mushroom' structure is not a simple waveguide mode of a grounded dielectric, which could be considered accurate for the metal patch array metasurface. However the capacitive coupling between neighbouring patches and the associated high electric field is seen for the Sievenpiper 'mushroom' structure as previously discussed for the metallic patch array.

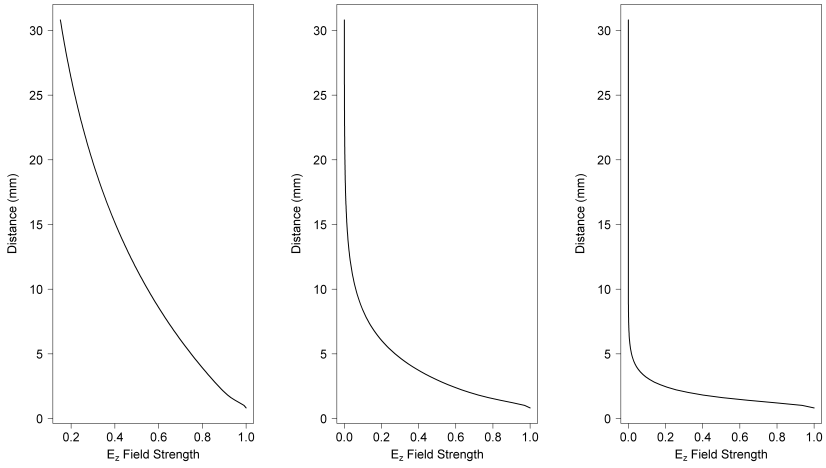

(a) 12.7 GHz (b) 21.8 GHz (c) 25.2 GHz

Figure 2.22: E_z field component of the near-field associated with the TM surface mode supported on a Sievenpiper 'mushroom' array plotted along a line in the z-direction away from the metasurface in the center of the unit cell at a) 12.7 GHz, b) 21.8 GHz and c)25.2 GHz.

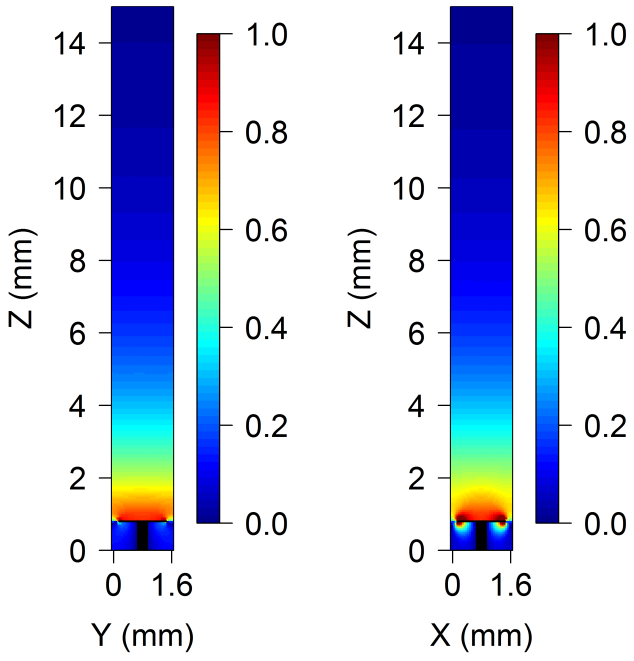

(a) yz-plane (b) xz-plane

Figure 2.23: E_z field component of the TM surface mode supported on the Sievenpiper 'mushroom' array in a) the yz-plane and b) the xz-plane, at 21.8 GHz where the surface wave is propagating in the x-direction and the black represents the metal.

2.6 Reflection of Surface Waves

Studies have analytically considered the reflection coefficient of surface waves for many different types of reflecting interface [79–81, 89–95]. However each solution employs different assumptions to solve the analytical equations and these assumptions introduce limitations on their applicability to describe the systems investigated within this study. Most importantly the geometry of the metasurface structure is never fully considered: Previous works have considered the guiding surface to be a plasmonic metal [90, 91, 93, 94] or represented simply using an impedance boundary condition [79–81, 92].

Studies on the reflection coefficient of a surface wave incident upon the termination of a surface wave supporting surface to free space was considered by Chu et. al in the 1960's [79–81], where the reflection and scattering to free space of a surface wave was calculated and measured experimentally. An impedance approximation was applied to the guiding interface in order to provide the necessary boundary condition for supporting a surface wave, whereas in the experiment a dielectric coated metallic ground plane was used as the surface wave guiding interface [79]. Analytically the reflection coefficient of surface waves has been considered for step changes in the guiding interface [93], changing the guiding interface impedance [92], changing the dielectric half space [89–91], gaps in the guiding interface [94] and introducing a finite height overlayer discontinuity [95]. Experimental investigation of these systems has seen less attention [79] and full geometrical description of metasurface systems have not been described.

2.7 Conclusion

In this chapter an overview of the surface wave properties of various structures at microwave frequencies has been presented. The confinement of surface waves at microwave frequencies through surface structuring, i.e. metasurfaces, has been introduced and explored for the metasurfaces used in this thesis. The surface wave supported by a dielectric coated ground plane has been shown to be primarily a waveguide mode within the dielectric with near-field decay in the half-space above. Further the corrugation of a perfectly conducting plane has also been shown to support bound surface waves, provided that the corrugations are sufficiently subwavelength, the dispersion of which is defined by the resonances associated with the structure. These principles have been extended to the two metasurfaces used within this thesis, the metallic patch array and the Sievenpiper 'mushroom' array. The principles of BZ boundaries and their effect on surface wave dispersions for periodic structures has been explored and the effective medium model for representing the metasurface has been discussed. It has been shown that the Sievenpiper 'mushroom' metasurface and the metallic patch array

have significantly different surface wave dispersions. The dispersion of the surface wave supported by the metallic patch array metasurface has been shown to have similarities to the dispersion of a surface wave supported on a dielectric coated metal ground plane. Whilst the dispersion of a surface wave supported on a Sievenpiper 'mushroom' metasurface has been shown to be dictated by the structural resonance of the metasurface. The surface wave properties discussed within this chapter will subsequently be used when describing the effect of planar discontinuities in the metasurface to surface waves incident upon them. The planar discontinuities investigated within this thesis affect the surface modes on the metal patch array metasurface and the Sievenpiper 'mushroom' metasurface differently due to their field profiles. These differences will be explored for a variety of discontinuities in Chapters 5, 6 and 7.

Chapter 3

Techniques Used to Characterise Surface Waves on Metasurfaces

3.1 Introduction

In this chapter the experimental, numerical and analytical techniques used to characterise the structures investigated in this thesis are presented. A brief overview of the finite element method (FEM) modelling techniques used to produce the numerical results in this study is given in section 3.2. Development of a waveguide material characterisation system for measuring the material parameters of the dielectrics and composite materials used in this thesis is presented in section 3.3. A new technique for measuring the dispersion of a surface wave supported on a metasurface is presented in section 3.5. Development of an antenna capable of measuring the local electric field of a surface wave supported on a metasurface is presented in section 3.4 and a system for spatial mapping of the electric field using a 3-axis translation stage discussed in section 3.6. The creation of planar phase front surface waves over a broad frequency band is presented in section 3.7 which are utilised to measure the reflection coefficient of a surface wave incident upon a discontinuity; the method for obtaining the reflection coefficient is presented in section 3.8.

3.2 Finite Element Method Modelling

FEM modelling has been used extensively in this thesis to help design the metasurface structures investigated, and to determine the reflection coefficient of surface waves incident upon various planar discontinuities. FEM modelling is performed using the High Frequency Structure Simulator (HFSS) [96], which has been used to predict the dispersion of surface waves supported on metasurfaces and the reflection, transmission and

scattering to free space of surface waves, supported on a metasurface, incident upon various different planar discontinuities. HFSS contains a variety of distinct solution types, two of which have been used in this thesis: The first is the Eigenmode solver used for obtaining the dispersion relations of surface waves supported on a periodic metasurface, useful in the design of such metasurfaces. The effect of varying the dimensions of the elements within the metasurface unit cell on the dispersion relation of surface waves supported on the metasureface can be investigated using the Eigensolver. Secondly the Driven Modal solver which solves the EM field in a region of interest at a user defined frequency, which may be either periodic or non-periodic.

FEM is a numerical method which divides a three dimensional region into smaller, usually tetrahedral shaped, volumes known as tetrahedra and then solves Maxwell's equations at the boundaries between these tetrahedra [97, 98]. The EM field solution is then calculated at the vertices of the mesh element or the mid points of the edges of the element. Which of these sets of points is used depends on whether the quantity being calculated acts tangential to the edges or the face respectively. These points are then formed into a matrix of equations of the form:

$$\nabla \times \left(\frac{1}{\mu} \nabla \times \mathbf{E} \right) - k_0^2 \varepsilon \mathbf{E} = 0 \tag{3.1}$$

where k_0 is the free space wavevector and ε and μ are the relative permittivity and permeability of the region respectively. This matrix of equations is then simultaneously numerically solved for the **E**-field from which the **H**-field can be derived:

$$\mathbf{H} = \frac{1}{\omega \mu} \nabla \times \mathbf{E} \tag{3.2}$$

From the numerically calculated fields a generalised scattering matrix (S-Matrix) is determined from which the reflection and transmission properties of the structure can be extracted. The S-Matrix can also be used to analyse the eigenmodes of the modelled structure by determining the frequencies at which poles in the S-Matrix occur [74].

3.2.1 Meshing and Convergence

In order to obtain an accurate representation of the EM fields present around a metasurface structure HFSS employs an adaptive iterative mesh refinement process. Initially a coarse mesh is defined within the region of interest and a first approximation of the EM fields is calculated. This mesh is then refined in regions of high field gradients, equivalently in regions where the EM field solution error is high. Tetrahedra within these regions are divided into a number of smaller tetrahedra and the EM field solution recalculated. Solutions to the EM fields associated with a metasurface structure are

expected to converge such that the further refinement of the mesh does not significantly change the EM field solution. This convergence is determined through the change in the generalised scattering matrix (S-matrix) for Driven Modal solutions and by the change in the Eigenmode frequency for the Eigenmode solver. The change in the Eigenmode frequency or the change in the S-matrix are expected to decrease through the iterative meshing process with an approximately exponential form.

3.2.2 Boundary Conditions

In HFSS the region of interest must be surrounded by appropriate boundary conditions in order for a physically correct solution to be obtained. These boundary conditions take various forms including perfect electric, perfect magnetic, periodic boundary conditions and many others. The eigenmode solutions determined within this thesis utilise the periodic boundaries and both the perfect electric and magnetic boundaries. Since the metasurfaces designed in this thesis are periodic, pairs of master-slave periodic boundaries are required. A master-slave boundary pair requires that the electric and magnetic fields at the slave boundary exactly match those at the master boundary. These periodic boundary conditions produce a solution which is exactly equivalent to an infinite array of these metasurface unit cells in the direction tangential to the faces of the mast-slave boundary pair. A relative phase difference may be applied between the master and slave boundary to allow angles of incidence other than normal to be investigated. This relative phase difference may also be greater than that of a grazing photon in order to investigate non-radiating surface modes whose dispersion lies outside the light line. The perfect electric and perfect magnetic boundary conditions act as perfect electric conductors and perfect magnetic conductors respectively. Therefore these boundaries force the tangential electric or magnetic field to zero at these boundaries, ($E_{||} = 0$) for the perfect electric boundary and ($H_{||} = 0$) for the perfect magnetic boundary. Finally radiation boundary conditions are used to mimic the propagation of radiation to free space. Therefore any EM field incident upon these boundaries is absorbed without reflection without increasing the modelled region of interest.

3.2.3 Designing Metasurfaces

Designing metasurfaces with the required dispersion relation is performed by modelling a single unit cell of the metasurface and applying periodic boundary conditions to the unit cell faces. The eigenmodes of the unit cell are then computed using the eigenmode solver within HFSS for a given in-plane wavevector, $k_{||} = \sqrt{k_x^2 + k_y^2}$. The wavevector is defined by the periodic boundary conditions, with any combination of k_x and k_y possible, and the resonant frequency of the mode is obtained. The dispersion relations

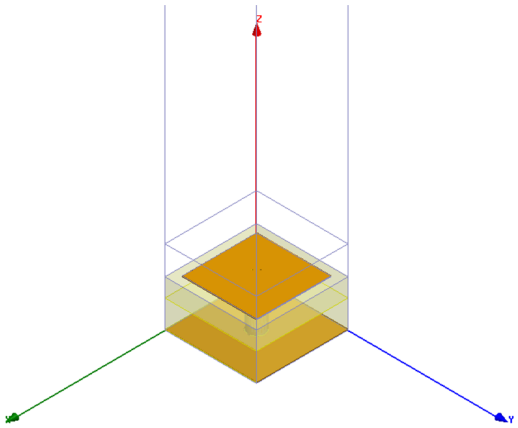

Figure 3.1: Schematic of a Sievenpiper 'mushroom' metasurface unit cell with the coordinate system labelled where orange represents the metal structure.

of interest in this thesis are those along a lattice vector of the metasurface and as such are either purely k_x or k_y. Since the metasurfaces considered within this structure all contain square symmetry $k_x = k_y$, we shall therefore restrict ourselves to considering the case when $k_y = 0$. The Eigenmodes for a number of values of k_x are found in order to determine the whole dispersion of the mode propagating purely in the x-direction. It is also possible to restrict the class of surface mode we are interested in, either TE or TM, by applying perfect electric, TE, or perfect magnetic, TM, boundary conditions to the faces in the xz-plane, figure 3.1.

3.2.4 Determining the Reflection Coefficient for Surface Waves

Modelling the reflection coefficient of surface waves incident upon a planar discontinuity is performed by including the full metasurface structure. The inclusion of the full metasurface structure is computationally intensive since the convergence of the FEM solution depends on the accurate representation of the metasurface elements by the tetrahedra. Therefore each sub-wavelength metasurface unit cell must be broken down into many sub-unit cell size tetrahedra. Typically convergence of a model is achieved with tetrahedra whose side length is approximately 0.2λ, this ensures that the variation of the EM field is represented on a sufficiently subwavelength scale. Since these models require sub-unit cell size tetrahedra and a unit cell is typically $0.1 - 0.2\lambda$ these models require significantly more tetrahedra than usual to reach an accurate EM field solution. In order to reduce the computational power required, and equivalently the solving time, it is necessary to introduce a high density mesh into the region within the metasurface structure and the region of high field gradients in the half space above, but close to, the metsurface interface. Constraints on the size of the initial tetrahedra

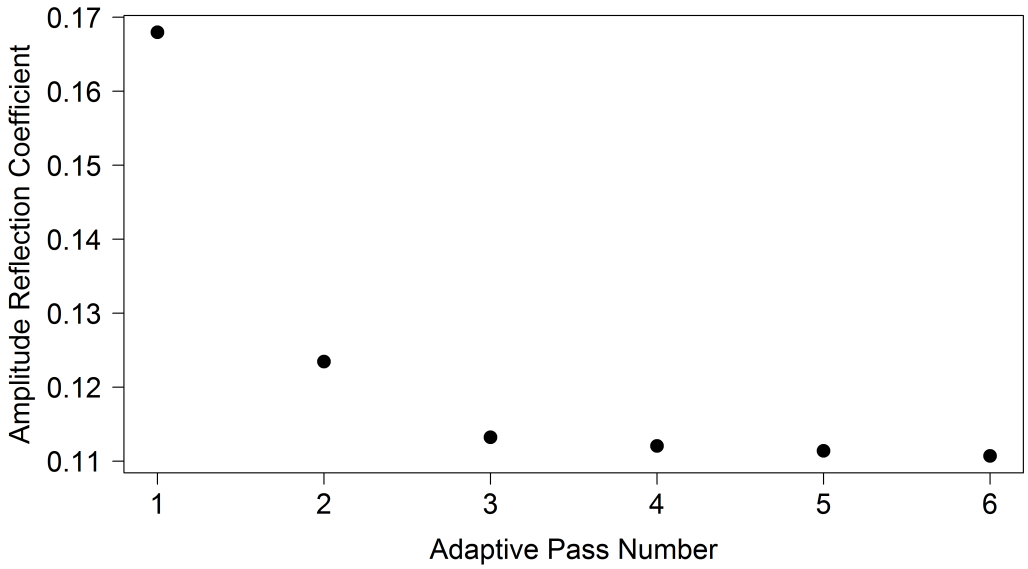

Figure 3.2: Plot of the reflection coefficient of a surface wave incident upon the termination of a metallic patch array to free space, chapter 5, obtained from analysis of the EM field predicted by FEM modelling for increasing iterations of the adaptive meshing process.

are manually applied to these regions, within the metasurface core and the dielectric half-space region within 2 mm of the interface, such that approximately 1 million tetrahedra are placed within these volumes. The convergence of the model can be measured by determining the value of the reflection coefficient for increasing iterations of the adaptive mesh process. An example of this convergence is seen in figure 3.2, where the reflection coefficient is determined for the termination of a metallic patch array to free space at 25 GHz, see chapter 5. The convergence of these models in a relatively small number of passes is achieved by these constraints on the initial mesh, the change in the modelled amplitude reflection coefficient is small ($\lessdot$0.002) after pass number 3, figure 3.2. By increasing the density of the tetrahedra for the first pass within the metasurface structure and close to its interface the convergence of the reflection coefficient is achieved with fewer tetrahedra and in less time than without such operations.

3.3 Material Parameters Characterisation

Determining the complex permittivity and permeability of a material is important in the design of surface wave absorbing materials and surface wave devices [99–113]. Later work presented here relies on the accurate measurement of the material parameters of

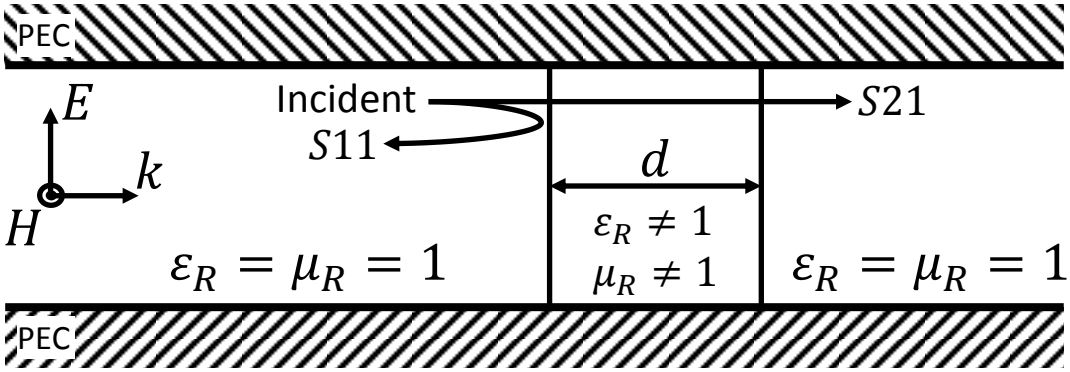

Figure 3.3: Schematic of the waveguide system used to obtain the material parameters of an unknown material, the measured S-parameters S11 and S21 are indicated.

composite materials; microwave absorbing materials have been realised through loading of magnetic ferrite materials into a dielectric elastomer. The characterisation of the material properties of these microwave absorbing materials and the dielectric elastomers used in chapter 6 has been performed using this system. The microwave absorbing materials have been used in the plane wave launcher discussed in section 3.7.

The complex permittivity and permeability of an unknown material can be obtained from the complex reflection (S11) and transmission (S21) coefficients of a slab of this material placed within a reflectionless waveguide [100, 101, 109, 114–119], figure 3.3. The derivation of the material parameters from the reflection and transmission coefficients is presented in Appendix A.

In general the propagation of modes within a waveguide can be characterised by the direction of the electric and magnetic fields by comparison to the direction of propagation. For the descriptions of the modes that follows we shall consider the wave propagating purely in the x-direction and waveguides to be infinite in extent in the x-direction. We consider the fields in the yz-plane cross-sections unless otherwise stated. The three possible mode types are transverse electric (TE), transverse magnetic (TM) or transverse electromagnetic (TEM). In the TE case $E_x = 0$ ($H_x \neq 0$), there is no longitudinal component of the electric field, conversely in the TM case $H_x = 0$ ($E_x \neq 0$), there is no longitudinal component of the magnetic field. Finally in the TEM case $E_x = H_x = 0$, there is no longitudinal component of either the electric or magnetic field.

The fundamental mode supported within a rectangular waveguide is a TE mode with the field quantised across the long edge of the waveguide a, the electric field profile is shown in figure 3.4. Higher order quantisations of the electric field exist within the rectangular waveguide and the lowest frequency propagating mode within

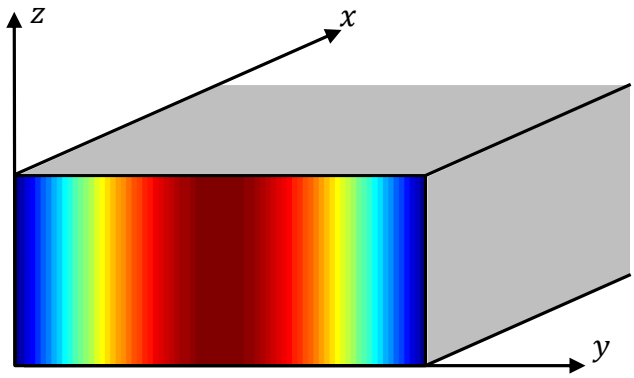

Figure 3.4: Time averaged electric field associated with the TE_{10} eigenmode plotted over the cross-section of an air filled X-band rectangular waveguide at 10GHz. Red and blue regions correspond to high and low field respectively.

a rectangular waveguide is determined by a, when the wavelength is longer than twice the length of the long edge, $\lambda_0 > 2a$, no propagating modes exist below that frequency, full derivation of waveguide fields can be found here [120].

The reflection and transmission of the fundamental waveguide mode upon a slab of material has been used to determine the material parameters. Such a system has been employed to characterise the materials used in this thesis, the initial calibration of this system was performed by obtaining the material parameters of a well known material; Teflon. The complex permittivity of Teflon is expected to be $\varepsilon \approx 2.05 + 0i$ and the complex permeability is expected to be $\mu = 1 + 0i$. Figure 3.5 shows the obtained material parameters for a 5mm thick slab of Teflon in an X-Band waveguide (8.5-12.4 GHz).

3.3.1 Application to Microwave Absorbing Materials

A study of the microwave material parameters of manganese zinc ferrite (MnZnFe) loaded into a base elastomer with non-dispersive material parameters, $\varepsilon = 2.6 + 0i, \mu = 1 + 0i$, in the frequency range of interest has been performed. These composite materials are a candidate for creating microwave absorbing materials [121–123], the material parameters of such a system has been measured for increasing concentration of MnZnFe, figures 3.6a and 3.6b. The magnetic properties of the MnZnFe produces significant absorption at the microwave frequencies of interest due to a broad resonance and therefore a large magnetic loss tangent. Whilst the significant dielectric loss is produced by the electrical polarisability of the MnZnFe particles dispersed within the elastomer. This microwave absorbing material has been employed within the plane wave launcher, dis-

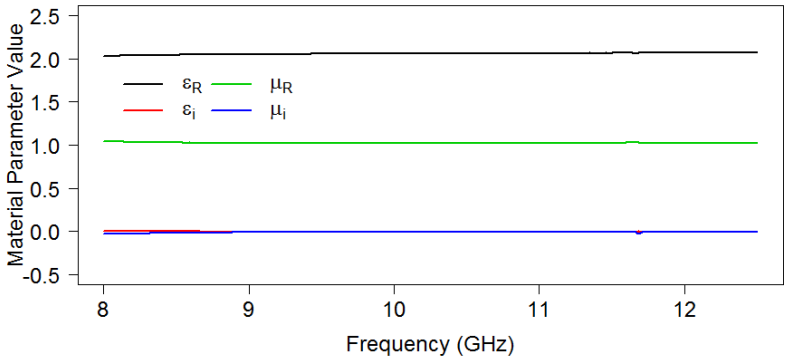

Figure 3.5: Complex material parameters of Teflon measured using the complex reflection and transmission coefficients. The expected values are as follows: $\varepsilon_R \approx 2.05$, $\mu_R = 1$, $\varepsilon_i \approx \mu_i \approx 0$.

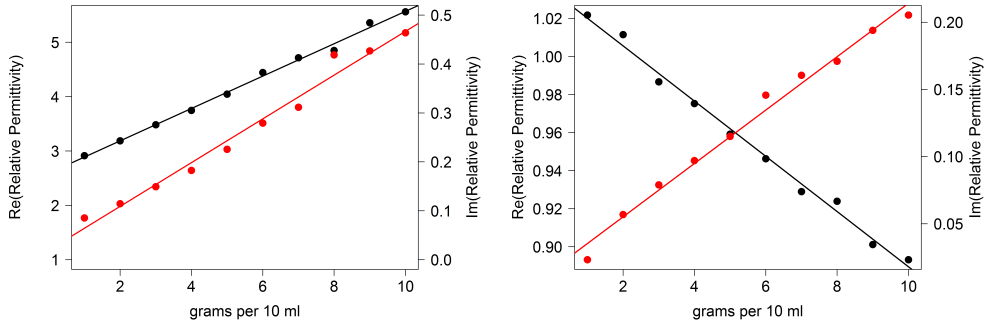

(a) Complex Permittivity (b) Complex Permeability

Figure 3.6: Measured complex material parameters for MnZnFe loaded elastomer at 10 GHz for increasing concentration of MnZnFe, straight line fits are added to guide the eye.

cussed in section 3.7, to absorb microwave radiation within the parallel plate waveguide.

3.4 Near-Field Coaxial Probe

Excitation and detection of surface waves requires a source and detector capable of measuring the near-field above the interface associated with these modes. Experimentally this has previously been achieved in a variety of ways including via the diffracted fields passing through a metallic letterbox [124] or via the exponential fields associated with total internal reflection [125]. A new device for experimentally characterising the near-fields associated with a surface wave propagating on a metasurface has been developed using a coaxial waveguide.

Measurement of the near-field associated with a surface wave in the microwave

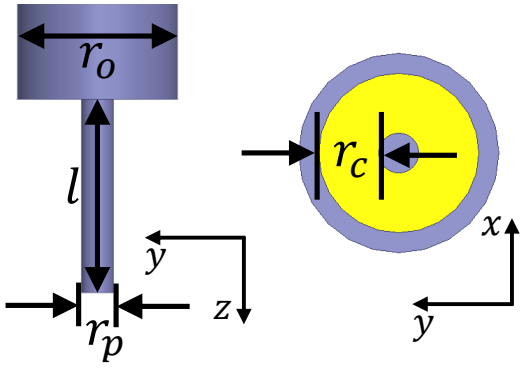

Figure 3.7: Schematic of the experimental near-field coaxial probe used to detect near-fields associated with surface waves supported on metasurfaces.

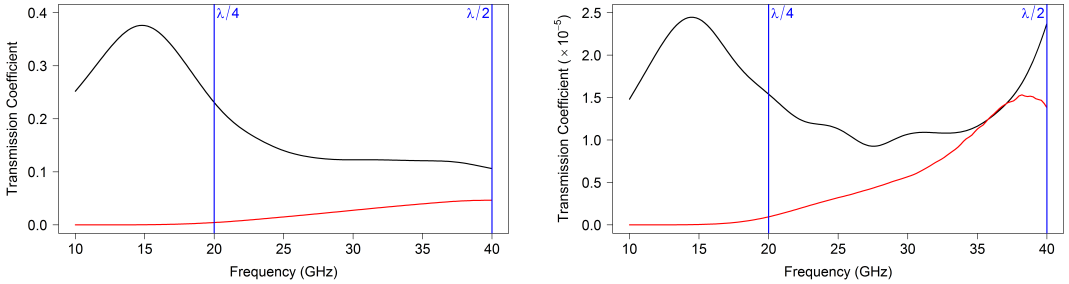

(a) Electric field orientated parallel to the coaxial pin.

(b) Electric field orientated perpendicular to the coaxial pin.

Figure 3.8: FEM modelled transmission of the radiation excited by a stripped coaxial antenna, with $l = 3.75$ mm, and detected by a waveport. The distance between the coaxial antenna and the waveport is 1.5 cm for the near-field (black line) and 20 cm for the far-field (red line). The $\lambda = 2l$ and $\lambda = 4l$ frequencies are also shown.

regime is performed using a coaxial probe designed to be minimally perturbing to the surface wave. This near-field probe has been experimentally realised by the use of a coaxial waveguide, the inner metallic pin of which has been extended beyond the termination of the coaxial waveguide, figure 3.7. This coaxial antenna is mostly sensitive to electric field along the axis of the pin, it can be considered to act as an electric dipole along the same axis. The length of the electric dipole can be approximated to lie close to the $\lambda = 2l$ resonant condition, as shown in figure 3.8. The electric fields associated with the resonance of a stripped coaxial antenna with $l = 3.75$ mm are shown in figure 3.9.

Figure 3.8 shows the transmission between the stripped coaxial dipole antenna with $l = 3.75$ mm and a waveport in FEM modelling. This waveport accepts both propagating and non-propagating modes, and the transmission has been measured in

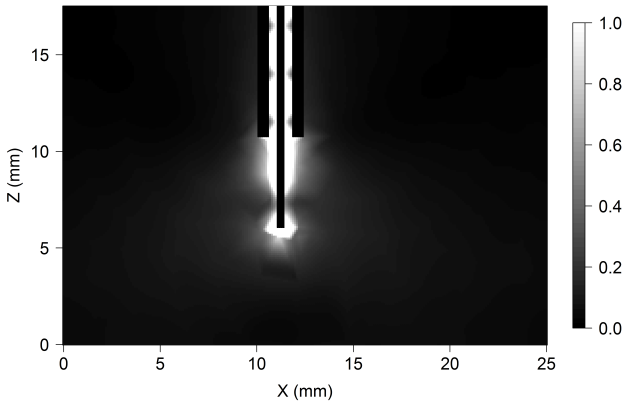

Figure 3.9: Time average E-field associated with the near-field coaxial probe, with $l = 3.75$ mm, driven at $\lambda = 2l$ (40 GHz).

both the near-field of the coaxial antenna, where the distance is 0.5λ of the lowest frequency, and far-field of the coaxial antenna, where the distance is $>6\lambda$ of the lowest frequency. The transmission in the far-field is dominated by the propagating modes excited by the coaxial antenna whilst the near-field transmission is not only determined by these but also the non-propagating fields which decay away from the source. The non-propagating fields associated with the antenna have in-plane wavevectors greater than k_0 and are therefore able to couple directly to the near-field radiation associated with surface waves. It can be seen that for this stripped coaxial antenna there exists a peak in the near-field signal at approximately 15 GHz corresponding to non-propagating modes since the far-field transmission at these frequencies has near zero amplitude.

A comparison between the transmission of both the propagating and non-propagating fields associated with the antenna for both polarisations, electric field orientated parallel, TM, and perpendicular, TE, to the coaxial pin, has been performed. The transmission coefficient for TM polarisation is shown in figure 3.8a and for TE polarisation in figure 3.8b. It can be seen that the transmission coefficient is on the order of 10,000 times larger for TM polarisation than that of TE polarisation. It is therefore approximated that these near-field coaxial antennas are only sensitive to the electric field orientated along the coaxial pin of the near-field antenna. In order to simplify the discussion of the experimentally characterised electric field within this thesis they shall be labelled with the component of the electric field parallel to the coaxial pin orientation.

Practically the thickness of the coaxial pin within the coaxial waveguide, $r_p = 0.25$ mm, is too large to resolve sharp subwavelength features at higher frequency. An example of such features is the minima associated with high reflection coefficients, shown in figure 3.10, where the E-field strength of the interference between an incident and

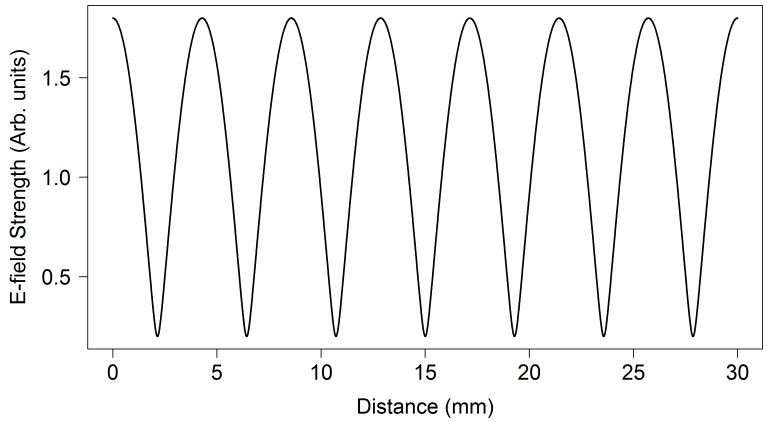

Figure 3.10: Time averaged electric field profile of the interference between an incident wave and a reflected wave with $r = 0.8$ at 35 GHz.

reflected wave with an amplitude reflection coefficient of 0.8 at 35 GHz is shown. The width of these minima is on the order of 2 mm which is not sufficiently resolved by the original coaxial antenna. At higher frequencies or increase in the in-plane wavevector the width of these features may become comparable to the effective size of the antenna. In order to overcome this limitation the exposed coaxial pin has been replaced by a short length of copper wire with a radius of $r_p = 40$ μm, soldered to the pin of the coaxial waveguide. This significantly increases the resolution of the coaxial antenna and allows the measurement of sharp subwavelength features.

3.5 Surface Wave Dispersion Measurements

Measuring the dispersion of surface modes supported on a metasurface is a fundamental part of understanding the EM response of such a structure and the characteristics of the surface waves supported by it. Previous methods of measuring the dispersion mostly relied upon one of two methods. Firstly Otto coupling of propagating radiation into the surface mode via a higher index dielectric material [125, 126] and secondly referencing the change in phase of the surface wave to that of a grazing photon [127]. The first of these methods is time consuming since each value of $k_{||}$ must be independently obtained by varying the angle of incidence of the radiation through the prism. The second method requires use of a metallic sample to produce a surface current with a dispersion equivalent to that of a grazing photon, it would be preferable to determine the dispersion from the surface wave using the metasurface alone.

At a single frequency the propagation of surface waves along a structure is directly

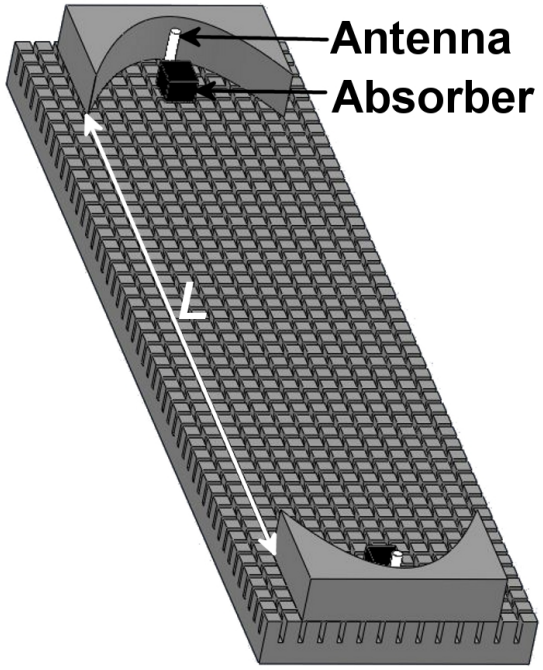

Figure 3.11: Schematic of the collimating mirrors setup used to in the characterisation of the surface wave dispersion, white cylinders indicate the position of the antenna and the black boxes indicate the position of the absorbers with an example metasurface of square pillars, see Chapter 4.

related to the dispersion of that surface, $\mathbf{E} \propto exp(i(k \cdot r - \omega t))$. Detection of the phase of this surface wave at two different distances from the source enables the determination of the $k_{||}$ value for the surface at that frequency. The phase of the transmitted signal is recorded at two different distances between the source and the receive antennas, L_1 and L_2. By using two distances and obtaining the differences in phase for the two situations, the phase shifts brought about at the coupling-in and coupling-out structures are eliminated. Thereby the wavevector, $k_{||}$, required for the derivation of the surface modes dispersion, is obtained simply from the phase change $(\varphi_2 - \varphi_1)$ over the distance (L_2-L_1) as given below:

$$k_{||} = \frac{2\pi}{L_2 - L_1}\left(\frac{\varphi_2 - \varphi_1}{2\pi} + m\right) \tag{3.3}$$

Here m is an unknown integer since the system measures the phase only to modulo 2π. This unknown integer m is however readily obtained by changing it in unit steps and examining how it impacts the resulting dispersion curve which, away from any resonance, has to lie close to the light line.

This technique is combined with a collimating system, figure 3.11, to increase the

amount of power transmitted across the sample in order to determine the dispersion of lossy surface modes. These losses are typically found at large $k_{||}$ values or small group velocities, $\partial\omega/\partial k$ [128, 129]. Stripped coaxial antennas are used as near-field sources to excite and detect the surface waves, see section 3.4. These coaxial antennas are situated at the focus of a metallic mirror whose profile is parabolic in the plane of the surface and uniform in the direction perpendicular to the surface. Surface waves are emitted with approximately cylindrical phase fronts from these antennas so the purpose of the parabolic mirrors is to collimate the surface waves such that all the path lengths reflected from the mirror are identical and guide the power across the sample. Direct transmission of the surface waves between the coaxial antennas is prevented by absorbing material. This technique has been employed to measure the dispersion of surface wave supported on a square array of square cross section metallic pillars in chapter 4.

3.6 Spatial Mapping of the Electric Field

Spatial mapping of the electric field is highly desirable at microwave frequencies since it allows sub-wavelength characterisation of the near-field associated with a surface wave supported on a metasurface. This system has been realised through the use the near-field coaxial probe whose operation is discussed in section 3.4 and a 3-axis translation stage with a resolution of 100 μm. A VNA is used to measure the intensity and phase of the electric field detected by the near-field coaxial probe. The translation stage has a range of approximately 1 m in the x and y directions, typically the plane of the sample, and 80 cm in the z-direction, this allows the electric field across large samples to be characterised along with the scattered radiation from any metasurface.

3.7 Launching Planar Phase Front Surface Waves

In order to determine the surface wave reflection coefficient for normal incidence at a reflecting interface a source of surface waves with planar phase fronts was developed, since in this case the interference between the incident and reflected waves is analytically trivial. Such a system has been realised using an apsherical Perspex lens to shape the emission from a source of microwaves with circular phase fronts within a parallel plate waveguide into planar phase fronts.

Lenses are a common way of controlling the propagation of light and can be used for focussing and collimating beams of radiation [130]. Within a parallel plate waveguide the fundamental transverse electromagnetic (TEM) mode is excited by applying an alternating voltage difference between the top plate and the bottom plate of the

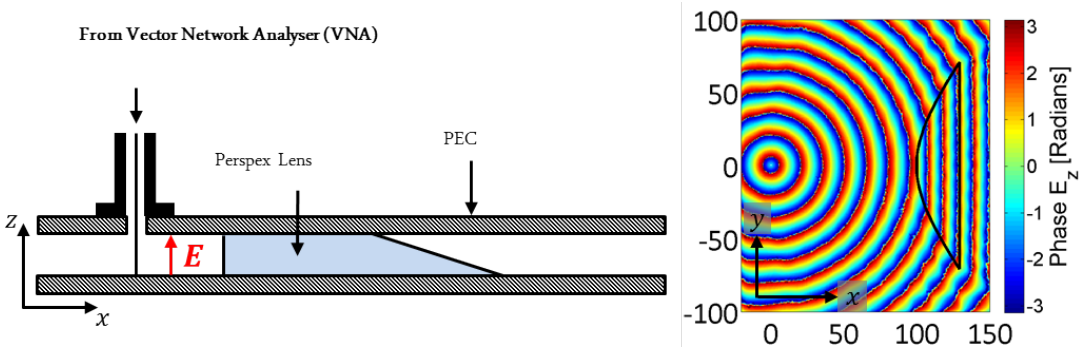

Figure 3.12: Schematic of the plane surface wave launching parallel plate waveguide device

waveguide. This is achieved by connecting the inner core of a coaxial waveguide to the bottom plate using a metallic pin and the outer sheath to the top plate, figure 3.12, the wave propagates outwards from this pin with circular phase fronts in the xy-plane. These waves then pass through a perspex lens which is uniform in the z-direction and has an aspherical profile described by equation 3.4 in the xy-plane.

$$r(\theta) = r_0 \frac{n_2 - n_1}{n_2 cos\theta - n_1} \tag{3.4}$$

Here n_1 is the refractive index of the material filling the waveguide (air), n_2 is the refractive index of the material used to make the lens, θ is the angle from the x-axis and r_0 is the distance from the point source to the front of the lens at $\theta = 0^o$.

This profile modifies the cylindrical phase fronts produced by the source at position (0,0), figure 3.12, to planar phase fronts at the exit of the lens. This aspherical profile is chosen to produce a wide region of planar phase fronts [131]. The beam is not just planar but also has an approximately gaussian intensity distribution due to the increasing reflection coefficient of the perspex at higher angles of incidence. A linear taper in the xz-plane on the exit face prevents strong reflection at this interface, avoiding interference effects within the lens. Microwave absorbing material is also placed within the waveguide such that any radiation from the coaxial source which is not incident upon the lens is absorbed. This microwave absorbing material is made from a composite of MnZnFe dispersed in a dielectric elastomer base, see section 3.3.

The end of this waveguide structure is placed on the metasurface to excite the surface waves via the diffracted fields produced at the waveguide exit. As well as producing the required surface wave some scattered free space radiation is produced the amount and form of which is strongly dependent on frequency and the metasurface structure. To characterise the operation of this device, referred to as a plane wave launcher (PWL), the near-field of the surface waves supported on a metallic patch ar-

ray metasurface, section 2.5.2, is measured using the spatial field mapping technique presented in section 3.6. As an illustration of the quality of the planar surface waves produced by this device a comparison of the phase fronts produced from the PWL described above with the phase fronts modelled from a dipole source at the same distance as shown in figure 3.13. Comparison of the curvature of the wavefronts indicates that the PWL has a bandwidth greater than 20 GHz.

3.7.1 Curvature Characterisation

The strength of the radiation along a line away from a cylindrical source of surface waves, such as the near-field coaxial antenna, is inversely proportional to the distance from the source, d, due to the expansion of the cross-sectional area of the wavefront. The curvature of the surface waves excited by the PWL device have been characterised by measuring the phase associated with the surface wave over the plane of the metasurface. The metasurface used for the characterisation of the curvature is the metallic patch array discussed in section 2.5.2. To calculate the radius of this curvature, x', first a parabola is fitted to the phase measured along each line parallel to the PWL exit face in the two dimensional plane. From this fit the central position is calculated, from the maximum in the phase, and the distance from the centre of the curvature, Δy for a given phase change $\Delta\phi$ is obtained. Then x' is calculated from:

$$x' = \frac{2\pi\Delta y^2}{8\Delta\phi} \tag{3.5}$$

The average radius of curvature for the system is then obtained by simply averaging the radius across all of the lines. This radius of curvature is then compared to the physical distance to the source within the PWL device which would be the radius of curvature is the lens was not present. Figure 3.14 shows the radius of curvature at the exit of the lens with the physical source distance subtracted. Therefore this illustrates the increased radius of curvature caused by the lens as a function of frequency. For all the frequencies measured the radius of curvature is significantly larger than the physical distance to the source within the PWL. However the lens works most effectively above 20 GHz, where the radius of curvature increases significantly. This curvature is used to apply a correction in the measurement of the reflection coefficient of a surface wave in section 3.8.

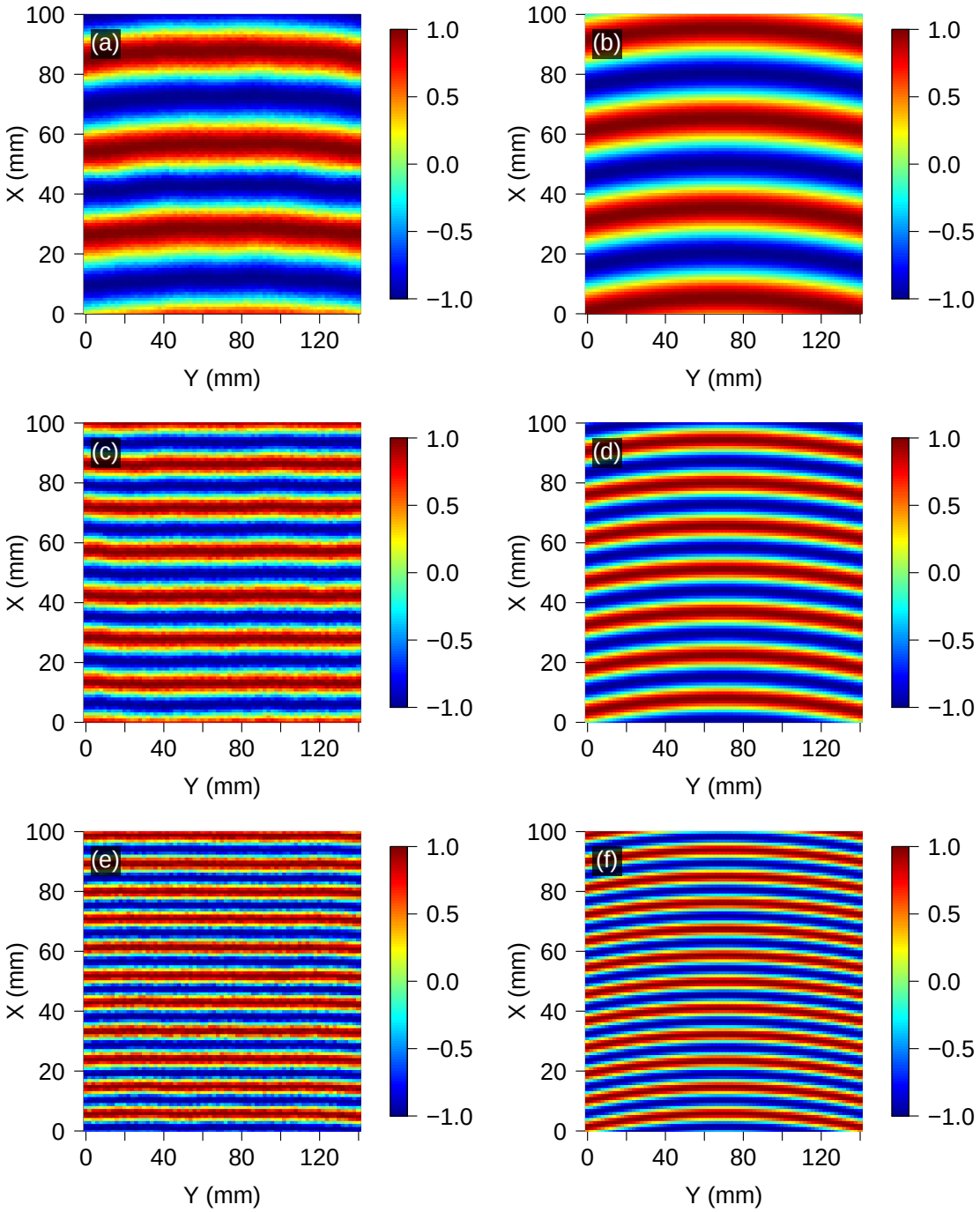

Figure 3.13: Comparison of the phase fronts of a surface wave on the metallic patch array, measured experimentally, (a,c,e) with the phase fronts of a surface wave modelled from a point source on the same surface, (b,d,f). Three frequencies are presented 10 GHz (a,b), 20 GHz (c,d) and 30 GHz (e,f).

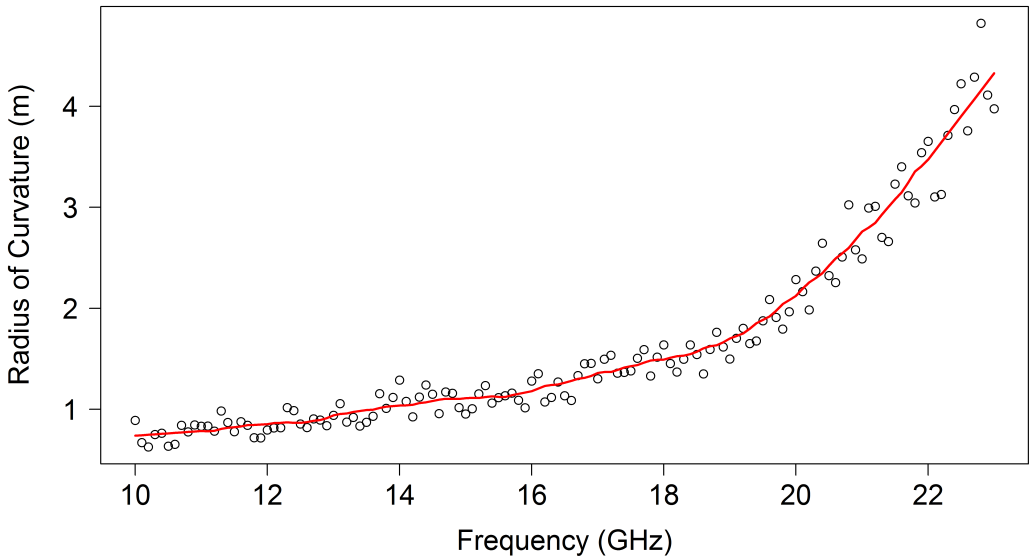

Figure 3.14: Radius of curvature of the phase fronts of the surface waves launched by the PWL with the physical source distance subtracted, illustrating the increased radius of curvature caused by the lens as a function of frequency.

3.8 Measuring the Reflection Coefficient of a Surface Wave

Determining the reflection coefficient of a surface wave, supported on a metasurface, incident upon a discontinuity is of interest for a variety of applications such as the characterisation of surface wave devices and evaluation of the performance of surface wave absorbing materials. As such a technique for determining the reflection coefficient of surface waves from any discontinuity has been developed using the spatial field mapping presented in section 3.6. The reflection coefficient of a surface wave incident upon a discontinuity is determined by examining the interference between the incident surface wave and the reflected one.

The instantaneous E_z-field is reconstructed by measuring both the time averaged field strength and the phase of the electric field. A fast fourier transform (FFT) is performed on the measured E_z-field to determine the relative amplitudes of the fourier components present in the measured electric field. The amplitude reflection coefficient is simply obtained from the ratio of the magnitude of the Fourier component whose wavevector corresponds to the reflected wave to that of the incident wave. The FFT is a form of a Fourier transform in which the integral over all wavevectors is replaced with a discrete sum with finite maximum values, this is done to allow solutions to be found for non-trivial spectra. The length of the spectrum analysed determines

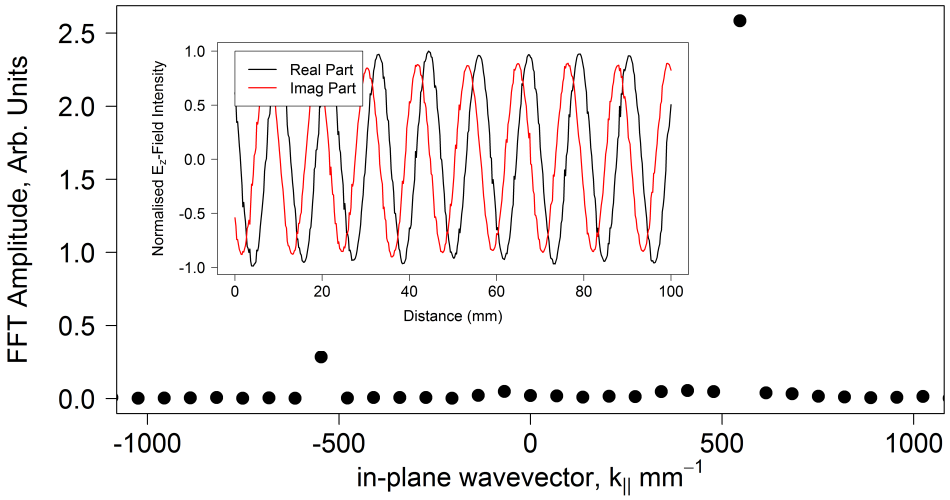

Figure 3.15: Example fast Fourier transform of the E_z-field showing the relative amplitudes of the forward and backward propagating waves. Inset:Corresponding E_z-field measured using the near-field coaxial probe reconstructed from the time averaged field amplitude and the phase.

the resolution of the wavevectors available within the FFT sum and the resolution of the spectrum determines the maximum wavevector within the sum. The wavevectors available within the FFT sum will be those whose wavevector corresponds to half wavelength quantisations along the length of the measured spectrum, $L = N\lambda/2$ where N is an integer and L is the length of the measured spectrum. If the wavevectors corresponding to the incident and reflected surface waves are not present within the FFT sum then the incorrect reflection coefficient will be measured. To ensure the required wavevectors are within the FFT sum a peak finding algorithm is used to find the position of the interference peaks in the spectra, which has been passed through a smoothing algorithm [132]. The measured spectrum is then truncated at the positions of the first and last peaks to ensure that the optimal $L = N\lambda/2$ condition is used, an example of the measured intensity and corresponding FFT spectrum is shown in figure 3.15.

3.8.1 Application of the Curvature Measurement

The residual curvature in the surface wave phase fronts excited by the PWL has an effect on the measured reflection coefficient of a surface wave incident upon a planar discontinuity on a metasurface. The curvature associated with the PWL source reduces

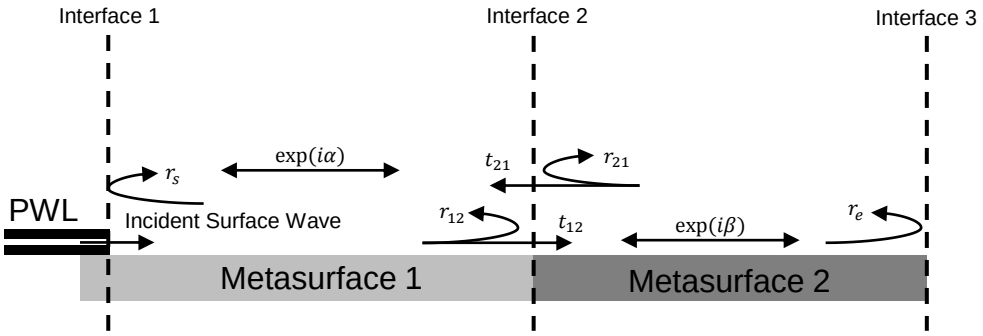

Figure 3.16: Schematic of the example system of a surface wave incident upon the discontinuity between two metasurfaces.

the amplitude along a line perpendicular to the waveguide exit due to the expansion of the surface wave phase fronts area, see section 3.7. The measurement of the interference between the incident and reflected surface wave begins at a distance, d, from the reflecting discontinuity and has length l. Since the surface wave amplitude is decaying along the direction of propagation the amplitude of the surface wave incident on the discontinuity is lower than that measured at distance d. The amplitude of the wave incident upon the planar discontinuity, A', is derived from the radius of curvature of the surface wave phase fronts, R_0, at the distance d from the discontinuity and the amplitude of the surface wave at distance d from the discontinuity A.

$$A' = \frac{AR_0}{R_0 + d} \tag{3.6}$$

The reduction of the amplitude of the surface wave incident upon the discontinuity leads to a reduced amplitude reflected surface wave. The measured reflection coefficient, r', is reduced from the true reflection coefficient, r, by the same factor as the surface wave amplitude. A simple correction is possible to determine the amplitude reflection coefficient of the discontinuity from the measured reflection coefficient.

$$r' = r\left(\frac{AR_0}{R_0 + d}\right) \;\; \therefore \;\; r = r'\left(\frac{R_0 + d}{AR_0}\right) \tag{3.7}$$

3.8.2 Reflection Coefficient and Fabry-Perot Effects

Measurement of the reflection coefficient of surface waves incident upon a discontinuity has several inherent difficulties which must be considered. In order to present these difficulties in a coherent manner the example system shown in figure 3.16 will be considered. The example system involves the measurement of the reflection coefficient of

a surface wave incident upon a change in the metasurface supporting the surface wave. The surface waves are excited using the PWL described in section 3.7 and are normally incident onto the planar discontinuity. The reflection coefficient of interest is r_{12} and the effect on the measured reflection coefficient of two difficulties inherent to this system shall be considered. Firstly the effect of the Fabry-Perot like cavity between interface 1 and interface 2 on the measured reflection coefficient shall be analysed. Secondly the effect of the transmission through interface 2, t_{12}, and the subsequent reflection, r_e, on the measured reflection coefficient shall be considered.

Throughout this section the Fresnel equations shall be used; however these equations are designed to be used in free space where the two possible channels through which power can leave the interface are reflection and transmission. For surface waves there is an additional mechanism present at each boundary, scattering to free space. The modal matching requirements at a planar discontinuity induces scattered EM radiation which propagates into the dielectric half space above. Often, in free space, a simplification of the reflection coefficient for a complex system is performed using the knowledge that the reflection and transmission coefficients must sum to unity. However in the case of surface waves these simplifications cannot be performed. Therefore within this section the scattering mechanism is considered to be a loss channel at each interface and the reflection and transmission coefficients no longer sum to unity.

3.8.2.1 Reflection Coefficient within a Fabry-Perot Cavity

The field profile within the PWL used in this thesis is significantly different from that of the surface waves supported on metasurfaces, since one is a parallel plate waveguide mode and the other confined to the metasurface interface. Therefore considering a surface wave incident upon the termination of the PWL the modal matching requirements will produce surface wave reflection, waveguide transmission and scattering to free space. From this surface wave reflection, r_s, it can be seen that a Fabry-Perot-like cavity is present between the interface of interest, interface 2, and the PWL, interface 1. It is therefore important to determine the effect of this cavity, if any, on the measured reflection coefficient, r_{12}. In order to determine the effect of this cavity it shall be assumed that $r_e = 0$.

It is possible to write the forward and backward propagating surface waves supported on metasurface 1 as two separate sums which are then simplified using a similar derivation to that provided in appendix A. The forward propagating component is given by equation 3.8 and the backward component by equation 3.9. The relationship between these components is shown in equation 3.10 and therefore the modification to the reflection coefficient is $\exp(i\alpha)$. Since $|\exp(i\alpha)| = 1$ the magnitude of the reflection

coefficient is unaffected by the cavity and the measurement of the local electric field only contains information about the $|r_{12}|$.

$$\psi_f = \frac{1}{1 - r_{12} r_s \exp(2i\alpha)} \tag{3.8}$$

$$\psi_b = \frac{r_{12} \exp(i\alpha)}{1 - r_{12} r_s \exp(2i\alpha)} \tag{3.9}$$

$$\psi_b = \psi_f r_{12} \exp(i\alpha) \tag{3.10}$$

3.8.2.2 Effect of Subsequent Reflections

The effect of the transmission, t_{12}, and the subsequent reflection, r_e, on the measured reflection coefficient shall now be considered. The reflection coefficient for a system within which there are two reflecting interfaces is determined in appendix A, the equation for the total amplitude reflection coefficient from a two interface system is equation A.4, into which we have substituted the relevant symbols for the system shown in figure

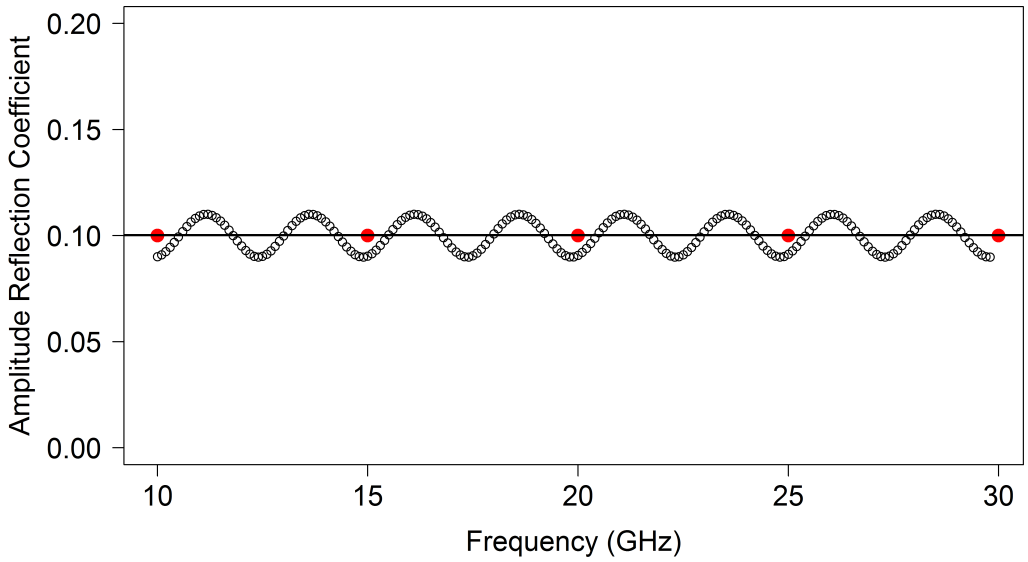

Figure 3.17: Effect on the measured reflection coefficient, r_m, of a subsequent reflection, r_e of the transmitted component showing the varying period oscillation (black points). Mean of the reflection coefficient (black line) and the actual amplitude reflection coefficient (red points), all analytical data.

3.16. Then

$$r_m = r_{12} + \frac{t_{12}t_{21}r_e exp(2i\beta)}{1 - r_{21}r_e exp(2i\beta)} \tag{3.11}$$

where r_m is the measured amplitude reflection coefficient.

Extracting the reflection coefficient r_{12} is not a trivial exercise, unless $r_e = 0$, it is therefore necessary to consider the system numerically. The reflection coefficient, r_m, has a complex form which has been numerically calculated, the reflection and transmission coefficients used are non-dispersive as a function of frequency, figure 3.17. This function becomes significantly more complex once the dispersion of the individual interface reflection and transmission coefficients is included in the equations. It can be seen that the measured reflection coefficient oscillates as a function of frequency, this is due to the constructive and destructive interference of the surface wave reflected from interface 3, r_e, with the reflection from interface 2, r_{12}. An increased reflection coefficient is measured when the interference is constructive and a decreased reflection coefficient is measured when the interference is destructive. For small subsequent reflection coefficients it can be seen that the reflection coefficient r_{12} is approximately the mean of the oscillating total reflection coefficient, r_m. As such great care is taken within the experiments performed throughout this thesis to reduce the magnitude of r_e through the use of microwave absorbing materials.

3.9 Conclusions

In this section the numerical, analytical and experimental techniques developed and used for the characterisation of the surface waves supported on metasurfaces are presented. In section 3.2 the FEM techniques used to efficiently design metasurface structures and to measure the reflection coefficient of surface waves incident upon planar discontinuities has been discussed. A system for characterising the material parameters of composite materials in the microwave regime has been presented in section 3.3. A new technique for measuring the dispersion of metasurfaces is presented in section 3.5, a system for measuring the near-field associated with the surface waves in section 3.6 and a device for launching planar phase front surface waves in section 3.7. Finally a discussion of the measurement of surface wave reflection and the difficulties involved is present in section 3.8. These techniques are used throughout this thesis to characterise the surface waves supported on metasurfaces and the reflection coefficients of various planar discontinuities including the termination of metasurfaces to free space, the addition of a dielectric overlayer onto a metasurface structure and a change in the metasurface structure.

Chapter 4

Surface Wave Resonances Supported on a Square Array of Square Metallic Pillars

4.1 Introduction

In this chapter the surface wave properties of a new metasurface, a square array of square cross section metallic pillars on a metallic ground plane, have been characterised using the experimental technique described in section 3.5. The structure presented within this section has been developed from the study of a sub-wavelength hole array analytically considered by Pendry et. al [20] and experimentally characterised by Hibbins et. al. [14] and later extended by Rance et. al. [49]. Studies on a 1D array of grooves have been completed by Garcia-Vidal et. al. [133] and Rance et. al. [134]. Analytically the 1D array of grooves has been considered as an effective medium on a metal ground plane in [133] where it is shown that the grooves can be considered to be an anisotropic layer. This anisotropic layer on a ground plane is shown to support bound modes whose dispersion asymptotes to the resonance of the waveguide modes supported by the grooves.

The square array of square cross-section metallic pillars considered here is the complimentary structure of the sub-wavelength hole array placed on a metal ground plane. The square array of square cross-section metallic pillars can also be described as two arrays of wax-filled slits which are orthogonal to one another and shall henceforth be referred to as a bi-grating. The dispersions of the surface modes supported on the sub-wavelength hole array are determined by the waveguide modes (i.e. the geometry and the material filling the hole) supported within the holes and it will be shown that

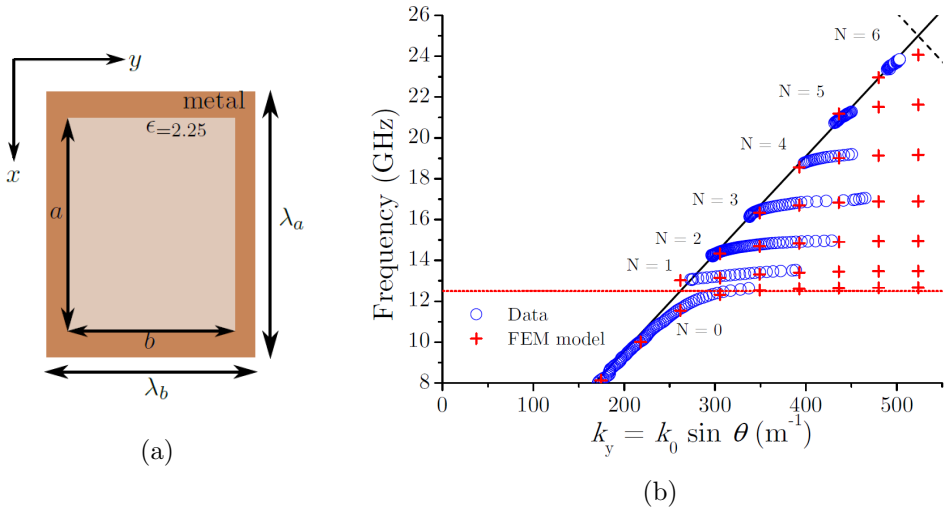

Figure 4.1: a) Schematic of the unit cell of the rectangular array of rectangular dielectric-filled waveguides. The long pitch of the tube $\lambda_a = 9$ mm and the orthogonal shorter pitch $\lambda_b = 6$ mm with the inner dimensions $a = 8$ mm and $b = 5$ mm. b) Experimentally measured dispersion (circles) together with predicted eigenmode solutions (crosses) of the family of surface modes supported on the structure shown in figure 4.1a at $\phi = 0^o$ (along the y-axis). The red dashed line represents the cutoff frequency of the rectangular waveguide and the solid black line is the light line. Reproduced with permission from [135].

the dispersions of the surface modes supported on the bi-grating are also determined by the waveguide modes within the structure. The dispersion of these modes has been compared to an analytical description of the surface modes supported on an idealised single grating structure, with infinitely thin metal walls. The reflection coefficient of surface modes incident upon the termination of the bi-grating to free space has also been fully characterised as a function of frequency. This reflection coefficient has been shown to have features associated with the surface waves supported on the bi-grating.

4.2 Background

It has been shown (chapter 2) that subwavelength structuring of the metal surface produces surface-wave field confinement at microwave frequencies. One such structure, which has received significant attention, is the sub-wavelength hole array which supports bound surface modes [14, 20, 49], where the lowest frequency surface mode is asymptotic to the cutoff frequency, ν_{cutoff}, of the holes. The cutoff frequency is defined as the frequency below which no propagating modes exist within the subwavelength holes. For frequencies below the cutoff frequency the decay length into the subwave-

length holes is much greater than the skin depth of the unstructured metal thereby allowing the textured metal surface to become rather like the 'poorer' conductor it is at optical frequencies [14]. This leads to much tighter confinement of this surface wave, analogous to the surface plasmon polariton supported at visible wavelengths [20]. Of course, above ν_{cutoff} there are a family of transverse electric (TE) waveguide modes (see section 3.3), which are quantised (along the waveguide length (z)) due to the onset of propagating solutions, within the holes. A family of surface waves may then be supported with asymptotic frequencies defined by this quantisation in z, as shown in figure 4.1b (circles and crosses labelled $N = 1, 2, 3...$).

In contrast to the hole array discussed above, a square array of subwavelength square cross-section metal pillars on a conducting ground plane supports transverse electromagnetic (TEM) waveguide modes within the slits that have no lower cut-off frequency. However the TEM waveguide modes supported within the slits are also quantised in the z-direction, which again leads to a family of bound surface waves with asymptotic frequencies equal to the resonant frequencies of the modes in the slits. These waveguide modes are analogous to the waveguide modes supported between a pair of parallel metal plates. The slit structure will give a response which is similar to that of the higher order waveguide modes supported above the cut-off frequency of the aforementioned hole array [13, 47, 49, 136], where the lowest energy quantisation will occur when a quarter wavelength resonance is supported in the slit cavity.

4.3 Experimental Observations

The experimental sample is created from a single block of aluminium 460 mm × 460 mm in the x and y directions, with square bottomed slits cut to a depth $h = 30$ mm with all of the resulting square metallic pillars remaining connected via a metal base (ground plane), figure 4.2. Each square cross section pillar has side lengths of $w_p = 3$ mm with the slit width between pillars being $w_s = 1$ mm, figure 4.2a. The pitch of the structure is 4 mm in both the x and y directions giving the onset of diffraction in the air above the sample as $\nu = 37.5$ GHz, for grazing incident radiation at azimuthal angles of $\phi = 0^o$ or 90^o. We consider only non-radiating surface modes (i.e. modes which lie to the right of the light line) in this study and therefore it is straightforward to increase the onset of diffraction (to further increase the range of the non-diffracting domain) by changing the azimuthal angle to $\phi = 45^o$. At this angle the onset of diffraction occurs at $\nu = 53$ GHz because the distance between the diffraction planes reduces by a factor of $\sqrt{2}$. To decrease the resonant frequencies of the modes within the slits, the slits are filled with paraffin wax ($\epsilon_r \approx 2.38$), thereby increasing the number of modes available for study in the non-diffracting regime. The dispersions of the surface modes

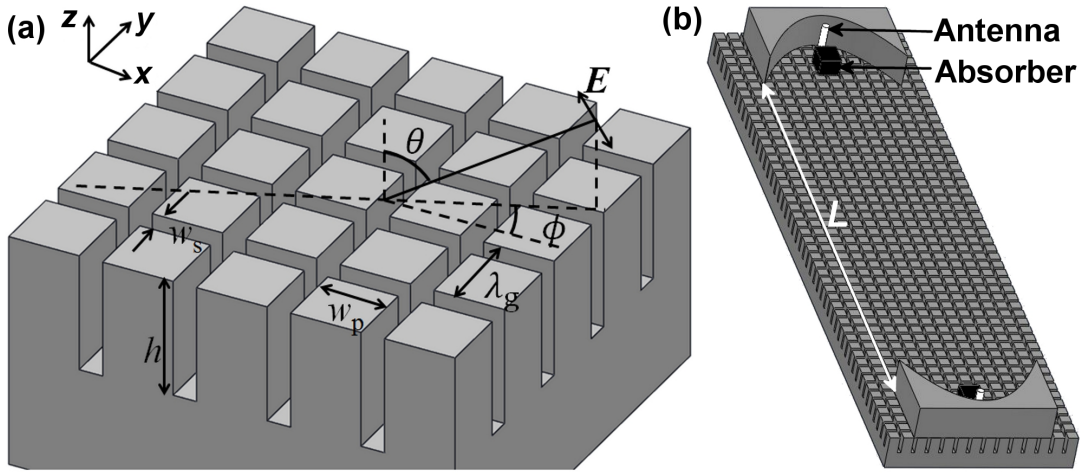

Figure 4.2: Schematic diagrams of the a) bi-grating structure. b) the experimental setup, white cylinders indicate the position of the antenna and the black boxes indicate the position of the absorbers

supported by this structure are measured using the technique described in section 3.5. This involves measuring the phase of the surface wave using a near-field coaxial probe at two different positions and looking at the phase change between them.

The modes of the system are related to quantisation of the electromagnetic field within the depth of the slits. Boundary conditions for such resonances are an approximate E-field maximum at the top surface and an E-field minimum at the ground plane. Therefore these resonances occur whenever the external wavelength approaches the condition given by equation 4.1.

$$\lambda = \frac{4h\sqrt{\varepsilon_r}}{(2N-1)} \tag{4.1}$$

Where N is an integer, h is the depth of the slits and ε_r is the permittivity of the material filling the slits. This sets up a resonant standing wave in the cavity and no power propagates across the sample since all of the power is localised within the cavity resonance. Where the cavity resonance of the slits crosses the dispersion of the grazing photon, indicated by the light line, an anti-crossing of the modes occurs due the hybridising of the cavity resonance with the grazing photon. Thus a family of surface waves are supported with asymptotic frequencies equal to those of the cavity resonances which, because of the square symmetry, are largely unaffected by the azimuthal angle of the sample. Modelled fields of the first four modes, from left to right, supported by the system are shown in figure 4.3b, calculated using a finite element method (FEM) modelling package [96].

From figure 4.3, it is clear that the group velocity of each mode decreases as the

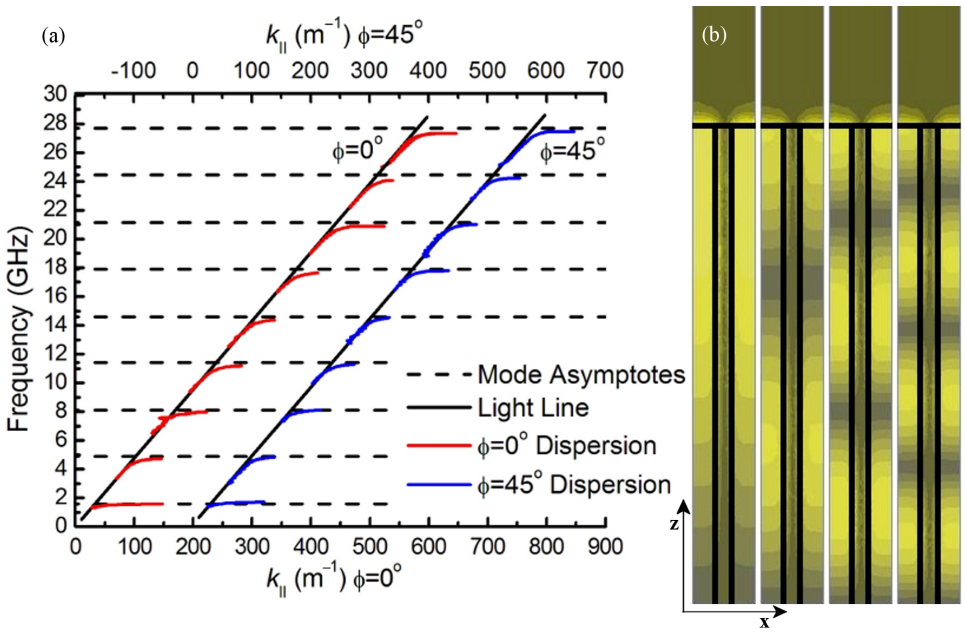

Figure 4.3: a) Plot showing the experimental dispersion of the first nine modes of the structure together at $\phi = 0^o$ (red) and $\phi = 45^o$(displaced by $+200k_{||}$) (blue) with the predictions of the resonant frequencies from numerical modelling (horizontal dashed lines). b) Plots of the time averaged electric field strength in the centre of the slits parallel to the x-axis for the first four modes at the resonant frequency of the mode ($k_x = 1570\ m^{-1}$ BZ boundary), where light indicates high field and dark low field.

resonant condition of the slit is approached tending to zero at the asymptote of the surface wave dispersion. This decrease in group velocity and associated increase in surface wave absorption eventually leads to a complete loss in received power at the near-field antenna as the mode approaches the asymptote preventing the quantification of the dispersion very close to the resonant frequency of the slit. The dispersion of the modes measured at both $\phi = 0^o$ and $\phi = 45^o$ are nearly identical, showing the azimuthal independence. Further, both agree extremely well with both the shape of the dispersion and the asymptotes obtained from FEM modelling as illustrated by figures 4.3 and 4.4. In addition the electromagnetic fields shown in figure 4.3 illustrate clearly the quantisation, below the surface, as well as the obvious surface wave character of the modes, shown by the decaying field above the surface.

Figure 4.4 shows in detail the measured and predicted dispersion of the first and second modes demonstrating that these are surface-wave-like in character with wavevectors extending well beyond the light line. This also shows the agreement between the shape and position of the FEM dispersion curve and the experimental data. The lowest order mode is only measured from frequencies above about 1.3 GHz as the wavelength

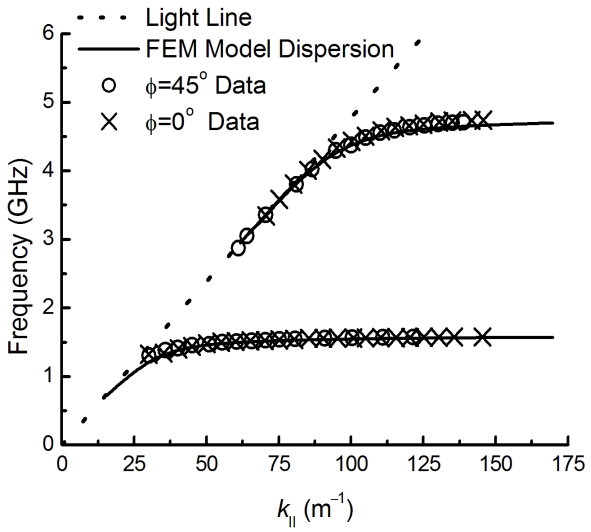

Figure 4.4: Plot of the dispersion for the first two modes of the structure at both azimuth angles $\phi = 0^o$ (crosses) and $\phi = 45^o$ (circles) along with the FEM modelled dispersion (black lines).

of the microwaves (23 cm) is now becoming comparable to the overall size of the system, $L \sim 30$ cm.

The electric field profile of the first four modes, shown in figure 4.3, is presented in more detail in figure 4.5. The electric field strength along a line in the z-direction within the slit orientated along the y-axis, at $x = \lambda_g/2$ and $y = \lambda_g/4$, is extracted from FEM modelling. The quantisation of the electric field within the depth of the slit is shown along with the evanescent decay of the electric field away from the metasurface interface, situated at approximately 30 mm (dashed line). The decay length of the electric field perpendicular to the metasurface is the same for each of the 4 modes as the field is extracted at the Brillouin Zone (BZ) boundary and therefore the in-plane wavevector is identical for each of the modes.

The electric field strength is also extracted for the second order surface mode propagating in the x-direction with $k_x \approx 1300\ m^{-1}$ ($f \sim 4.79$ GHz) in the xy-plane at $z = h/2$ and is shown in figure 4.6. The field is shown to be mostly restricted to the slits perpendicular to the direction of propagation of the surface wave along the metasurface. When the surface wave is propagating along the x-axis (at $\phi = 0^o$) the electric field is mostly excluded from the slits whose orientation is parallel to the x-axis due to the boundary conditions imposed by the metal walls. Propagating modes are only supported within the parallel slits above the frequency of the first quantisation across w_s since the tangential E-field must fall to zero at the slit walls, as such the cutoff

frequency (fitting in $\lambda/2$) for these modes is approximately 97 GHz.

4.3.1 Analytical Dispersion

The surface mode supported on the bi-grating structure is similar to that supported by a single grating when the mode is propagating perpendicular to the direction of the slit. In this case it has just been shown that the electric field is mostly excluded from the slits parallel to the direction of propagation and hence the response of the bi-grating metasurface can be compared to that of a single grating.

An air-filled, single grating with infinitely thin walls has been analytically considered in section 2.3.2. For this single grating a family of TM surface modes is supported with asymptotic frequencies defined by the resonances of the truncated parallel plate waveguides, figure 4.7. These resonances occur when the depth of the grating is equal to $(2N-1)\lambda_0/4$, where N is an integer and λ_0 is the free space wavelength, and as such they are equivalent to the resonances supported by the bi-grating since it is comprised of a pair of orthogonal slits. The azimuthal independence of the bi-grating, shown in figure 4.3, arises from the four-fold symmetry of the square sub-wavelength unit cell which leads the sample to nearly appear isotropic. In the single grating case the sample

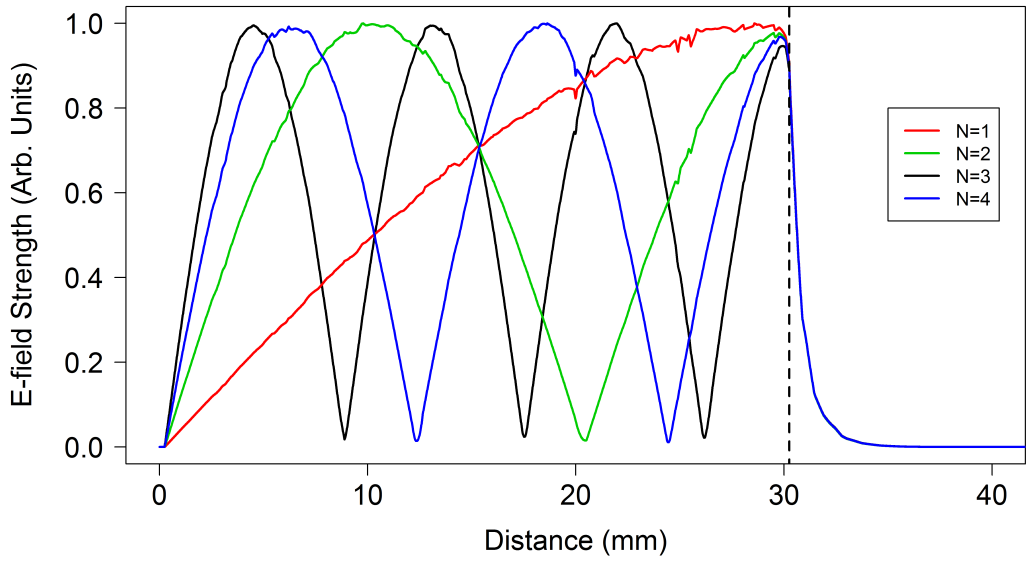

Figure 4.5: FEM predicted electric field strength, along a line in the z-direction at $x = \lambda_g/2$ and $y = \lambda_g/4$, of the first 4 modes of the bi-grating structure at the BZ boundary. The first mode (N=1) is shown in red, the second (N=2) in green, the third (N=3) in blue and the fourth (N=4) in black. The interface of the metasurface is at approximately 30 mm indicated by the dashed line.

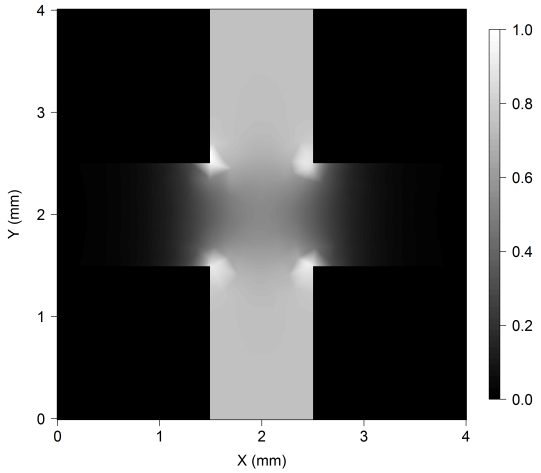

Figure 4.6: Greyscale plot of the time averaged electric field strength in the xy-plane associated with the second order mode at ~ 4.79 GHz at $\phi = 0^o$ where white indicates high field strength and black indicates low field strength.

is highly anisotropic due to the fact that the system is only periodic in one direction.

A comparison of the dispersion of the second order mode supported on the bi-grating and the idealised single grating, whose asymptotic frequency is defined by the $h = (3/4)\lambda$ resonance within the slits, is presented in figure 4.8. Whilst the asymptotic frequencies for the mode supported on the bi-grating and that predicted from the single grating structure are similar, the change of the group velocity of the surface waves with respect to ω, equivalently $\partial^2\omega/\partial k^2$, is significantly different for these two structures. It has been shown, using an array of sub-wavelength holes, that the exact dispersion of the surface modes supported on a metasurface are strongly dependent on the evanescent near-fields associated with the structure [45]. The idealised single grating considered analytically is significantly different from the bi-grating which, whilst only providing a minor perturbation to the resonant frequencies, leads to vastly different evanescent fields for the two structures. This difference in the evanescent fields makes exact comparison of the form of the dispersion curves irrelevant since the rate of change of the dispersion curve close to the asymptotic frequency is dominated by the evanescent fields associated with the structure, as can be seen in figure 4.8.

4.4 Surface Wave Reflection Coefficient of the Bi-grating Termination

The reflection coefficient of a surface wave incident upon the termination of the surface on which it is supported (to free space) is determined primarily by the dispersion of

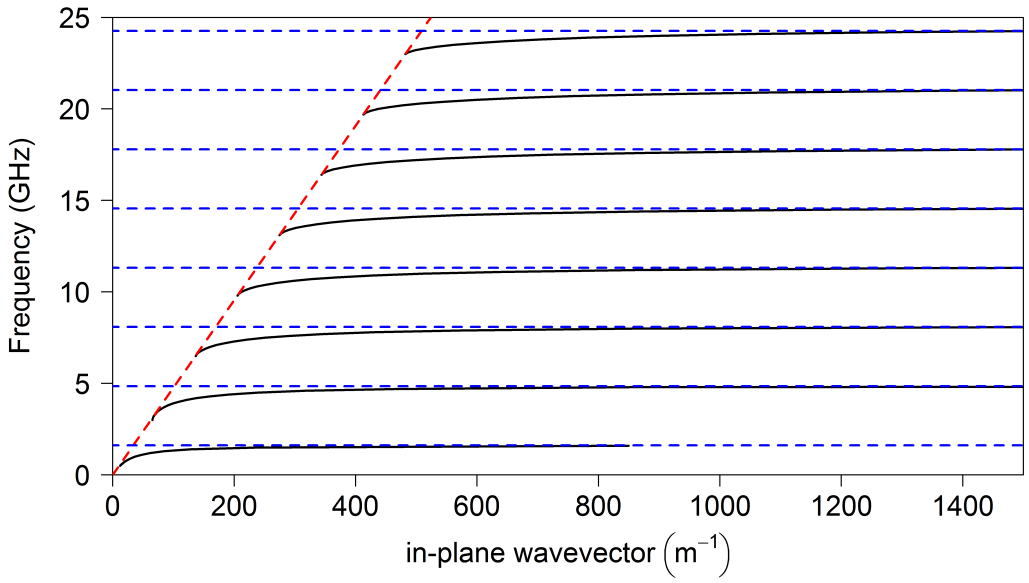

Figure 4.7: The dispersion of the surface modes (black lines) supported on a corrugated metallic ground plane derived from the analytical expressions presented in section 2.3.2. Here the analytical method only solves for in-plane wavevectors greater than k_0. The red line indicates the light line and blue dashed lines the resonant frequencies of the slits.

the surface waves supported on the structure. This is because the amplitude of the reflection coefficient is related to the confinement of the surface wave in the z-direction above the metasurface. This confinement is defined by the k-vector perpendicular to the interface, k_z, which is directly related to the k-vector of the surface wave in the direction of propagation, k_x, since the total k-vector, k_0, is fixed by the frequency of the surface wave and $k_0^2 = k_x^2 + k_z^2$. As such the reflection coefficient of the bi-grating structure is expected to contain a significant number of features associated with the dispersion of the family of surface modes supported. Accurate determination of the amplitude reflection coefficient of a surface wave incident upon the termination of the bi-grating structure to free space has been made possible by utilising the plane wave launcher (PWL) described in section 3.7, and the measurement method described in section 3.8.

The measured reflection coefficient exhibits a series of amplitude reflection coefficient peaks, at frequencies associated with the family of surface modes supported on the bi-grating, figure 4.9. Peaks in the amplitude reflection coefficient are coincident with the asymptotic frequencies of the surface waves supported. The reflection coefficient of a surface wave incident upon the termination of this structure is related to the

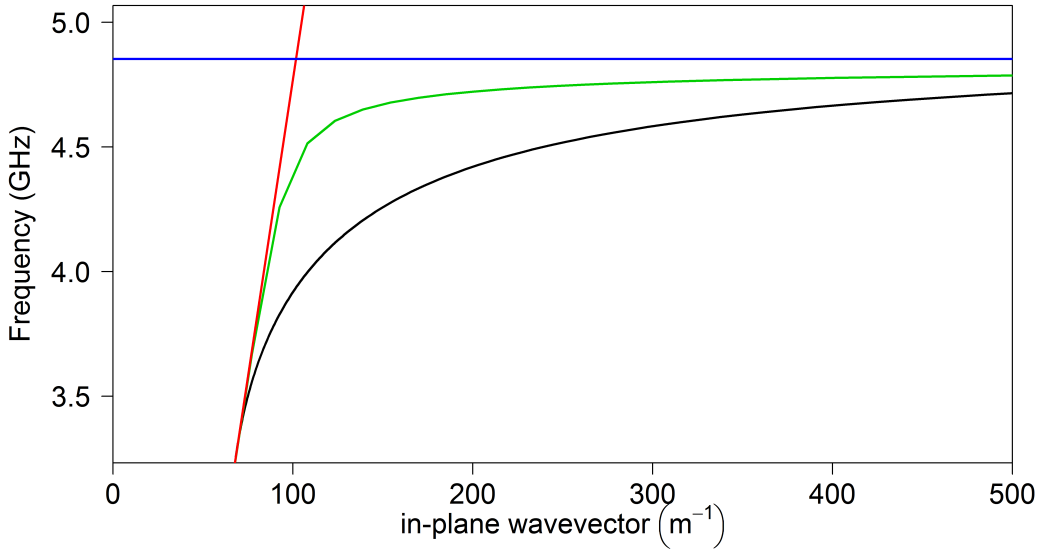

Figure 4.8: Comparison of the dispersion for the second order mode obtained from FEM modelling (green line) with the analytically derived dispersion for a corrugated ground plane with similar parameters (black line). The light line is shown (red line) as is the predicted asymptotic frequency for the mode (blue line).

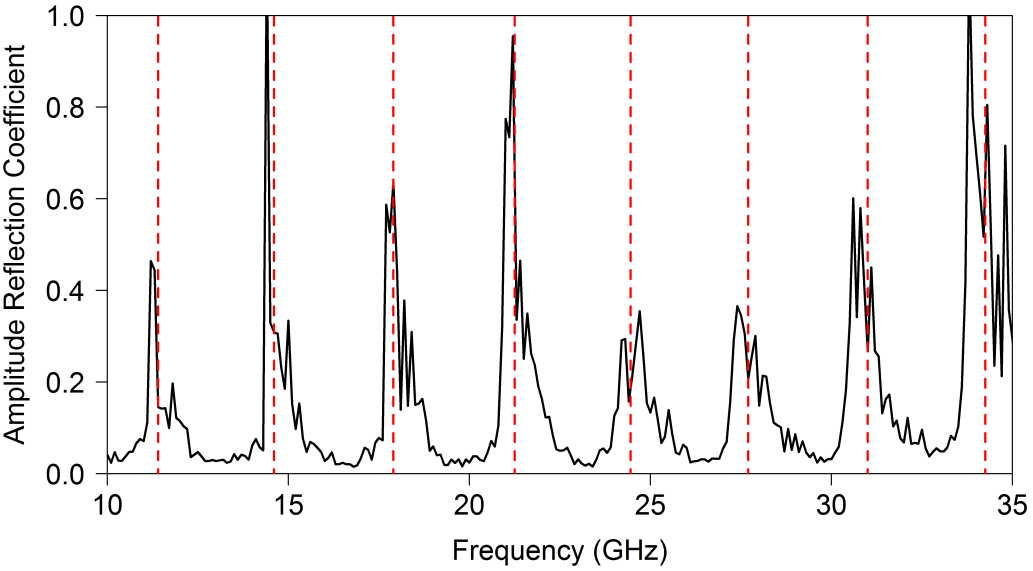

Figure 4.9: The amplitude reflection coefficient of surface waves incident upon the termination of the bi-grating metasurface to free space. The red dashed lines represent the surface wave mode asymptotic frequencies.

confinement of the surface wave to the metasurface interface, since no power propagates below this interface. No power propagates along the slits parallel to the direction of propagation for frequencies below the cutoff frequency of these slits (97 GHz). This confinement is defined by the imaginary k-vector perpendicular to the interface, k_z, which is directly related to the k-vector of the surface wave in the direction of propagation, $k_{||}$, since the total k-vector, k_0, is fixed by the frequency of the surface wave with $k_z = \sqrt{k_0^2 - k_{||}^2}$. At frequencies where the surface wave fields decay many wavelengths into the dielectric above, i.e. in-plane wavevectors close to k_0, the reflection coefficient of the termination is near-zero. Whilst at frequencies where the surface wave fields decay rapidly away from the interface, $k_{||} \gg k_0$, the reflection coefficient is large. Since this change in the in-plane wavevector occurs within a narrow range of frequencies this leads to a sharp rise in the amplitude reflection coefficient over this narrow range of frequencies.

The asymmetric shape of the reflection coefficient peaks is explained by the dispersion of the surface waves. It can be seen in figure 4.3 that above the asymptotic limit of each of the surface waves there exists a frequency band where no surface wave is experimentally measured or predicted by FEM modelling. At these frequencies the mode exists within the light line and is therefore considered a 'leaky mode'. These modes originate at $k_x = 0$ and disperse from there to the light line with increasing frequency to become the surface waves. Since these modes are not surface waves their reflection coefficient is undefined in this system. It can be seen that as the mode crosses the light line and becomes a surface wave the reflection coefficient is near-zero.

This structure served as a test-bed for experimental technique development and similar investigations can now be performed with thin, lightweight metasurfaces which support surface waves in the microwave regime as discussed in Chapters 5, 6 and 7.

4.5 Conclusion

In conclusion the dispersion of surface waves on a square array of square cross-section metal pillars has been fully characterised and compared to FEM modelling. The results show that a family of surface waves may be supported by pillar or crossed slit structures. A family of TM surface modes have been shown to exist with dispersions which asymptote to frequencies defined by the pillar heights (slit depth) and the refractive index of the material filling the slits. The amplitude reflection coefficient of surface waves incident on the termination of this metasurface to free space have also been characterised. A series of amplitude reflection coefficient peaks are shown to exist close to the surface wave asymptotes associated with standing waves defined by the depth of the bi-grating structure.

Chapter 5

Determining the Reflection Coefficient of Microwave Surface Waves on Metasurfaces Terminated to Free Space

5.1 Introduction

The determination of the reflection coefficient of a surface wave incident upon a device or a discontinuity in the surface is important in characterising the performance of devices and methods used for the control of radar cross section. The reflection coefficient and scattering from a terminated surface, represented by an impedance approximation, has been theoretically studied [80, 81] for the two limiting cases of high and low surface reactance. Experimentally, however, there has been little published work while a theoretical study of such a system including a full analytical description including the fields within the metasurface structure has not been done. It shall be shown that this shortcoming of the analytical descriptions of the metasurfaces can lead to the prediction of incorrect surface wave reflection coefficients. The purpose of this work is to experimentally determine the microwave surface wave reflection coefficient for such a system and compare the results to those obtained by finite element method (FEM) modelling as well as analytic theory. The scattered field at the termination is also experimentally characterised and compared with FEM modelling. It is shown that the scattered radiation is in a lobe of power scattered at small angles with respect to the plane of the metasurface.

Surface waves are supported on many different metasurfaces at microwave frequen-

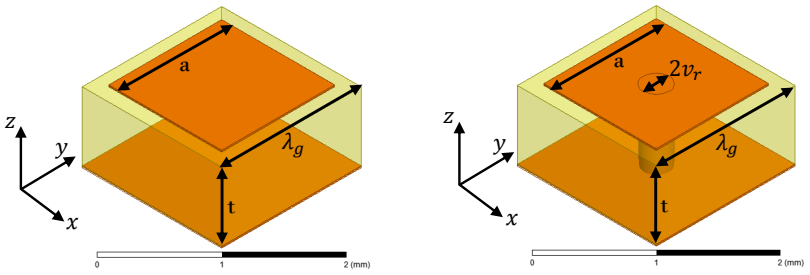

(a) (b)

Figure 5.1: Schematic of a unit cell of the metasurface structures used in this study where the orange represents metal and yellow indicates the edge of the dielectric; a) square array of square metallic patches on a dielectric coated metallic ground plane and b) Sievenpiper 'mushroom' array, which has a metal via connecting the metal patch to the ground plane.

cies [14, 20, 41, 47, 49, 71] the dispersion of these surface waves being defined by the nature of the metasurface structure. The dispersion of surface waves supported on simple metallic patch arrays, section 2.5.2, as well as Sievenpiper 'mushroom' metasurfaces, section 2.5.3, have been well documented and are significantly different [44, 71]. The unit cells of each of these two structures are shown in figure 5.1 and the surface wave dispersions, predicted using the eigenmode solver in HFSS, section 3.2, for each metasurface studied here are shown in figure 5.2 and discussed in detail in section 2.2. The pitch of the square array is $\lambda_g = 1.6$ mm, the side length of the patches is $a = 1.3$ mm and the dielectric thickness $t = 787$ μm in both cases and the via radius $v_r = 150$ μm for the Sievenpiper structure. Arrays of area 60 cm by 40 cm were fabricated and explored over the frequency range of 10 to approximately 30 GHz.

The reflection coefficient of surface waves incident upon the termination of a metasurface to free space has been characterised using the near-field mapping technique, discussed in section 3.6, to characterise the surface wave with the experimental analysis method described in section 3.8. The magnitude of the reflection coefficient of the surface waves depends strongly on the boundary conditions associated with the local environment of the termination. The boundary conditions imposed in this case are shown in figure 5.3. A metal boundary extends infinitely into the lower half-space connected to the ground plane of the metasurface. Practically this has been achieved by electrically connecting the ground plane of the metasurface to an L-shaped section of aluminium, the electrical connection was created using a silver epoxy.

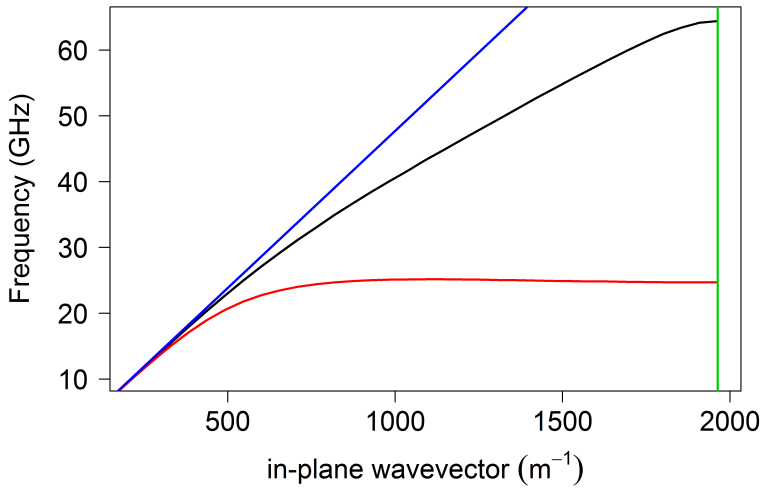

Figure 5.2: Dispersion of the transverse magnetic surface mode for the square array of square metallic patches on a dielectric coated metallic ground plane (black line) and a Sievenpiper 'mushroom' array (red line). The dispersion of a grazing photon, the light line, is shown (blue line) as is the Brillouin Zone boundary (green line) due to the periodicity of the lattice.

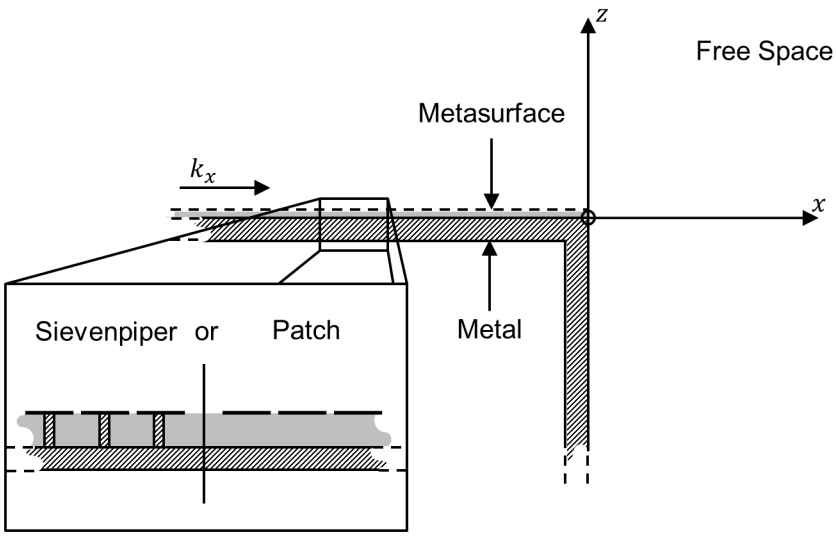

Figure 5.3: Schematic of the termination of a metasurface to free space. The patterned region indicates the L-shaped metal support.

5.2 Measurements of the Scattered E-field

Measurements of the scattered E-field from the termination of a square array of square metallic patches on a dielectric coated metallic ground plane and Sievenpiper 'mushroom' array to free space is also performed using the same 3-axis translation stage, section 3.6, and near-field stripped coaxial antennas, section 3.4. At the termination of the metasurface scattering is the only mechanism by which power can be lost from the reflected surface wave since there is not a second surface to support a transmitted surface wave. The scattered radiation is predominately in a lobe of power scattered at low angles close to the x-axis with a small angular spread both of which depend on the frequency of the incident surface wave. A qualitative comparison of the measured E_z-field with that obtained from FEM modelling is performed and show good agreement.

The physical size of the antenna restricts the proximity to the metasurface and the metal boundary which can be obtained. The width of the antenna sheath restricts the distance to the metal boundary to be no less than 1.5 mm (including a 0.5 mm gap) and the length of the antenna restricts the measurement position, the centre of the antenna exposed length, to no closer than 2.5 mm (including a 0.5 mm gap) from the metasurface. This creates a region close to the metasurface and metal boundary where the field cannot be characterised. In the field profiles presented throughout this chapter this region is indicated in grey and the physical position of the metasurface and metal boundary by the black rectangles.

Measurement of the scattered field from the termination of the metasurface is very sensitive to the orientation of the coaxial line of the antenna. Measurement of the z-component of the electric field is desired to determine the form of the scattered wave. The metallic sheath of the coaxial line creates a significant perturbation to the electric field in certain orientations which must be avoided in order to obtain an accurate field map. It is clear that at the metal boundary, at $z < 0$ $x = 0$, the tangential component of the electric field, E_z, must fall to zero. With the antenna orientated perpendicular to the metasurface, figure 5.4a, the data shows an apparent maxima at the metal boundary at $z = -7$ mm $x = 0$ in figure 5.5a. This is clearly unphysical and is caused by the orientation of the antenna. In this orientation whilst the dipole antenna is in the low field region below the interface the metallic sheath of the coaxial line is in the large electric field of the scattered radiation. This causes significant scattering of the electric field and allows surface currents to flow along the conducting sheath to the dipole antenna. This leads to an incorrect measurement of the electric field strength.

Two alternative antenna orientations are possible whilst still keeping the sensitivity of the dipole to E_z only; which often involves bending of the exposed length. The

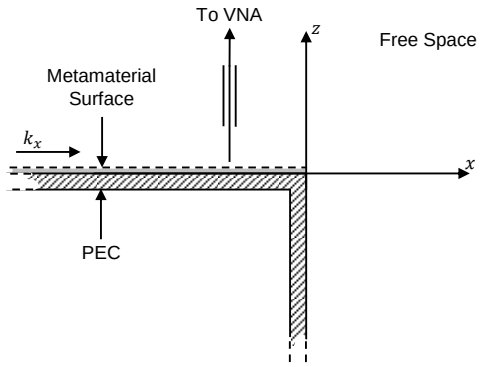

(a) The antenna sheath is orientated perpendicular to the plane of the metasurface.

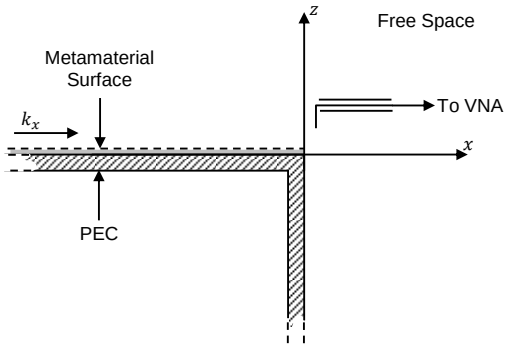

(b) The antenna sheath is orientated in the plane of the metasurface and perpendicular to the termination edge.

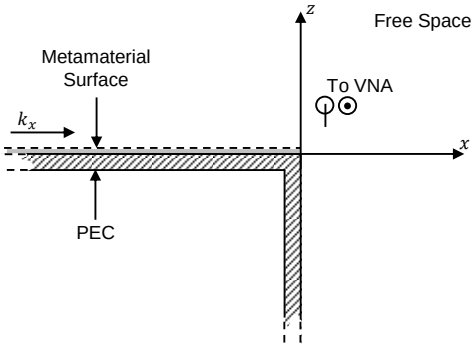

(c) The antenna sheath is orientated in the plane of the metasurface and parallel to the termination edge.

Figure 5.4: Schematic diagrams of the antenna orientation for scattered field measurements. The dipole axis of the antenna is orientated perpendicular to the plane of the metasurface to detect E_z for all orientations.

first is to orientate the sheath of the coaxial line in the plane of the metasurface but perpendicular to the termination edge of the sample, figure 5.4b. Secondly to orientate the sheath of the coaxial line in the plane of the metasurface and parallel to the termination edge of the sample, figure 5.4c. Orientation of the antenna perpendicular to the termination edge measures the E_z-field near the metal boundary below the plane of the metasurface to be near-zero, figure 5.5b $z = -7$ mm $x = 0$. This is consistent with FEM modelled fields, figure 5.6a, and the boundary condition. However the field in the region above the metasurface gives a significantly different distribution to that measured in the original orientation. Since the sheath is electrically conducting and in the near-field of the surface wave it contributes significantly to the detection of the electric field. The sheath is orientated along the x-direction and the antenna is there-

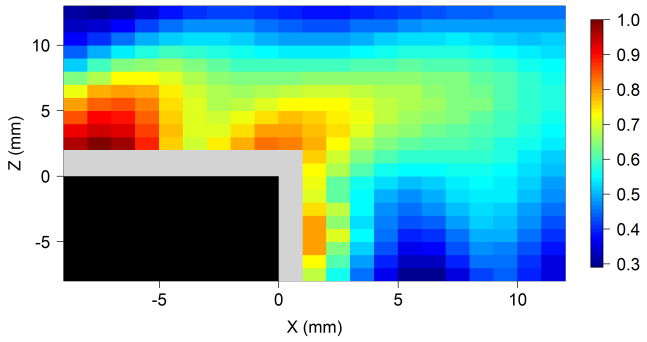

(a) The antenna sheath is orientated perpendicular to the plane of the metasurface, 5.4a.

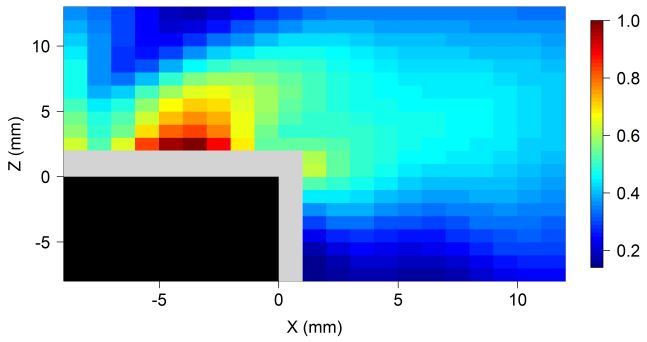

(b) The antenna sheath is orientated in the plane of the metasurface and perpendicular to the termination edge, 5.4b.

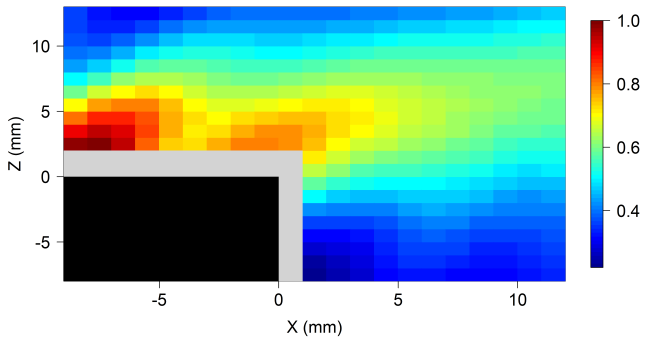

(c) The antenna sheath is orientated in the plane of the metasurface and parallel to the termination edge, 5.4c.

Figure 5.5: Time-averaged E_z-field measured at the termination of a metallic patch array to free space.

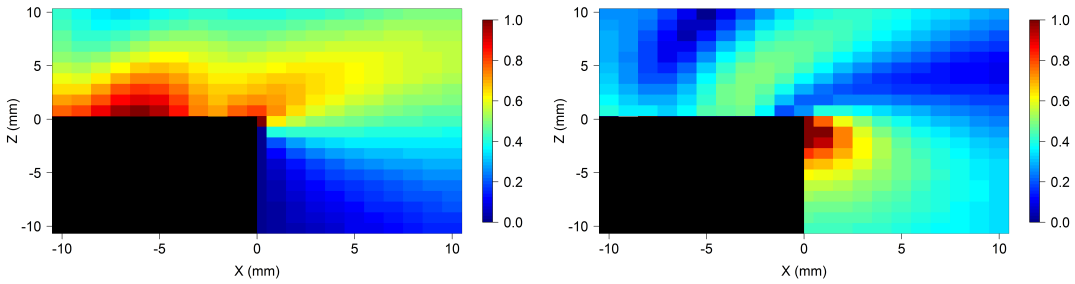

(a) E_z field (b) E_x field

Figure 5.6: Time-averaged electric field components at the termination of the metallic patch array to free space from FEM modelling at 20 GHz.

fore sensitive, not only to E_z but also to E_x which in the standing wave pattern has maxima at the minima position of the E_z field. This is clearly shown in figure 5.5b.

Since the antenna is found to be sensitive to the electric field components in both the direction of the coaxial pin and the orientation of the sheath it is necessary to eliminate the contribution from the sheath in order to measure only the E_z field. An ideal TM surface wave has three field components, E_x, E_z and H_y. Since there is no electric field component in the y-direction the antenna sheath can be orientated along this direction, figure 5.5c, ensuring the antenna is once again sensitive only to the electric field in the direction of the coaxial pin. In this orientation, figure 5.5c, the field measured above the metasurface is comparable to that measured in the original orientation, figure 5.5a whilst the E_z field at the metal boundary, $z < 0$ $x = 0$, is now correctly measured to be near-zero.

A comparison of the experimentally measured field with the two orthogonal electric field components extracted from FEM modelling, shown in figure 5.6, can be performed. It can be seen that the field distribution for the two electric field components are significantly different, firstly at the metasurface interface the orthogonal components have maxima which are approximately 90^o out of phase in space with one another. Secondly the E_x component of the electric field is primarily scattered below the level of the ground plane, figure 5.6b, satisfying the normal E-field boundary condition, whilst the E_z electric field component is primarily forward scattered above the level of the ground plane, figure 5.6a. The final maximum in the interference oscillations above the metasurface, closest to the metasurface termination, is centered on the termination of the metasurface for the E_z field component. However the final maximum for the E_x field component is set back from the interface, at the position of the E_z field interference minima. It can clearly be seen that data taken with the orientation of the antenna sheath perpendicular to the termination edge, figure 5.4b, has many of the features

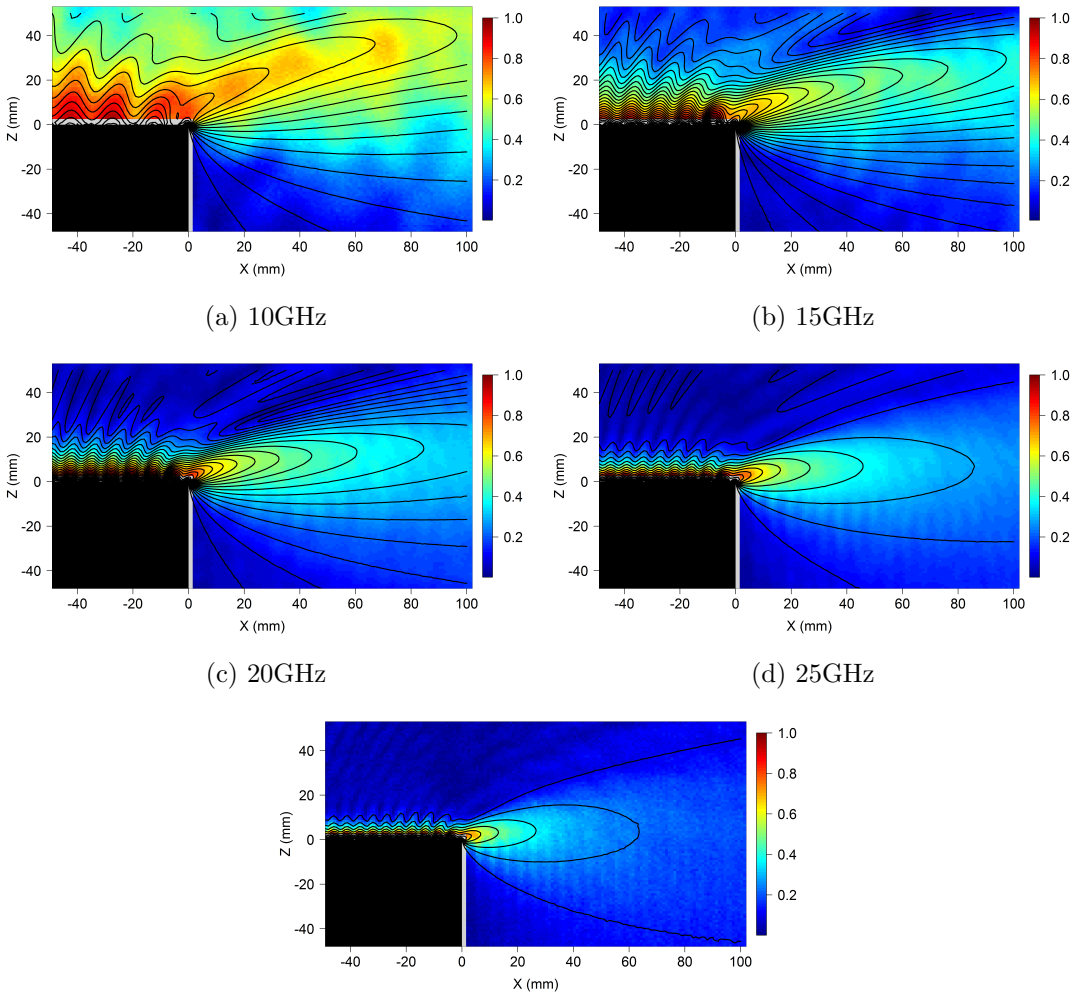

(a) 10GHz

(b) 15GHz

(c) 20GHz

(d) 25GHz

(e) 30GHz

Figure 5.7: Comparison of the scattered E_z field of the termination of the metallic patch array to free space obtained from experiment (colour map) and FEM modelling (lines). Surface waves launched from the left along the surface.

associated with the E_x field profile.

Figure 5.7 shows the experimentally measured scattered radiation associated with the termination of the patch array metasurface to free space with the FEM modelled fields overlaid in contours. Both the freely propagating radiation scattered to free space and the interference oscillations associated with the interference between the incident and reflected surface wave can be seen in these field profiles. The agreement between the experimental data and FEM modelling is good at all frequencies from 10 to 30 GHz. The angle of the lobe of scattered radiation changes rapidly in the near-field of the termination which is most clearly seen at the lower frequencies, figure

5.7a. However it can be seen in the higher frequency measurements that the angle of the lobe tends towards 0^o from the x-axis in the far field. It is predicted from the analytical expressions used to determine the analytical reflection coefficient [80] that in the far-field of the scattering point the angle of the lobe of scattered radiation is small. However the scattered radiation propagates at high angles away from the x-axis for low frequencies. This is due to the near-field of the scattering point which may extend several wavelengths.

5.3 Experimentally Determined Reflection Coefficient

The reflection coefficient of a surface wave incident upon the termination of a metasurface to free space is related to the confinement of the surface wave in the z-direction above the metasurface. This confinement is defined by the k-vector perpendicular to the interface, k_z, which is directly related to the k-vector of the surface wave in the direction of propagation, k_x, since the total k-vector, k_0, is fixed by the frequency of the surface wave and $k_0^2 = k_x^2 + k_z^2$. The dispersions of the surface waves supported by each of the two metasurfaces used in this study are shown in figure 5.2. As the surface wave dispersion diverges from the light line then the decay length of the mode in the z-direction decreases, due to the increasing magnitude of ik_z. This increasing confinement of the mode increases the mismatch of the wavevector in the propagation direction, k_x, of the surface wave when compared to the k-vector of a wave propagating in free space. However the reflection coefficient of the surface wave cannot be purely determined by this mismatch of k_x but also by the field continuity conditions. There is no E-field below the metal ground plane at $z = 0$ of the metasurface, in the region $x < 0, z < 0$, whilst the E-field in the free space region has non-zero E-field within the $x > 0, z < 0$ region, figure 5.3. This field distribution plays an important role since even a mode whose in-plane wavevector is equal to that of the light line in the microwave domain, i.e. a surface wave on a flat perfect conductor, incident on such a termination has a non-zero reflection coefficient due to this field discontinuity.

The amplitude reflection coefficient of the surface wave incident upon the termination of the metallic patch array is shown in figure 5.8 and for the Sievenpiper 'mushroom' array in figure 5.9. In each of these diagrams the reflection coefficient obtained experimentally is shown as open circles whilst the reflection coefficient obtained using the analytical theory of Chu et. al. [80] is shown by the lines. The agreement between the analytic theory and experimentally determined reflection coefficient for the metallic patch array is good throughout the range of the plane wave launcher (PWL), section 3.7. However the agreement between the analytic theory and experiment for the Sievenpiper surface is poor except at low frequencies. The FEM modelling shown

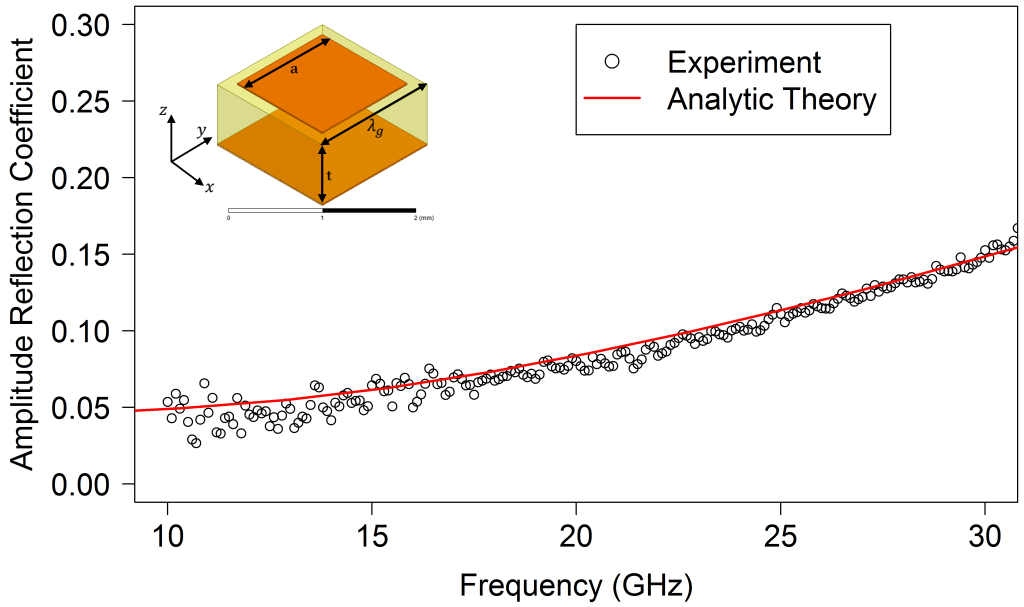

Figure 5.8: Reflection coefficient of the surface wave on a metallic patch array incident on the termination of the metasurface to free space, experiment (circles) and analytic theory (line). Inset: Schematic diagram of the unit cell of the square array of square metallic patches.

by the blue circles in figure 5.9, agrees with the analytic theory at low frequencies but also diverges at higher frequencies while remaining in reasonable agreement with the experiment.

The reflection coefficient for the Sievenpiper 'mushroom' sample tends towards 0.5 as the frequency approaches the surface wave cutoff frequency. Experimentally it is difficult to measure the correct reflection coefficient at these frequencies for two reasons. Firstly the confinement is increasing significantly with frequency making detection of the surface wave more difficult since the near-field coaxial antenna must be very close to the metasurface interface. Secondly the propagation length of the surface wave supported on the Sievenpiper array decreases significantly as the surface wave becomes more confined and more power flows in the dielectric.

The imaginary component of the in-plane wavevector extracted from FEM modelling is plotted as a function of frequency in figure 5.10 and can be seen to increase significantly above 22.5 GHz. This significant increase in the loss of the Sievenpiper 'mushroom' metasurface produces the apparent peak in the measured reflection coefficient of the termination of the metasurface to free space. The reflection coefficient analysis assumes that the loss associated with the propagation of the surface wave on

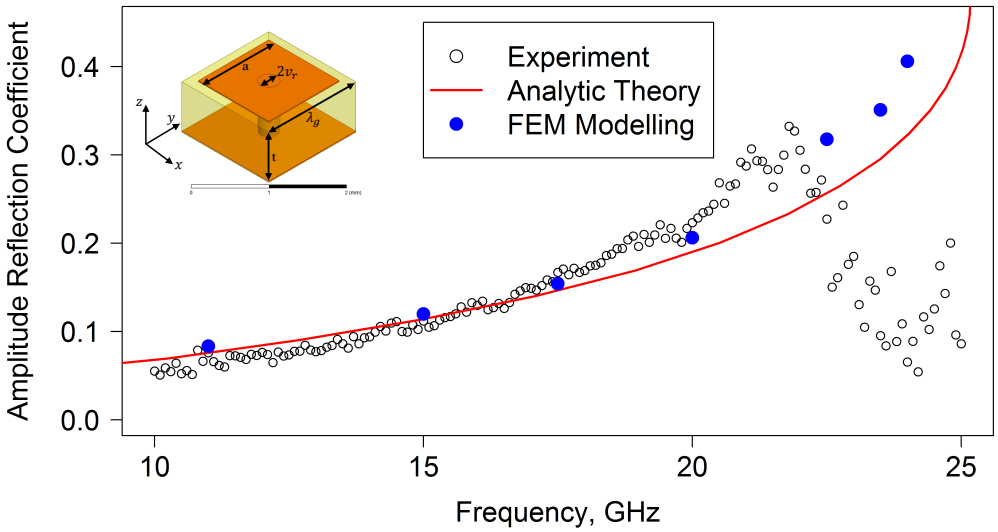

Figure 5.9: Reflection coefficient of the surface wave on a Sievenpiper array incident on the termination of the metasurface surface to free space, experiment (circles) and analytic theory (line). FEM modelling is shown by the crosses. Inset: Schematic diagram of the unit cell of the Sievenpiper 'mushroom' array.

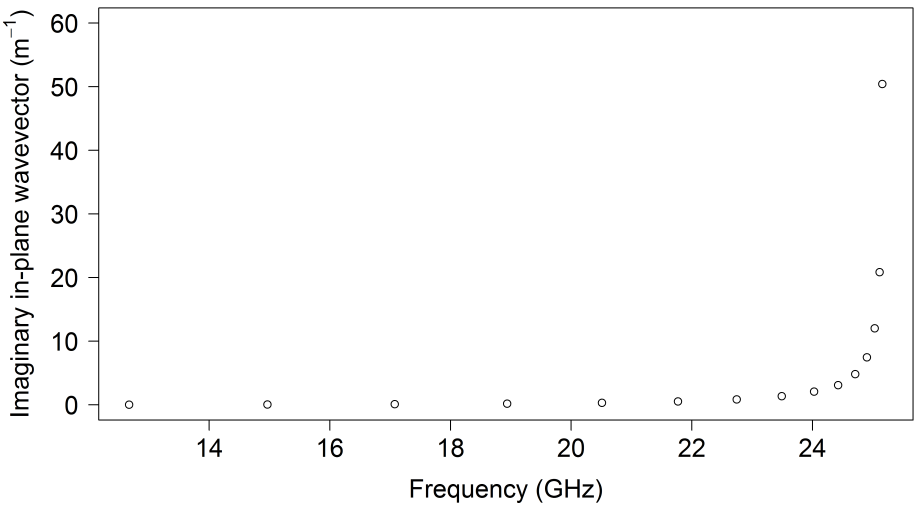

Figure 5.10: The imaginary component of the in-plane wavevector, k_x, of the fundamental TM surface wave supported on the Sievenpiper 'mushroom' metasurface extracted from FEM modelling.

the metasurface structures is negligible, i.e. $\mathrm{Im}(k_x) \approx 0$. Once the in-plane wavevector, $k_x = k' + ik''$, becomes complex the method for determining the reflection coefficient from the FFT is no longer trivial. This is due to the broadening of the peaks in the FFT spectrum such that their ratio is no longer equal to the amplitude reflection coefficient. As such at frequencies where the loss is significant the full measured wave must be fitted with the analytical description of the interference between two lossy waves. A short mathematical description shall be presented to show that this solution is impractical and as such the amplitude reflection coefficient is not accurately determined for frequencies associated with high loss.

The interference of two counter-propagating waves whose amplitudes are decaying along their propagation direction is derived below. The forward propagating wave, Ψ_f, is given by equation 5.1 and the backward propagating wave, Ψ_b, by equation 5.2.

$$\Psi_f = A\exp(-k''x)\exp(i(k'x - \omega t)) \tag{5.1}$$

$$\Psi_b = Ar\exp(k''(x - 2L))\exp(i(k'(L - x) - \omega t)) \tag{5.2}$$

Combining these two waves gives:

$$\Psi_t = \Psi_f + \Psi_b = A\exp(-k''x)\exp(i(k'x - \omega t)) + Ar\exp(k''(x - 2L))\exp(i(k'(L - x) - \omega t)) \tag{5.3}$$

Separating the real and imaginary parts using $\exp(i\theta) = \cos(\theta) + i\sin(\theta)$ gives equations 5.4 and 5.5

$$\mathrm{Re}(\Psi_t) = A\exp(-k''x)\cos(k'x - \omega t) + Ar\exp(k''(x - 2L))\cos(k'(L - x) - \omega t) \tag{5.4}$$

$$\mathrm{Im}(\Psi_t) = A\exp(-k''x)\sin(k'x - \omega t) + Ar\exp(k''(x - 2L))\sin(k'(L - x) - \omega t) \tag{5.5}$$

The square magnitude of the total wavefunction Ψ_t is given by the sum of the squares of the real and imaginary parts:

$$|\Psi_t|^2 = \mathrm{Re}(\Psi_t)^2 + \mathrm{Im}(\Psi_t)^2$$
$$= A^2\exp(-2k''x) + A^2r^2\exp(2k''(x-2L)) +$$
$$2A^2r\exp(-2k''L)\left[\cos(k'x-\omega t)\cos(k'(L-x)-\omega t) + \sin(k'x-\omega t)\sin(k'(L-x)-\omega t)\right] \tag{5.6}$$

A simplification can be made using $\cos(A-B) = \cos(A)\cos(B) + \sin(A)\sin(B)$ to give:

$$|\Psi_t|^2 = A^2\exp(-2k''x) + A^2r^2\exp(2k''(x-2L)) + 2A^2r\exp(-2k''L)\left[\cos(2k'x-k'L)\right] \tag{5.7}$$

Equation 5.7 is the square of the magnitude of the interference pattern associated with two counter-propagating waves whose amplitude is decaying. This is the form of the interference associated with the surface waves incident upon the termination of the Sievenpiper 'mushroom' metasurface. It is clear that fitting this function to the experimentally determined spectrum is infeasible. This difficulty is further increased by the addition of in-plane wavevectors not associated with either the incident or reflected surface wave. These are primarily caused by the interference of the surface wave with the freely propagating wave launched by the PWL.

Therefore, due to the difficulties associated with fitting the function and the inaccuracy associated with the FFT method, it can be seen that the apparent peak in the measured reflection coefficient is not a feature associated with the termination of the Sievenpiper 'mushroom' metasurface. The reflection coefficient, as shown by both the FEM modelling and the analytical theory, continues to increase as the momentum mismatch and the confinement of the mode increases. Correct measurement of the reflection coefficient when the propagation of the surface wave is not lossless is currently not possible using this method.

5.4 Conclusions

The spatial field mapping technique discussed in section 3.6 has been utilised to measure the near-field of a surface wave incident upon the termination of a metasurface to free space. The scattered field from the termination has also been characterised and compared to FEM modelling. Various different antenna orientations have been used to determine the scattered radiation associated with a surface wave incident upon the termination. It has been shown that the sheath of the near-field antenna plays a crucial role in the accurate measurement of a single component of the electric field and must

be orientated along the direction of the magnetic field for characterising TM surface waves. The scattered radiation is strongly forward scattered with the intensity lobe at an angle to the x-axis that depends on the frequency. The surface wave reflection coefficient at the termination of a metasurface to free space for both an array of metallic patches on a dielectric coated ground plane and a Sievenpiper 'mushroom' array has been determined. For the patch array metasurface an analytical model agrees well with the experimental data. However for the Sievenpiper 'mushroom' metasurface the analytical model and experimental data strongly diverge at higher frequencies. This divergence is caused by the surface wave properties of the Sievenpiper 'metasurface', most notably the decrease in the surface wave propagation length at frequencies close to the asymptote of the fundamental TM mode. The reflection coefficient is shown to increase significantly with the confinement of the surface mode which is significantly different for the two metasurfaces considered due to the surface wave dispersions. This increase in the reflection coefficient is caused by both the momentum mismatch of the surface wave compared to the freely propagating modes and the different field distributions of the two modes.

Chapter 6

Surface Wave Reflection and Scattering from Dielectric Overlayers on Metasurfaces

6.1 Introduction

Surface wave absorbing materials are often realised in the form of lossy magnetic or dielectric coatings on top of metal or metasurface substrates. It is therefore desirable to determine the reflection coefficient of a surface wave incident upon such a finite thickness dielectric or magnetic overlayer. In this chapter the reflection coefficient of a surface wave supported on a metasurface and incident upon the boundary of a region of the same metasurface coated with a finite thickness dielectric overlayer, figure 6.1, is experimentally characterised. This reflection coefficient has been determined for a range of dielectric overlayer thicknesses and for both the metallic patch metasurface and the Sievenpiper 'mushroom' metasurface, section 2.2. The addition of a thin, significantly subwavelength, dielectric overlayer onto the metasurfaces markedly alters the dispersion of the fundamental TM surface mode supported on both metasurfaces.

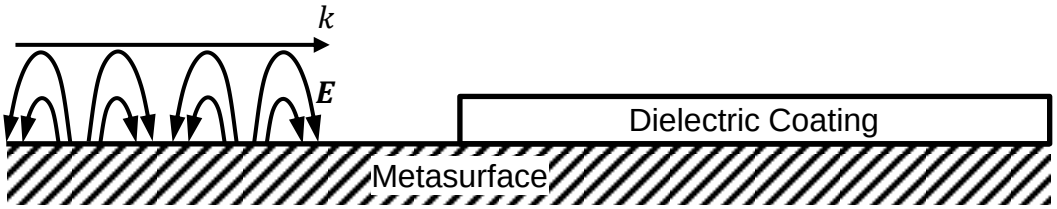

Figure 6.1: Schematic of a surface wave supported on a metasurface incident upon a region of the metasurface coated with a thin dielectric overlayer.

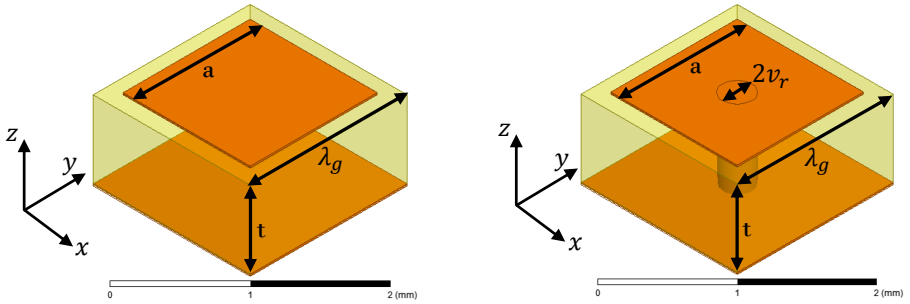

(a) (b)

Figure 6.2: Schematics of the metasurface structures used in this study where the orange represents metal and yellow represents the dielectric; a) square array of square metal patches on a dielectric coated metallic ground plane and b) Sievenpiper 'mushroom' array.

This then leads to reflection of the surface wave as well as scattering to free space radiation at the interface between the coated and uncoated metasurface regions.

The reflection coefficient of the surface wave incident upon these boundaries has been experimentally characterised using the PWL, section 3.7, as a source of microwave surface waves and the reflection coefficient measurement technique described in section 3.8. The behaviour of the reflection coefficient as a function of frequency is determined by both the dispersion of the surface waves supported on the metasurface both with and without a dielectric overlayer. The reflection coefficient of a surface wave incident upon a finite thickness overlayer on the metallic patch metasurface has been fully characterised for a range of dielectric thicknesses and compared to FEM modelling. For the surface wave supported on the Sievenpiper 'mushroom' metasurface the effect of the dielectric overlayer on the surface wave stop band and subsequently on the reflection coefficient has been considered. It will be shown that the surface wave stop band is significantly reduced in frequency by the presence of a dielectric overlayer and as such there exists a frequency band in which transmission of a surface wave is completely forbidden. The radiation scattered to free space is experimentally quantified for this frequency regime.

6.2 Surface Wave Dispersions

The surface wave dispersions for the two metasurfaces studied in this chapter, whose unit cells are shown in figure 6.2, have been discussed in detail in section 2.2. The high field at the metasurface associated with the confined surface wave means that even a thin (i.e. subwavelength) dielectric overlayer perturbs the dispersion of the surface mode

significantly. This can be seen clearly in figure 6.3 since the addition of a thin dielectric overlayer to the metal patch array provides a much larger change to the surface wave dispersion than subsequent thickening of the dielectric overlayer. The dispersion of the surface mode is strongly perturbed by the presence of the dielectric overlayer when the decay length of the surface wave perpendicular to the metasurface is comparable to the dielectric overlayer thickness. It has been shown in section 2.5.2 that the decay length of the surface wave decreases with increasing frequency. However the perturbation of the dispersion of the surface wave is also lessened as the frequency increases due to the increasing strength of the electric field within the core of the metasurface, as discussed in section 2.5.2. The maximum perturbation of the surface wave dispersion therefore occurs at frequencies defined by the convolution of these two effects and therefore where the surface mode is both confined on the order of the dielectric overlayer thickness and the power is mostly flowing in the upper half space. At low frequencies the dispersions converge since the field is less tightly confined to the metasurface and the thickness of the dielectric overlayer is small by comparison to the decay length of the surface wave perpendicular to the interface. Furthermore at high frequencies the perturbation to the surface wave dispersion also lessens since most of the field is now confined within the core of the metasurface.

A similar discussion regarding the surface waves supported on the Sievenpiper 'mushroom' array shows they are also significantly perturbed even for a small overlayer thickness, figure 6.4. This is because the surface wave supported by the Sievenpiper 'mushroom' metasurface has high fields at the interface between the metasurface and the dielectric half-space above. Additionally for all frequencies except those close to the asymptotic frequency of the fundamental TM surface wave the power flow is primarily within the dielectric half-space above the metasurface, see section 2.5.3. These properties of the surface wave mean that for all frequencies within ~ 15 GHz of the asymptotic frequency the dispersion of the surface wave is significantly perturbed by the presence of the dielectric overlayer. This perturbation reduces the frequency of the surface wave stop band, see section 2.5.3, by approximately 7 GHz for a 1.5 mm dielectric overlayer with $\varepsilon_d = 2.6$. It is also noted that due to slight curvature of the Perspex overlayer there is a 50 μm gap between the dielectric and the metasurface, this has been included in the modelling. The reduction of the asymptotic frequency of the fundamental TM surface wave supported on the Sievenpiper metasurface coated with a Perspex overlayer creates a frequency range in which the Sievenpiper metasurface with an overlayer supports no TM surface mode whilst, at the same frequencies, a TM surface mode is supported on the uncovered Sievenpiper metasurface. This frequency range is from approximately 21.5 GHz to 25 GHz and can be seen in figure 6.4. Later in this chapter an investigation of the reflection and scattering to free space of the

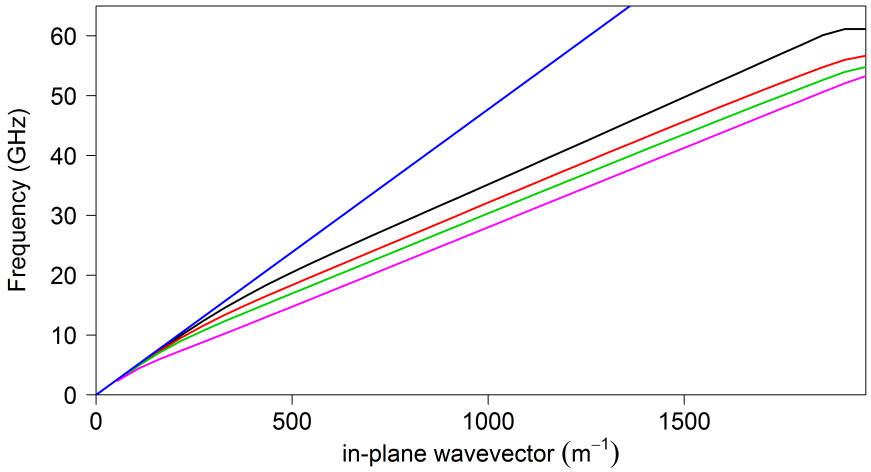

Figure 6.3: Disperision of the TM surface wave supported on the metal patch array (black line) compared with the same metasurface coated with 1 mm (red line), 2 mm (green line) and 10 mm (pink line) thick dielectric overlayers with $\varepsilon_d = 3.15 + 0.09i$. The light line is shown in blue and the x-axis limit indicates the BZ boundary.

surface wave incident upon a dielectric overlayer discontinuity in this frequency regime is provided.

6.3 Experimental Setup

A schematic of the experimental setup used to characterise the surface wave reflection coefficient is shown in figure 6.5. The surface waves are excited using the PWL, discussed in section 3.7, and are normally incident upon a dielectric overlayer coating the metasurface, of height h and permittivity ε_d. The permittivity of the dielectric has been measured using the material characterisation technique presented in section 3.3. It is found to be $\varepsilon_d = 3.15 + 0.09i$. At this interface the surface wave undergoes reflection of amplitude, r, transmission of amplitude, t, and scattering to free space of amplitude, s. The amount of energy contained in each of these channels is dictated by the frequency of the radiation, the geometry of the metasurface and the thickness of the dielectric overlayer. The near-field of the surface wave is measured above the uncoated metasurface using the spatial field mapping technique described in section 3.6. From the measurement of this near-field, the interference of the incident and reflected surface waves is quantified and the reflection coefficient determined, see section 3.8.

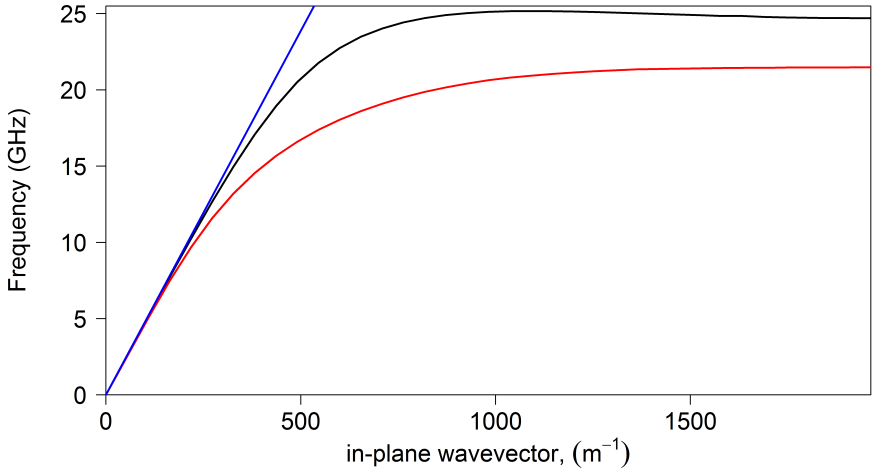

Figure 6.4: Dispersion of the TM surface wave supported on a Sievenpiper 'mushroom' metasurface (black line) compared to the same metasurface coated with a 1.5 mm dielectric overlayer (red line) with $\varepsilon_d = 2.6$. The light line is shown in blue and the x-axis limit indicates the BZ boundary.

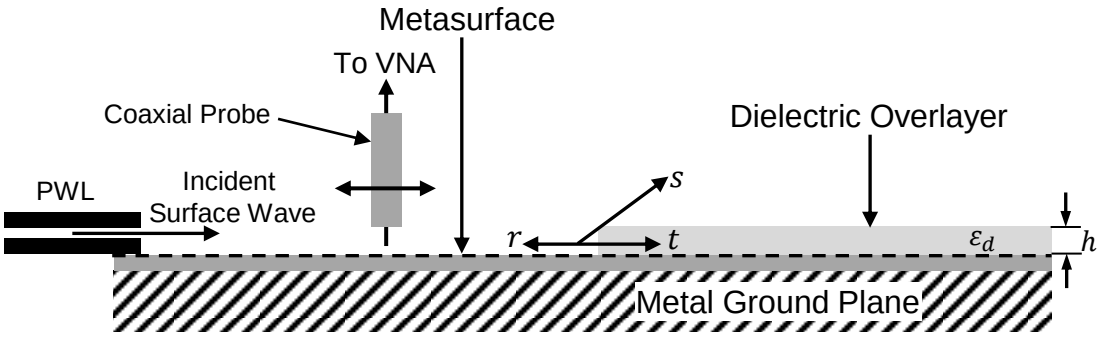

Figure 6.5: Schematic of the experimental setup for characterising the surface wave reflection coefficient for a surface wave, supported on a metasurface, incident upon a finite thickness dielectric overlayer.

6.4 Experimental Results

The reflection coefficient of surface waves propagating on a metasurface that are incident upon a region of the metasurface coated with a dielectric overlayer has been experimentally characterised for both the metal patch array metasurface and the Sievenpiper 'mushroom' metasurface. The reflection coefficient is shown to depend on a variety of different factors, primarily the thickness of the dielectric overlayer and the form of the dispersion of the surface wave supported by the metasurface. The distribution of the

power flow above the metasurface (air) and within the dielectric core of the metasurface structure has also been shown to be a determining factor in the variation of the reflection coefficient of surface waves incident upon the interface between the coated and uncoated metsurface as a function of frequency. Figure 6.6 shows the reflection coefficient as a function of frequency for various thicknesses of dielectric overlayer. Figure 6.7 shows the amplitude of the reflection coefficient of the surface waves incident upon the interface between the coated and uncoated metasurface as a function of the overlayer thickness. This is presented with both the experimental values and the predictions from FEM modelling.

6.4.1 General Form of the Reflection Coefficient as a Function of Frequency

For all dielectric overlayer thicknesses studied the measured reflection coefficient increases with increasing frequency for low frequencies and then begins to decrease with increasing frequency at higher frequencies. The frequency at which the gradient of the reflection coefficient spectrum becomes negative varies with overlayer thickness, as does the maximum reflection coefficient measured. The two parameters that determine the form of this curve are the ratio of the overlayer thickness to the decay length of the surface wave in the direction normal to the surface, and secondly the ratio of the power flow in the core of the patch array and the half space above. The increasing reflection coefficient seen at low frequencies is dictated by the increasing confinement of the surface mode as the frequency increases, see section 2.5.2. This increasing confinement, in the uncoated region, increases the ratio of the thickness of the dielectric overlayer to the decay length of the surface wave normal to the metasurface. This ratio provides an indication of the amount of power flowing above the height of the overlayer and therefore the surface wave reflection coefficient. At higher frequencies

Sample No.	Thickness (mm)	Error (μm)
1	0.825	$\pm$50
2	0.91	$\pm$35
3	1.375	$\pm$50
4	1.73	$\pm$60
5	2.86	$\pm$15
6	4.90	$\pm$25
7	6.85	$\pm$50

Table 6.1: A comparison of the thicknesses of the dielectric overlayers, $\varepsilon_d = 3.15 + 0.09i$, and associated errors used to modify the dispersion of the metal patch array metasurface.

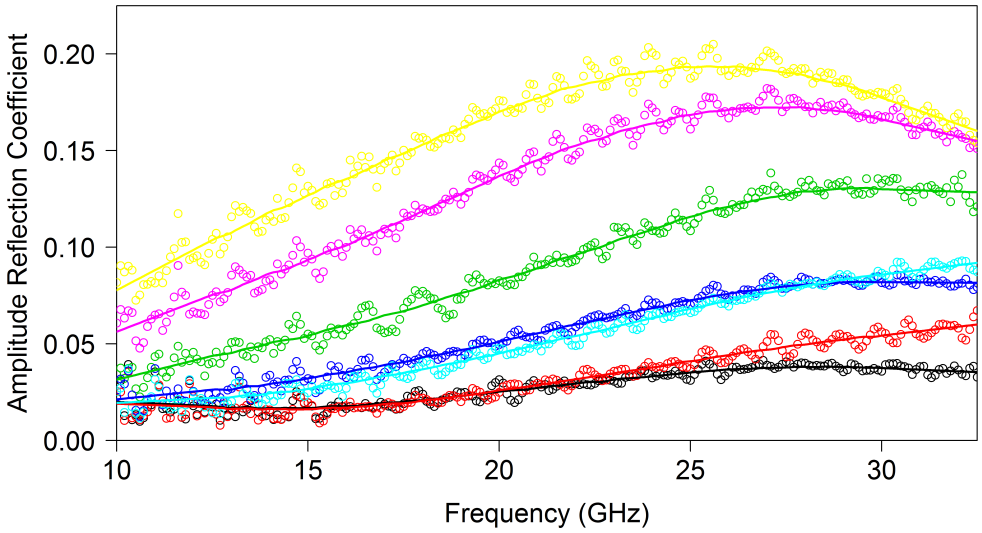

Figure 6.6: Measured amplitude reflection coefficients for surface waves incident upon the interface between the coated and uncoated metal patch array metasurface as a function of frequency for various overlayer thicknesses (points). The running average of the reflection coefficient is shown as the lines. The thicknesses of the dielectric overlayers are as follows: 0.83 mm (black), 0.91 mm (red), 1.38 mm (light blue), 1.73 mm (dark blue), 2.86 mm (green), 4.90 mm (pink) and 6.85 mm (yellow).

the variation in the reflection coefficient as a function of frequency is characterised by the increasing power flow within the dielectric core of the patch array metasurface. As the frequency increases the power flow within the core increases thereby reducing the amount of power contained in the upper half space which interacts more strongly with the dielectric overlayer. The balancing of these two processes determines the variation of the reflection coefficient with frequency.

Figure 6.8 shows the relative power flow in the core of the patch array and the half space above. In the low frequency regime, where the mode is close to the light line, the surface wave is relatively unconfined and the power transmitted in the upper half space is large. However as the confinement of the surface wave increases the fields, and consequently the power flow, in the dielectric core increases. It can be seen that the frequency for which the power flow in the dielectric core is equal to that in the half space above is approximately 35 GHz. The power flowing in the dielectric core of the metasurface begins to increase rapidly at approximately 20 GHz. The relative power flow in above the metasurface (in the air) and within the dielectric core of the metasurface in part determines the variation of the amplitude reflection coefficient with increasing frequency, this will be shown later.

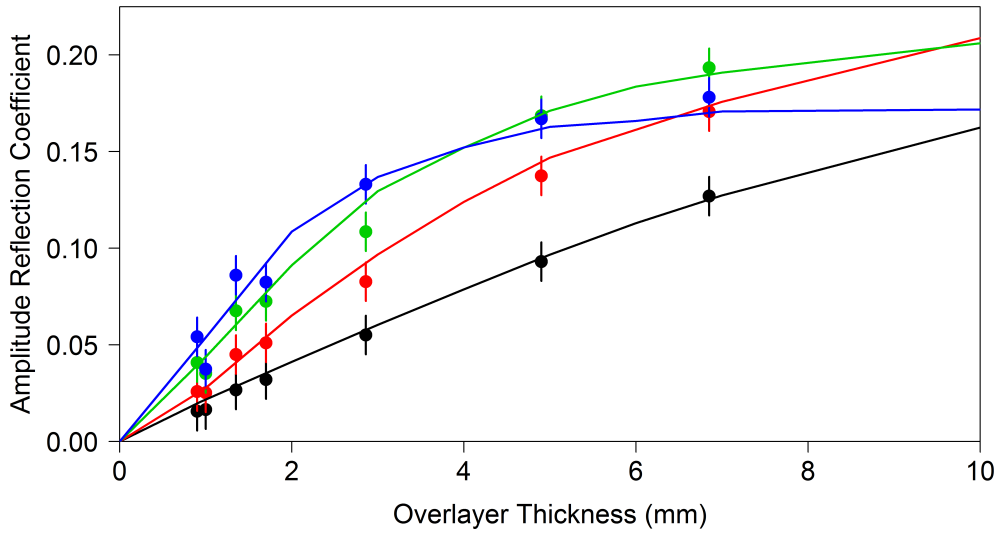

Figure 6.7: Amplitude reflection coefficient as a function of dielectric overlayer thickness for frequencies of 15 GHz (black), 20 GHz (red), 25 GHz (green), and 30 GHz (blue), experiment (points) and FEM model (lines). The error in the measured reflection coefficient is indicated but the error in the overlayer thickness is too small to be seen on this scale, see table 6.1.

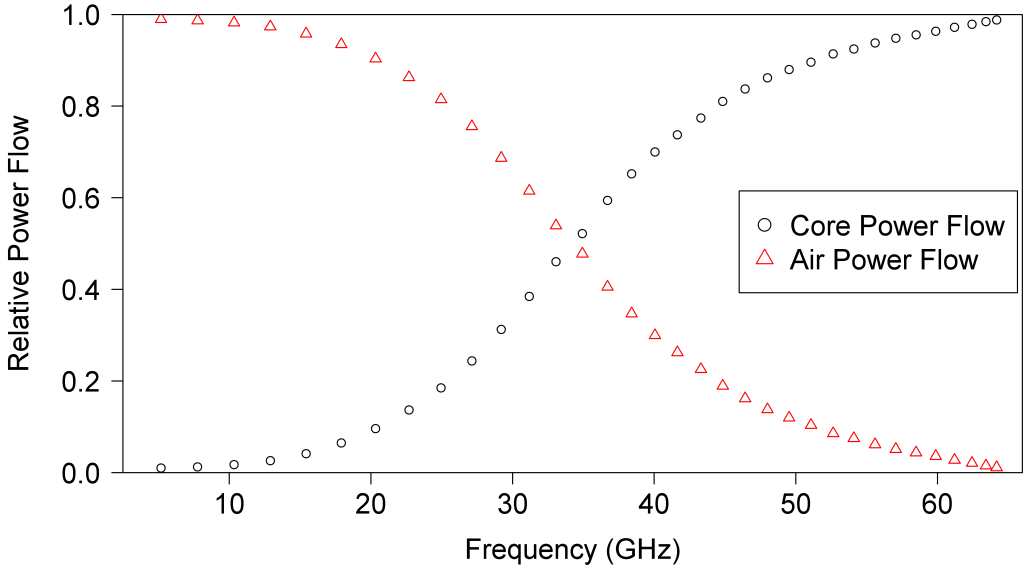

Figure 6.8: Power flow of the fundamental TM surface wave supported on a square array of square metallic patches on a dielectric coated ground plane. The amount of power confined within the dielectric layer is shown in the black circles and the amount of power in the upper half space in red triangles, values taken from FEM modelling.

In figure 6.6 it can be seen that below 20 GHz all of the reflection spectra increase as a function of frequency. This is partially due to the decreasing decay length of the surface wave normal to the metasurface which increases the effective thickness of the overlayer. The other contribution is from the momentum mismatch, Δk, between the dispersion of the surface wave supported on the coated and uncoated metasurface which is also increasing with increasing frequency. Whilst above 25 GHz, the dependence of the reflection coefficient on frequency for the larger thickness overlayers is beginning to be affected by the increasing power flow within the dielectric core of the metasurface. At these frequencies the Δk between the dispersion of the surface wave supported on the coated and uncoated metasurface is still increasing, figure 6.3, but the field of the mode is mostly confined within the dielectric core of the metasurface. This increase in confinement reduces the amplitude reflection coefficient due to the increase in modal overlap of the fields associated with the surface wave supported on the coated and uncoated metasurface.

To confirm this modal overlap understanding, a quantitative comparison of the time-averaged electric field profile for the uncoated and coated patch metasurface has been performed. The frequencies of the field plotted for the coated and uncoated patches are only approximately equal to each other due to the FEM dispersion modelling which fixes the in-plane wavevector, k_x. The time-averaged electric field profiles, extracted from FEM modelling, for three of these frequencies (~ 5.13 GHz, ~ 20.25 GHz and ~ 49.37 GHz) are shown in figure 6.9, where the surface wave is propagating along the x-axis.

The modal overlap of these fields can be quantified by calculating the sum, over an array of points in the yz-plane, of the magnitude of the difference between the time-averaged field for the coated and uncoated metasurface. This value is then subtracted from 1 to give an overlap coefficient. This analysis gives an overlap coefficient between 0 and 1 where 1 indicates perfect field matching and 0 indicates no field overlap. Figure 6.10 shows the variation of the overlap coefficient with frequency for the electric field of the surface wave supported on the uncoated and coated patch array metasurface. It can be seen that the highest modal overlap occurs at the lowest frequency, where both modes are very close the light line and the field confinement is low. As the confinement increases the modal overlap decreases, since the increase in confinement occurs at different rates for the two surface waves. However at the higher frequencies, where the majority of the field is confined within the dielectric core of the metasurface, the modal overlap is greater than that at 25 GHz. This increase in the modal overlap at higher frequencies is due to the increasing field strength within the dielectric core of the metasurface in both the coated and uncoated case.

The reduction of the reflection coefficient amplitude at higher frequencies due to

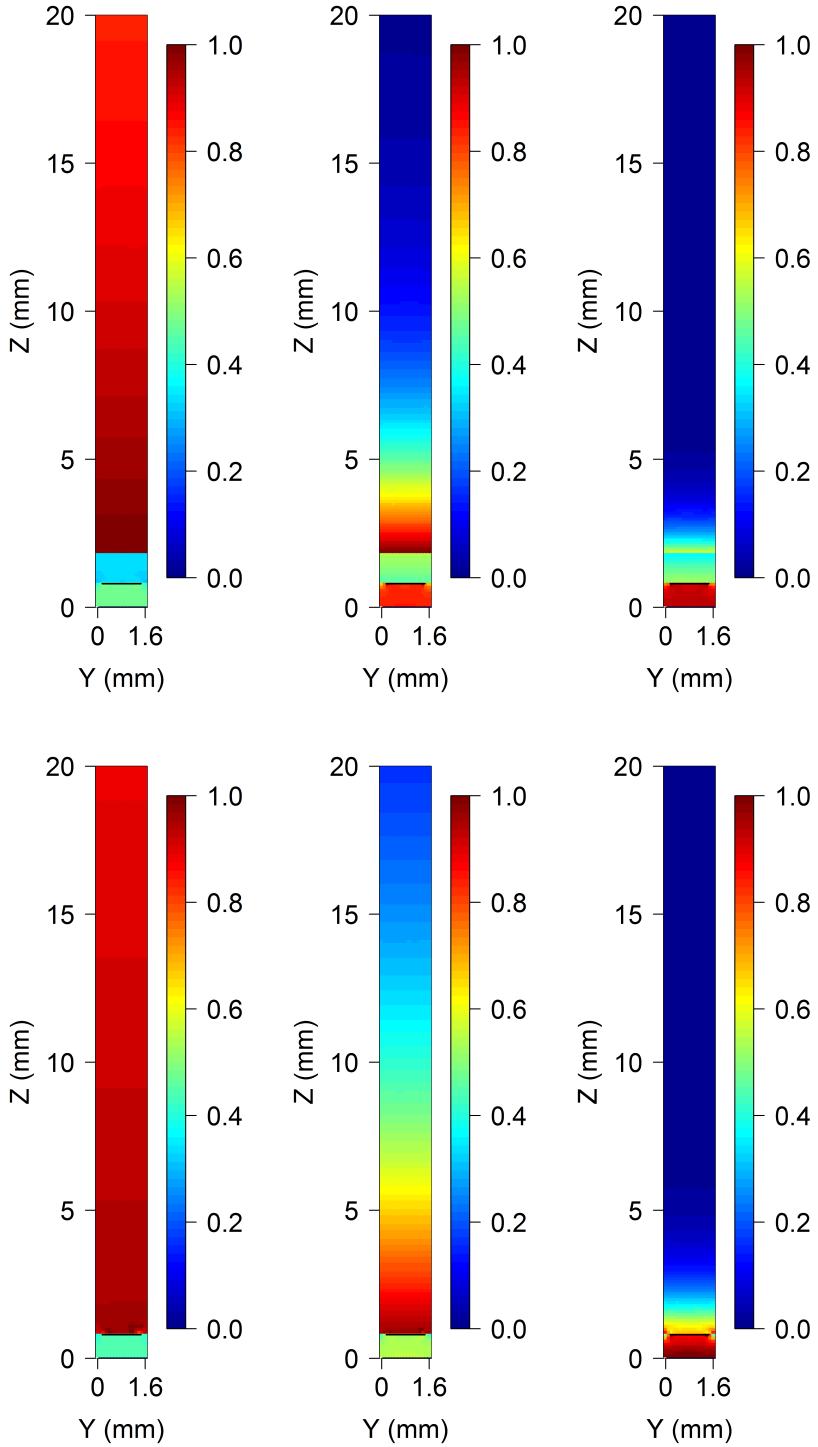

Figure 6.9: Time-averaged electric field profiles for the surface wave supported on the patch array metasurface at ∼5.13 GHz (left), ∼20.25 GHz (middle) and ∼49.37 GHz (right). The top row shows the field for the patch metasurface with a 1 mm thick dielectric coating ($\varepsilon_d = 3.16$) and the bottom row for the uncoated metasurface. Here red indicates high field, blue indicates low field and black indicates metal.

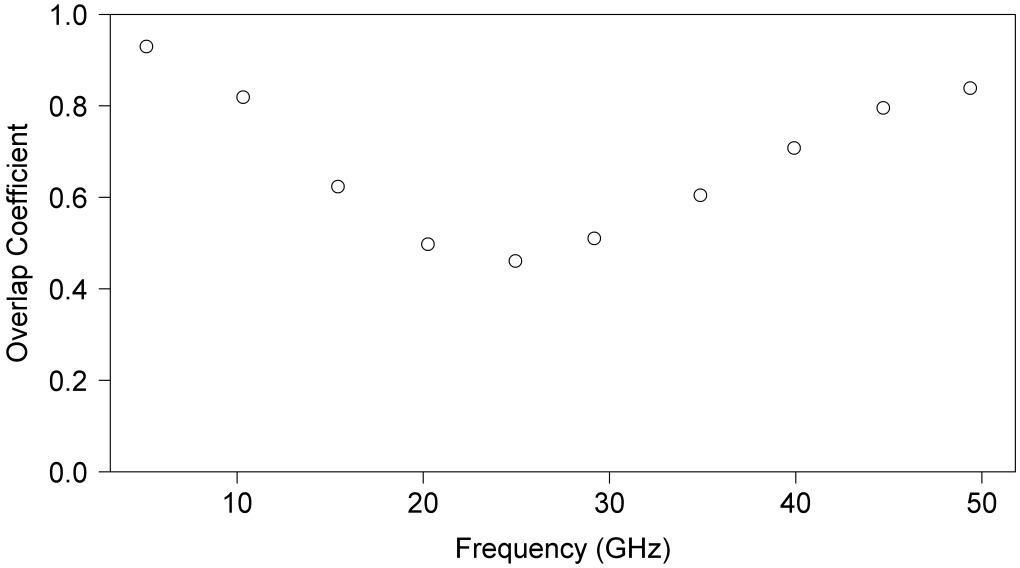

Figure 6.10: Plot of the overlap coefficient between the electric field of the TM surface mode supported on an uncoated patch array metasurface and the same metasurface coated with a 1 mm thick dielectric overlayer ($\varepsilon_{\mathrm{d}} = 3.15$).

increased confinement can also be understood by considering the reflection coefficient of the interface between the uncovered patch array and the patch array covered by an infinitely thick dielectric overlayer. Obtaining the reflection coefficient experimentally for such a system is difficult unless the dielectric is lossy due to the reflections from the termination of the sample, discussed in section 3.8.2.2. This is different than the thin overlayer case since, for thin overlayers, a taper is used to reduce the reflection from the sample termination. This tapering method becomes increasingly difficult for increasing overlayer thickness since the required taper length increases.

The modelled reflection coefficient for a surface wave incident on the patch metasurface coated with an infinite thickness dielectric decreases with increasing frequency due to the increasing power flow within the dielectric of the metasurface. This can be understood by considering the case where the surface wave is entirely confined within the dielectric of the metasurface, although this condition is never physically reached. In this case the addition of an overlayer would have no effect on the surface wave and the reflection coefficient would be zero. Therefore as the power flowing within the dielectric core of the metasurface increases there is a smaller perturbation of the surface wave caused by the dielectric overlayer and the reflection coefficient decreases.

In figure 6.7 the reflection coefficient of surface waves incident upon the interface between the coated and uncoated regions is plotted as a function of overlayer thickness.

With increasing overlayer thickness the surface wave reflection coefficient at the higher frequencies reaches its maximum value (asymptote) at smaller overlayer thicknesses than the lower frequencies. The reflection coefficient of the surface wave incident upon a region with a finite thickness coating will be the nearly the same as that for an infinite thickness coating if the surface wave field can be considered to be negligible above the coating. This condition is reached at thinner overlayer thicknesses for higher frequencies than for lower frequencies since the decay length away from the surface is shorter at higher frequencies. It can be seen that the reflection coefficient for surface waves at 30 GHz has reached its maximum value at overlayer thicknesses of less than 10 mm. The maximum value of this reflection is defined by the infinite thickness case, which decreases with increasing frequency. In contrast the reflection coefficient for 15 GHz surface waves is still increasing, in a near-linear fashion, throughout this range of overlayer thicknesses.

6.5 Perspex Overlayer on a Sievenpiper 'Mushroom' Metasurface

The dispersion of the Sievenpiper 'mushroom' structure presents a significantly different variation of the reflection coefficient with frequency than that of the metallic patch array. The Sievenpiper 'mushroom' structure has a frequency band where no surface wave is supported above the asymptotic frequency of the fundamental TM mode. This asymptote is significantly reduced in frequency by the introduction of a thin dielectric overlayer and with it, the surface wave stop band. This leads to a frequency regime where, for a surface wave incident upon the interface between the uncoated and coated metasurface, there is no possible transmission as a surface wave into the coated region. Therefore almost all of the surface wave is reflected. However the reflection coefficient at these frequencies is not necessarily equal to 1 since there still exists the scattering to free space radiation.

6.5.1 Scattered Fields

The scattered radiation associated with the surface waves incident upon the interface between the coated and uncoated Sievenpiper 'mushroom' metasurface has been experimentally characterised using the techniques presented in section 3.6. The radiation scattered to free space associated with the interface is clearly seen in figure 6.11. Its direction is primarily forward at an angle above the dielectric overlayer at the lower frequencies. The decay length of the surface wave incident upon the overlayer and the standing wave associated with the reflected surface wave can clearly be seen on

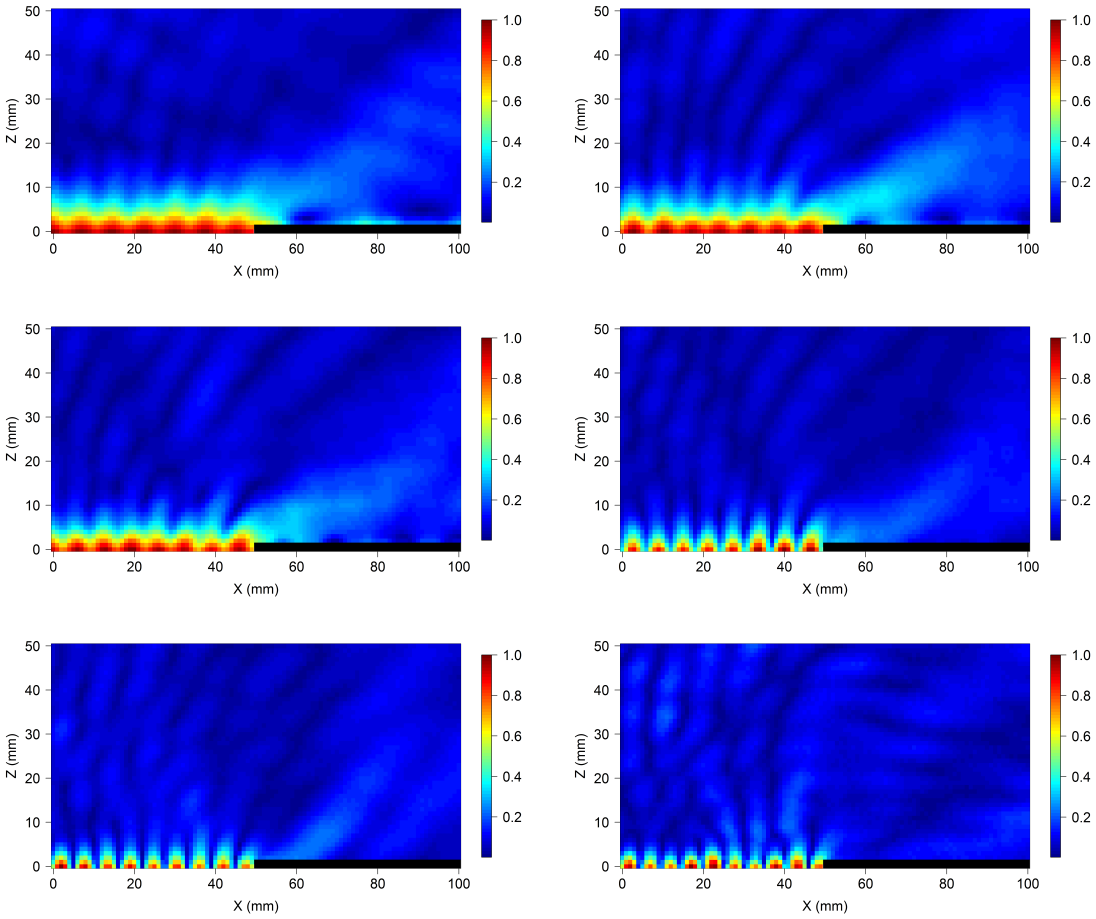

Figure 6.11: Experimentally characterised E_z-field associated with a surface wave supported on the Sievenpiper 'mushroom' metasurface incident upon a region of the metasurface coated with 1.5 mm thick Perspex overlayer (black rectangle) at 18 GHz (top left), 19 GHz (top right), 20 GHz (middle left), 21 GHz (middle right), 22 GHz (bottom left) and 23 GHz (bottom right). The surface wave is incident from the left and red indicates high field and blue low field.

the uncovered Sievenpiper 'mushroom' metasurface. As the frequency of the surface wave incident upon the overlayer increases it can clearly be seen that the decay length of the surface wave on the uncovered metasurface decreases significantly, such that at approximately 23 GHz the decay length is comparable to the thickness of the dielectric overlayer. The standing wave associated with the surface wave reflection coefficient can also be seen to increase in strength with increasing frequency, with the greatest change occurring between 20 and 21 GHz. This increase in the strength of the standing wave coincides with the rapid increase in the reflection coefficient also seen in this frequency range, see figure 6.12.

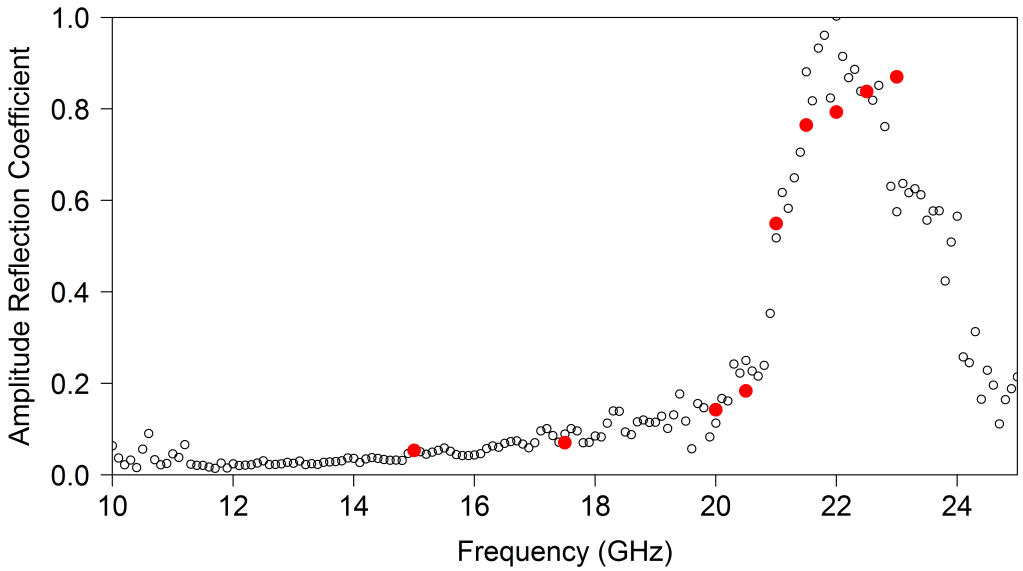

Figure 6.12: Amplitude reflection coefficient as a function of frequency for a surface wave incident on the boundary between an uncoated 'mushroom' structure to a coated 'mushroom' structure.

6.5.2 Experimentally Determined Reflection Coefficient

The reflection coefficient is of most interest in the frequency regime where a surface wave is supported on the uncoated but not on the coated metasurface. At these frequencies the surface wave supported on the uncovered Sievenpiper 'mushroom' metasurface has a decay length into the dielectric half-space above the metasurface which is comparable to the dielectric overlayer thickness. In this case the amplitude of the scattering of the surface mode to free space is relatively small, and since no transmission mechanism is present the reflection coefficient must be close to 1. The amplitude reflection coefficient increases significantly from near-zero, where the dispersions of the surface waves supported on the Sievenpiper 'mushroom' metasurface with and without and overlayer are nearly identical, to greater than 0.8 over a frequency range of approximately 5 GHz. This sharp feature is directly related to the shape of the dispersion of the surface wave which also diverges quickly from the light line at these frequencies, figure 6.4.

In the frequency regime where there is no transmission mechanism, above $\sim$21.5 GHz, scattering is the only channel, other than in the reflected surface wave, by which energy propagates away from the interface. The primary scatter direction for the radiation is forward in the half-space above the dielectric overlayer when the decay length of the surface wave is much larger than the overlayer thickness. However as the decay length

decreases the magnitude of the scattering into the half-space above is now significantly reduced due to the limited power flowing above the height of the dielectric and the primary scatter direction is in the negative x-direction. Once again, as in chapter 5, the significant decrease in the propagation length of the surface wave supported on the Sievenpiper 'mushroom' metasurface leads to an incorrectly determined reflection coefficient above 22.5 GHz. This introduces an apparent peak in the reflection coefficient as in the previous measurement. The near linear reduction with increasing frequency of the surface wave reflection coefficient at these frequencies is very similar to that shown by the reflection coefficient of surface waves incident upon the termination of the Sievenpiper metasurface to free space, seen in Chapter 5. The reflection coefficient predicted from FEM modelling remains large at these frequencies.

6.6 Conclusion

In this chapter the reflection coefficient of surface waves supported on a metasurface incident upon a dielectric overlayer has been experimentally characterised for the metallic patch array and Sievenpiper 'mushroom' metasurfaces. It has been shown that the addition of a thin, significantly subwavelength, dielectric overlayer onto the metal patch array metasurface perturbs the surface wave dispersion. The reflection coefficient of the surface waves supported on the metallic patch array metasurface incident upon the dielectric coated metasurface has been shown to vary significantly with both the frequency of the radiation and the thickness of the dielectric overlayer. The variation of the reflection coefficient with frequency is primarily dictated by the confinement of the surface wave by comparison to the overlayer thickness and the power flow within the metasurface structure. This leads to two different regions within the reflection coefficient spectrum where initially the reflection coefficient is increasing with frequency due to the increasing confinement of the surface wave whilst at higher frequencies the reflection coefficient decreases due to the increasing relative power flow within the metasurface structure. It has been shown that the reflection coefficient, measured at a single frequency, as a function of overlayer thickness has an asymptotic limit. This maximum reflection coefficient value is larger for lower frequencies due to the reduced power flow within the metasurface by comparison to higher frequencies. The reflection coefficient of a surface wave incident upon a coated Sievenpiper 'mushroom' metasurface is significantly different since the surface wave stop band of the Sievenpiper 'mushroom' metasurface leads to a near complete reflection of the surface waves when their transmission is forbidden. The scattered radiation associated with the reflection of the surface waves supported on the Sievenpiper 'mushroom' structure has also been mapped. The reduction of the reflection coefficient for surface waves incident on dielectric overlayer coated

metasurfaces has applications in the design of efficient surface wave absorbing materials for the reduction of radar cross section. This technique for determining the reflection coefficient of such overlayers may also be useful in characterising the performance of such absorbers.

Chapter 7

Surface Wave Reflection from an Impedance Discontinuity

7.1 Introduction

In this chapter the reflection coefficient and associated scattering to free space of a surface wave incident upon an impedance discontinuity in a metasurface will be fully experimentally characterised. The impedance discontinuity in the metasurface is engineered by a change of the unit cell of the metasurface such that the surface waves supported by the two regions have different dispersion relations and field profiles. The reflection coefficient and associated scattering will be considered in frequency regimes where the surface wave dispersions are similar and also in frequency regimes where they are distinctly different. The experimentally measured reflection coefficient is compared to both FEM modelling results and analytically obtained reflection coefficients using the impedance approximation. The reflection coefficient of the surface wave obtained analytically, using the impedance approximation, is shown to not match the experimentally measured reflection coefficient. A discussion of the validity of such an approximation is presented.

7.2 Surface Wave Dispersions

The metasurfaces that have been used in this experiment are derived from the metal patch array and the Sievenpiper 'mushroom' array metasurfaces used within the previous parts of this study, Chapters 5 and 6. One metasurface is an array of metal strips on a dielectric coated ground plane, the surface wave supported on this metasurface is similar to that supported on the metal patch array metasurface. The second metasurface is a square array of metal pins connected to a metallic ground plane and

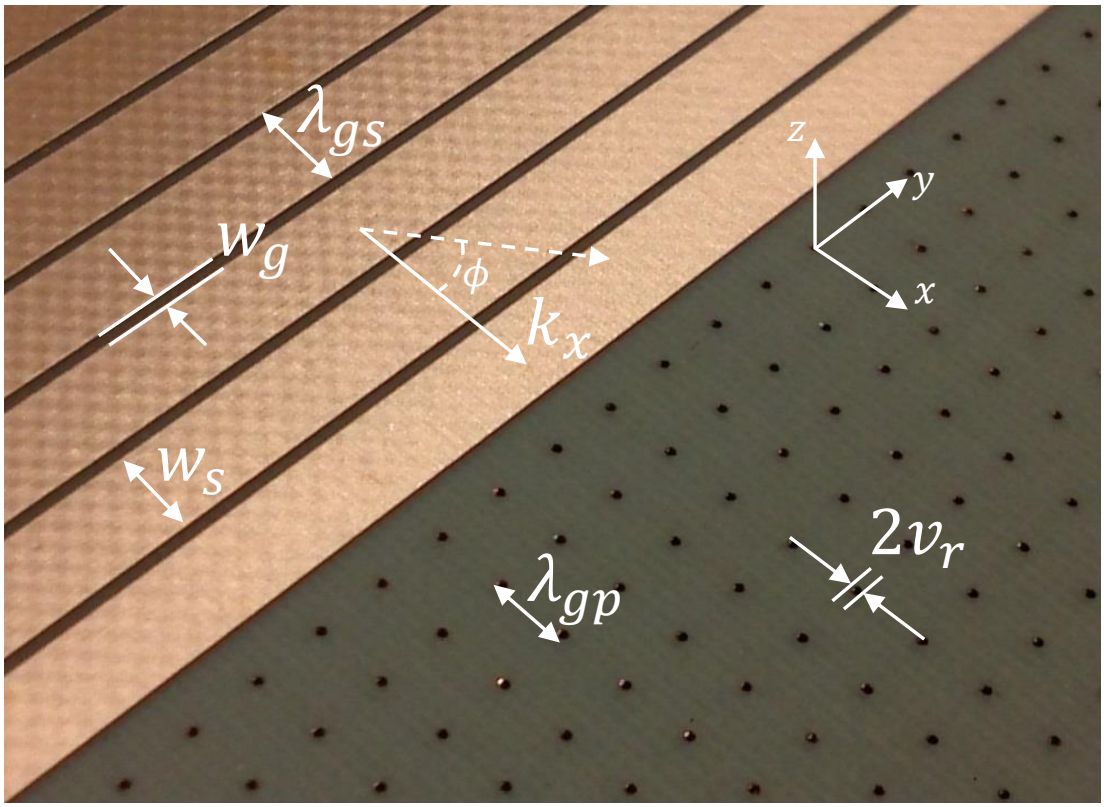

Figure 7.1: Photograph of the discontinuity in the metasurface structure showing the metal slit array and the metal post array with the incident surface wave momentum indicated by k_x. Here $\lambda_{gs} = 3$ mm, $W_s = 2.7$ mm, $W_g = 0.3$ mm, $\lambda_{gp} = 2$ mm, $v_r = 150$ μm and the thickness of the dielectric core of the metamaterial is 1.6 mm.

surrounded by a dielectric; this metasurface can be considered the same as that formed by removing the metallic patch from the Sievenpiper 'mushroom' array. The interface, i.e. the impedance discontinuity, between the two metasurfaces used within this chapter is shown in figure 7.1, where $\lambda_{gs} = 3$ mm, $W_s = 2.7$ mm and $W_g = 0.3$ mm for the strip array and $\lambda_{gp} = 2$ mm and $v_r = 150$ μm for the post array and the thickness of the dielectric core of the metamaterial is 1.6 mm.

The surface wave supported on the metal strips metasurface is effectively a guided wave in the dielectric similar to the patch array with the strips acting as a frequency selective surface as discussed in section 2.2. The dispersion of the fundamental TM surface wave supported on the metal strips metasurface is shown in figure 7.2a. However, unlike the metal patch array, the surface wave dispersion on the strip array is highly-dependent on the azimuthal angle, ϕ, of the incident wavevector with respect to the x-axis. This is due to the absence of the square symmetry present in the metal patch array. When the surface wave is propagating along the strips the electric field is

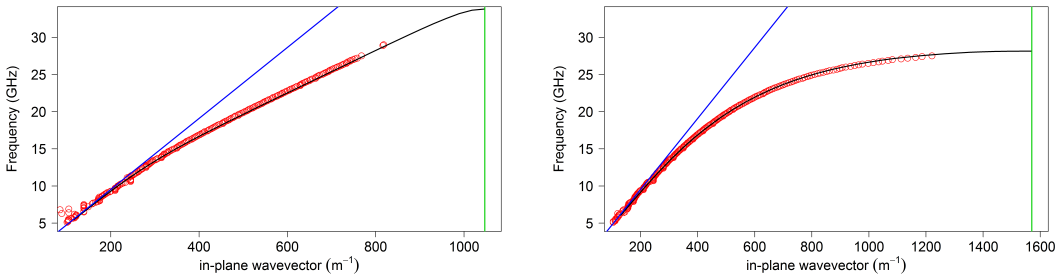

(a) (b)

Figure 7.2: Dispersion diagrams for a) the fundamental TM surface wave supported on the metal strip array from FEM modelling (black line) and experiment (red circles) and b) the fundamental TM surface wave supported on the metal post array from FEM modelling (black line) and experiment (red circles). The light line and BZ boundary is shown in blue and green respectively.

unable to penetrate into the dielectric core of the metasurface since the metallic strip acts as a polarising filter [137–139]. In this case the dispersion of the surface wave is essentially that of a grazing photon. In contrast, for the surface wave propagating along the axis perpendicular to the direction of the strips the surface wave dispersion is largely determined by the Brillioun Zone (BZ) boundary at which the group velocity of the surface wave must fall to zero, section 2.5.1. The metal strips array has been used in this study rather than the metal patch array due to FEM modelling constraints.

The dispersion of the surface wave supported on the square array of metal posts, figure 7.2b, is similar to that supported on the Sievenpiper 'mushroom' metasurface. The patch layer in the Sievenpiper 'mushroom' metasurface acted as an effective high index layer, see section 2.5.2.1, and its removal increases the asymptotic frequency of the fundamental TM surface wave supported by the structure. Once again the metal posts, in the post array metasurface, act as polarisable elements dispersed within the dielectric of the metasurface core. The TM surface wave is supported below the the resonance of these polarisable elements, defined primarily by their length, and above the resonance there exists a surface wave stop band within which neither TM nor TE surface waves are supported. By comparison to the dispersion of the surface wave supported by the Sievenpiper 'mushroom' metasurface discussed earlier, the dispersion of the fundamental TM surface wave on the metal post metasurface diverges from the light line at a lower frequency and the frequency of the lower edge of the surface wave stop band is increased, see figure 7.3. This leads to a dispersion whose rate of change of the gradient with respect to frequency is generally much slower than that of the original Sievenpiper 'mushroom' metasurface. The surface wave dispersions for both

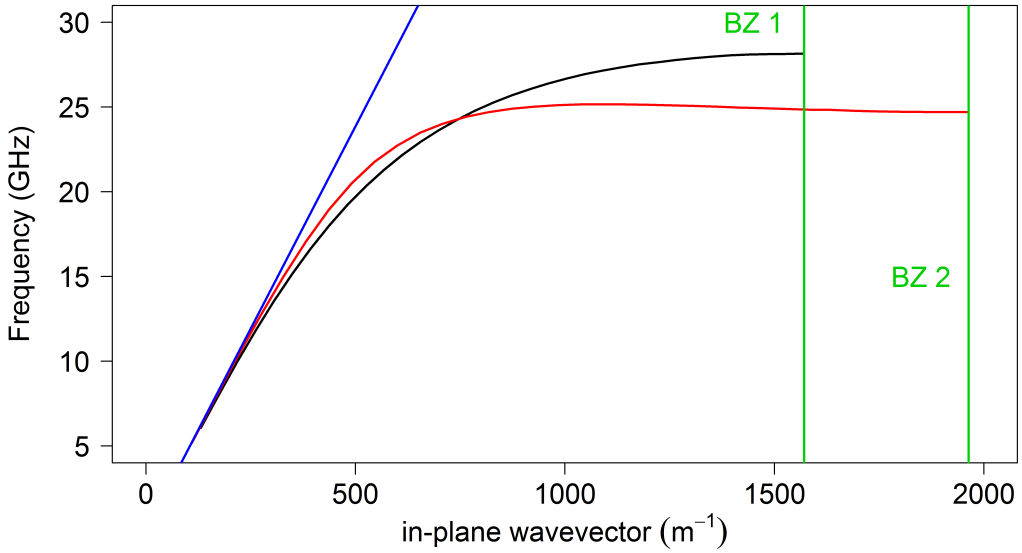

Figure 7.3: Comparison of the dispersion of the TM surface waves supported on the Sievepiper 'mushroom' structure (red line), discussed in section 2.5.3, and the metal post array (black line) extracted from FEM modelling. The light line is shown in blue and the BZ boundaries associated with each of the metasurfaces is shown in green, BZ 1 for the post array metasurface and BZ 2 for the 'mushroom' metasurface.

the strip array and the post array metasurfaces is shown in figure 7.2.

The relative power flow, extracted from FEM modelling, within the dielectric core of the two metasurfaces as a function of frequency is shown in figure 7.4. It can be seen that the relative power flow within the dielectric core of the strip array metasurface (black circles) is greater than that in the metal post array core (green crosses) at all frequencies, although they are very similar at low frequencies where the surface modes are almost on the light line for both surfaces. The relative power flow within the dielectric core of the metal strip array (black circles) quickly increases above 10 GHz and is greater than that flowing above the metasurface at $\sim$15 GHz. Conversely for the metal post array the relative power flow within the metasurface dielectric core (green crosses) is never greater than 30%. This shows that the two modes supported on these metasurfaces have significantly different field distributions with the metal strip array having significantly larger relative power flow within the metasurface than the surface mode at the same frequency for the metal post array.

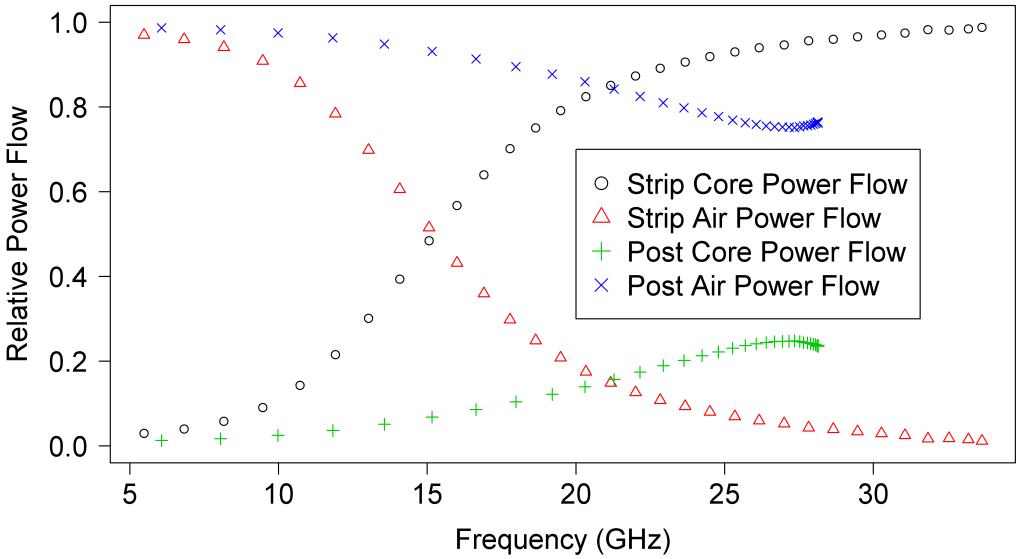

Figure 7.4: Comparison of the relative power flow above and below the metasurface interface for the metal strip array metasurface (below - black circles, above - red triangles) and the metal post array metasurface (below - green cross, above - blue x) extracted from FEM modelling.

7.2.1 Impedance Matched Condition

The surface impedance approximation, often used to describe the behaviour of surface waves on metasurface structures and discussed in section 2.4, is derived from the dispersions of the surface waves, equation 7.1 (reproduced from section 2.4). In the limit that the surface impedance is assumed to be purely reactive (no Joule heating), i.e. the surface waves propagation length is infinite, the surface impedance of the metasurfaces are identical at the crossing points of the dispersion. At these 'impedance matched' crossing points the surface impedance description predicts that a surface wave incident upon the interface between the two metasurfaces will undergo no reflection or scattering to free space. Naively one may expect this however, as discussed in section 7.3.1, it will be shown that this is not the case and that the impedance description is inadequate for the metasurfaces studied here. It can be seen from figure 7.5 that the dispersion of the surface waves supported on the two metasurface used in this study have two such 'impedance matched' crossing points, one at ~ 13.45 GHz (A) and another at ~ 20.12 GHz (B).

$$k_x = \frac{\omega}{c}\sqrt{1+\chi_s^2} \tag{7.1}$$

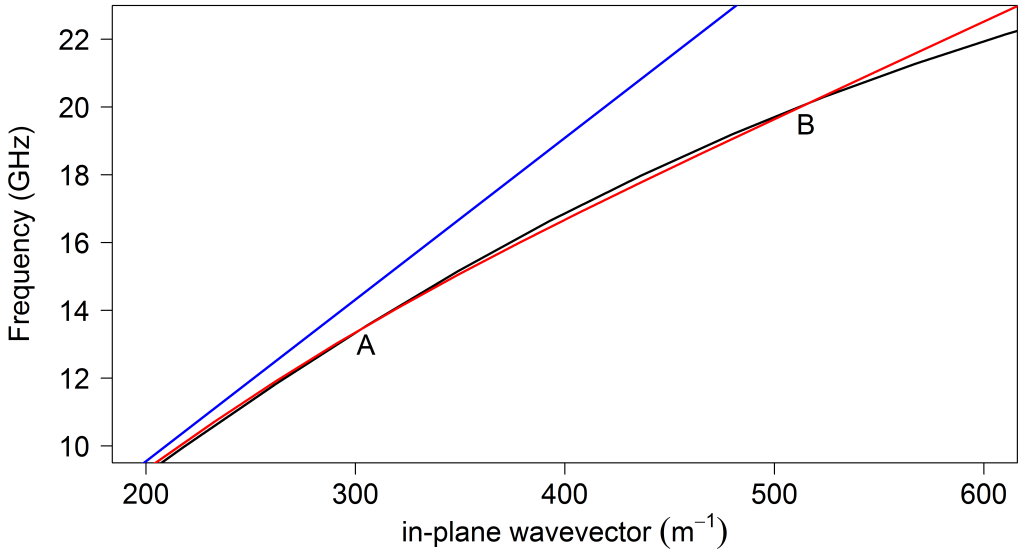

Figure 7.5: Predicted (FEM) dispersion diagram for the fundamental TM surface wave supported on the metal strip array, red, and the fundamental TM surface wave supported on the metal post array, black. The crossings of the mode dispersions, and hence the surface impedance matched condition, are shown to occur at approximately 13.45 GHz (A) and 20.12 GHz (B).

Where k_x is the in-plane wavevector of the surface wave, ω is the angular frequency of the surface wave, c is the speed of light and χ_s is the surface reactance in the impedance approximation.

7.3 Reflection of Surface Waves

The reflection coefficient of the surface waves incident upon the discontinuity in the metasurface has been measured using the technique described in section 3.8. It will be shown that the traditional surface impedance description used to determine the reflection coefficient is insufficient for surface waves supported on metasurfaces. Rather than the surface impedances it is shown that the reflection coefficient is dictated largely by the modal overlap of the fields at any given frequency. For both of the surfaces investigated in this study the confinement of the mode, determined by the magnitude of the normal wavevector, k_z, is increasing as the frequency increases. This confinement is different for each of the metasurfaces and is derived from the dispersion of the surface wave, since $k_0^2 = k_x^2 + k_y^2 + k_z^2$. At low frequencies most of the power within these structures is flowing above the interface and the modal overlap of the associated mode

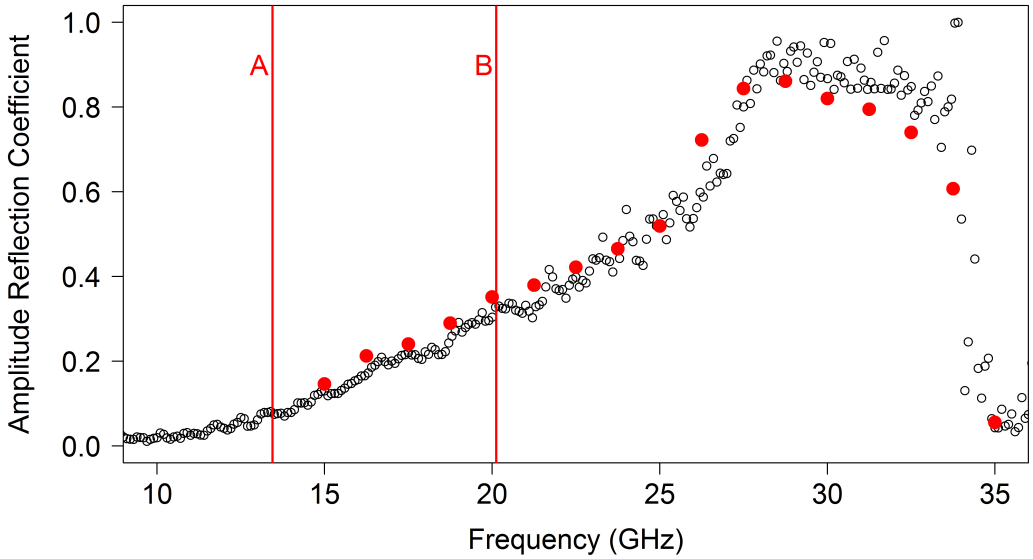

Figure 7.6: The surface wave reflection coefficient for a TM surface wave normally incident on the interface between the metal strip array and the metal post array. The experimental results are shown by the black circles and the FEM modelled reflection coefficient values are shown by the red points. The two 'impedance matched' frequencies are indicated by the vertical lines and labelled A and B respectively.

on each metasurface is high due to the relatively unconfined fields, i.e. the dispersion of the surface modes have gradients close to that of the light line. This in turn leads to a low reflection coefficient of a surface wave incident on the discontinuity between the two structures. However as the confinement of the mode increases, the fraction of the power flow below the surface of the metasurface within the dielectric core of the metallic strip array and the via layer of the post array, is also increasing. This increase occurs at different rates for the two structures, leading to an increasing modal mismatch.

The experimentally determined reflection coefficient (black circles), along with that predicted from FEM modelling (red points), is presented in figure 7.6 and contains several features of interest. The general form of the reflection coefficient is increasing approximately linearly above $\sim$12 GHz. At $\sim$27 GHz there is a sudden increase in the reflection coefficient which remains high, until $\sim$33 GHz at which point the reflection coefficient rapidly reduces to a minimum at $\sim$35 GHz. It can also be seen that there are no notable features associated with the 'impedance matched' conditions A and B, labelled by the vertical red lines.

The features in the reflection coefficient spectra are associated with points of inter-

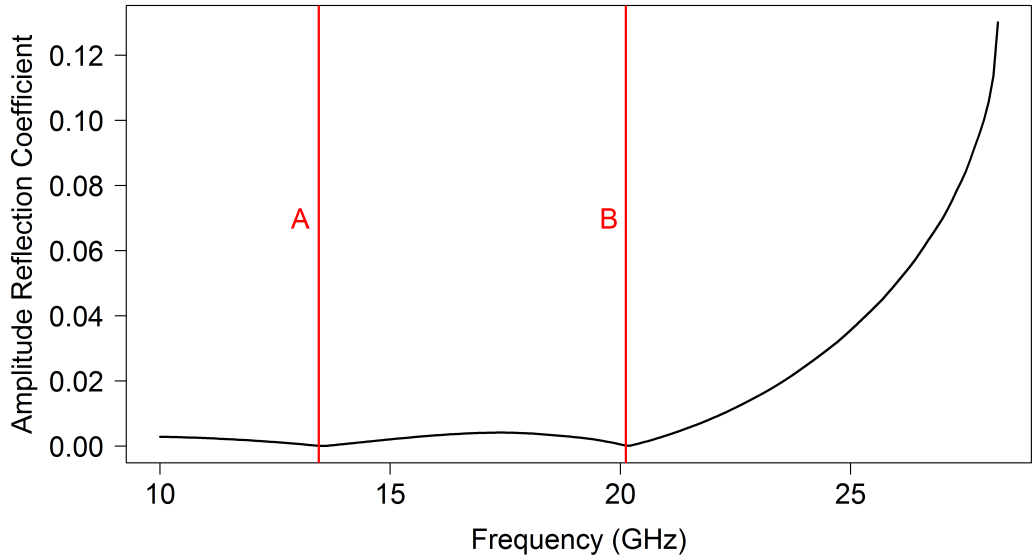

Figure 7.7: Analytically determined, using the impedance approximation, amplitude reflection coefficient of surface waves, black line, normally incident upon an impedance discontinuity equivalent to that for the metal strip metasurface to the post array metasurface. The amplitude reflection coefficient is shown to be equal to zero at the two 'impedance matched' conditions A and B indicated by the red lines.

est on the dispersions of the surface waves supported on the two metasurfaces. The increasing reflection coefficient at lower frequencies is associated with the increasing mismatch of the modal fields. Primarily this can be seen by the significant increase in the field strength within the dielectric core of the strip metasurface by comparison to that within the post metasurface. The sharp increase in the reflection coefficient at ~ 27 GHz is associated with the asymptotic frequency of the surface wave supported on the post metasurface. At frequencies close to the asymptote of the surface wave supported on the post array, the confinement of this mode increases significantly. Considering a surface wave incident from the strip array the rapidly increasing confinement also produces a rapidly increasing modal mismatch and therefore an increasing reflection coefficient at the interface of the metasurfaces. This increasing modal mismatch continues until the asymptotic frequency of the surface wave supported on the post metasurface (~ 27 GHz) is reached, beyond which surface waves are forbidden on the post metasurface. Finally the sudden decrease in the reflection coefficient at ~ 33 GHz is associated with the limit frequency of the fundamental TM surface wave on the strip metasurface. The reflection coefficient ceases to have any true meaning above this limit frequency (~ 33 GHz) since at these frequencies the radiation is effectively a grazing

photon. It can be seen that the agreement between the measured reflection coefficient and that predicted from FEM modelling is good throughout each of these features.

7.3.1 Impedance Matched Condition

The impedance approximation, described in section 2.4, has been utilised earlier in this study to predict the reflection coefficient of a metal patch array terminated to free space, Chapter 5. However it was shown that the approximation was only valid for low frequencies (less than ∼17.5 GHz) for the Sievenpiper 'mushroom' array. This approximation has been widely used when considering surface waves in the microwave regime [78–81, 140–142], but for metasurfaces this approximation is not accurate because it does not calculate any field below the interface. Clearly the reflection coefficient for the interface between two metasurfaces depends strongly on the field matching both above and below the surface, so this lack of treatment of the modal fields in the impedance approximation is seriously flawed.

It has been shown that the dispersions of the two surface modes cross at two frequencies at which the impedance of these surfaces will be equal. In the impedance approximation a surface wave incident upon the interface between two surfaces with the same impedance will undergo no reflection. However observation of the modelled fields (obtained using FEM modelling) of the eigenmode of each of these structures at the crossing points indicates that the modes themselves have significantly different field profiles, figure 7.8. The field within the slit array metasurface at the frequencies of the impedance matched conditions, ∼13.45 GHz (A) figure 7.8a and ∼20.12 GHz (B) figure 7.8c is primarily confined within the dielectric core of the metasurface. By contrast the field within the metallic post array, figures 7.8b and 7.8d, is mostly confined at the interface of the metasurface and the half-space above. It is clear that the field within the dielectric core of both metasurfaces is significantly different, and that the field is also different in the half space above the interface. In the impedance approximation the field below the interface is not calculated and the the fields above the interface must be identical at the impedance matched condition. In reality whilst the metasurfaces have the same surface impedance they do not have the same fields above or below the interface and therefore a non-zero reflection coefficient is inevitable.

It is also clear from figure 7.6 that the reflection coefficient at the 'impedance matched' conditions, ∼13.45 (A) and ∼20.12 (B) GHz, shows not only a non-zero reflection coefficient but no reduction in the reflection coefficient from the surrounding non-impedance matched frequencies. The reflection coefficient for the impedance approximation is presented in figure 7.7 and clear minima are indicated at the impedance matched frequencies. Thus use of an impedance surface to treat even this simple case

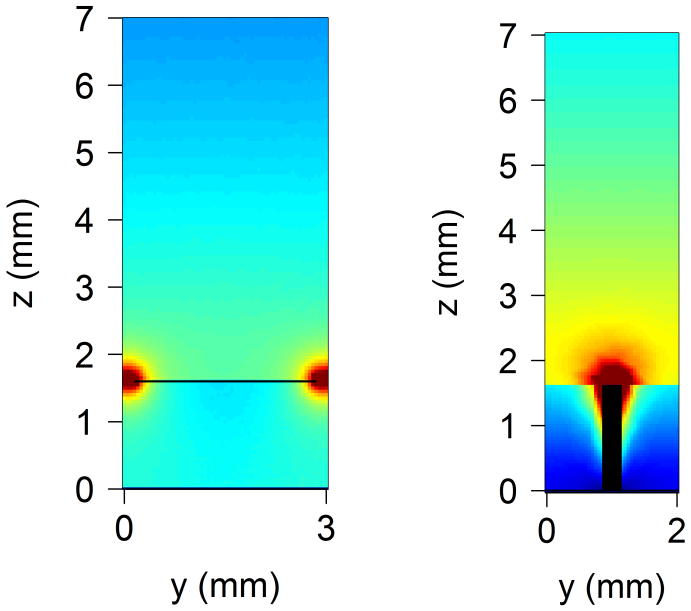

(a) Strip array at $k_x = 302.8$ (m^{-1}). (b) Post array at $k_x = 302.8$ (m^{-1}).

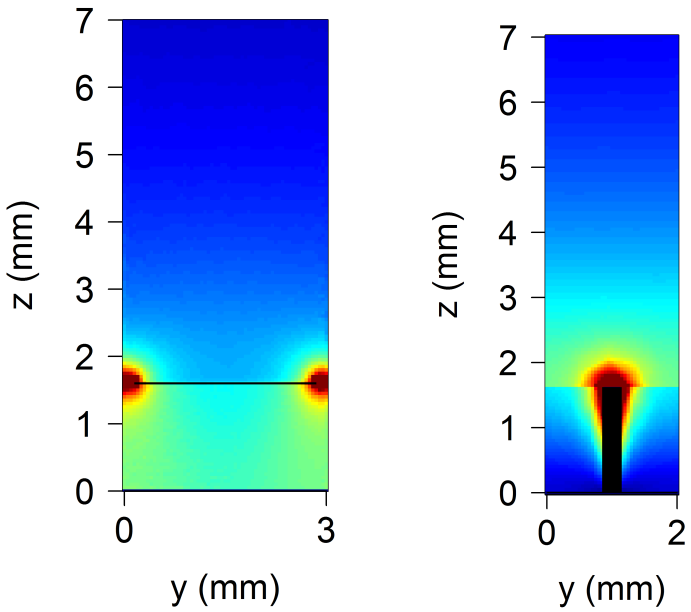

(c) Strip array at $k_x = 516.2$ (m^{-1}). (d) Post array at $k_x = 516.2$ (m^{-1}).

Figure 7.8: Time averaged electric field profiles associated with the TM surface waves supported on the metal strip metasurface and the metal post metasurface at the two 'impedance matched' conditions plotted across 1 unit cell. a) and b) (the strip and post array respectively) are associated with crossing point A and c) and d) (the strip and post array respectively) are associated with crossing point B. The fields are extracted from FEM modelling where red indicates high field strength and blue indicates low field strength and black represents metal.

of normal incidence reflection is totally inadequate.

7.4 Scattered Radiation

The scattered radiation resulting from the impedance discontinuity in the metasurface propagates primarily in the negative x-direction, figure 7.9. There is also a lower intensity scattered field in the forward x-direction above the post array metasurface ($x > 0$ mm). Isolating the backward scattered radiation from the surface wave incident upon the discontinuity from the radiation propagating in the forward direction from the source of the microwave surface waves is difficult. The interference of these waves can clearly be seen in the experimentally measured field plots, figure 7.9 $x < 0$ mm in the half space above. In these experimentally measured time-averaged electric field distributions the impedance discontinuity is at $x = 0$ mm. The direction of this scatter is interesting since the primary direction of scatter for the other planar discontinuities that have been studied in this thesis has always been in the forward direction of the incident surface wave.

The direction of this scatter has similarities to that obtained from FEM modelling, figure 7.10, and can be understood by consideration of the field profiles of the two TM surface waves. The mode supported by the metallic strips metasurface has a significant proportion of the power flowing within the dielectric core of the metasurface, figure 7.4. This is also evidenced by the field in below the strips ($z < 1.6$ mm) in figure 7.8. However for the array of metal posts metasurface the relative power flow within the dielectric core of the metasurface is much smaller and most of the power is above the metasurface interface. Therefore when the surface mode of the metal strips metasurface is incident upon the metal posts surface, where the electric field in the core is minimal, the mode can be considered to be incident upon a highly reflecting boundary. This can be seen by the consideration that the primary scatter direction (negative x-direction) present for the impedance mismatch between the two metasurfaces is similar in form to that for an infinitely high PEC termination of the metasurface. The modal mismatch of the fields is significant for these metasurfaces, indicated by the relative power flow, and as such boundary condition at the interface induces both backward and forward scatter in order to match the fields of the two modes.

7.5 Conclusion

In this chapter the impedance approximation, often used to describe metasurfaces, is investigated and shown to be an inadequate description of the surface waves supported on the metasurfaces used within this study. The amplitude reflection coefficient of a

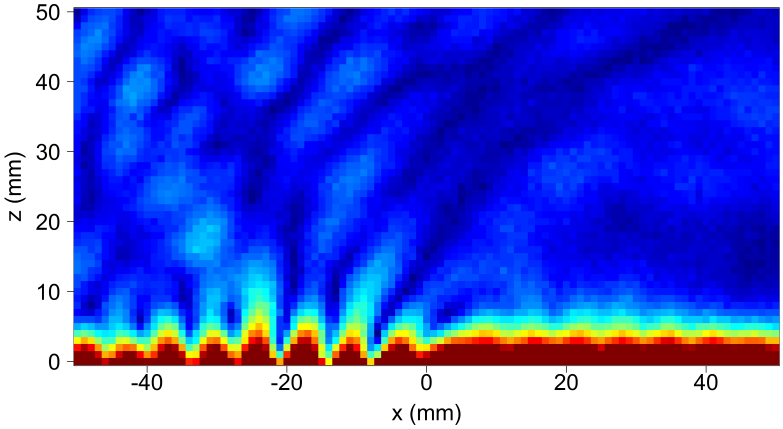

(a) 20 GHz

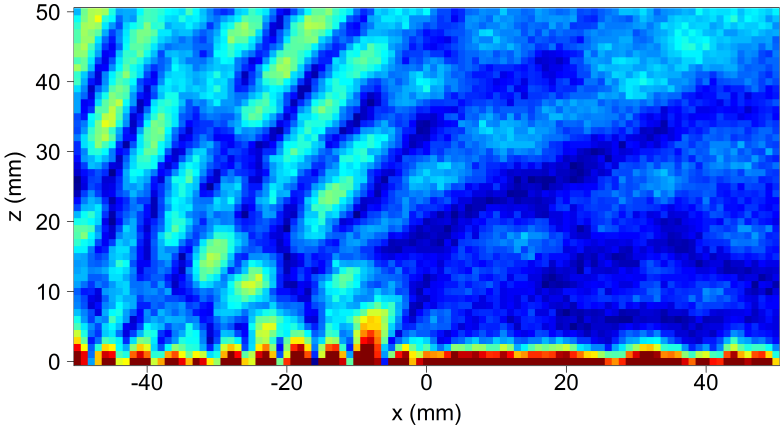

(b) 25 GHz

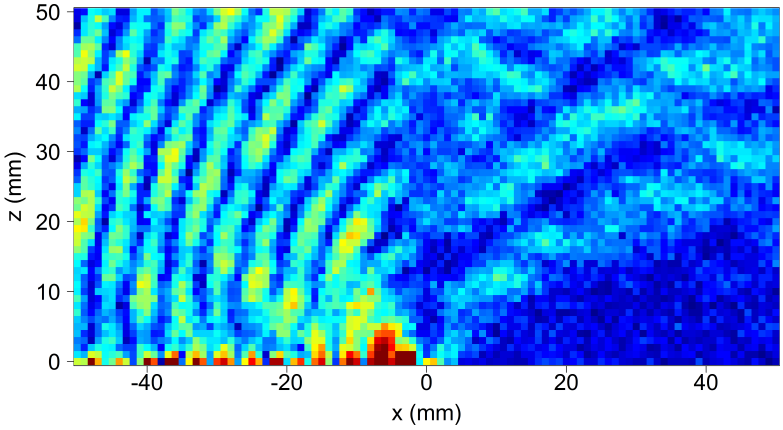

(c) 30 GHz

Figure 7.9: Experimentally characterised E_z-field above the discontinuity (at $x = 0$ mm) between the metal strip metasurface ($x < 0$ mm) and the metal post array metasurface ($x > 0$ mm) showing the scattered radiation at a) 20 GHz, b) 25 GHz and c) 30 GHz. Red indicates high field and blue indicates low field and black represents metal.

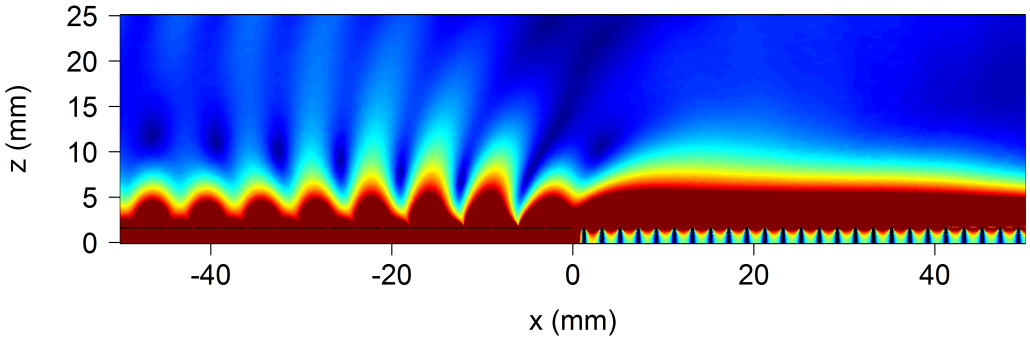

(a) 20 GHz

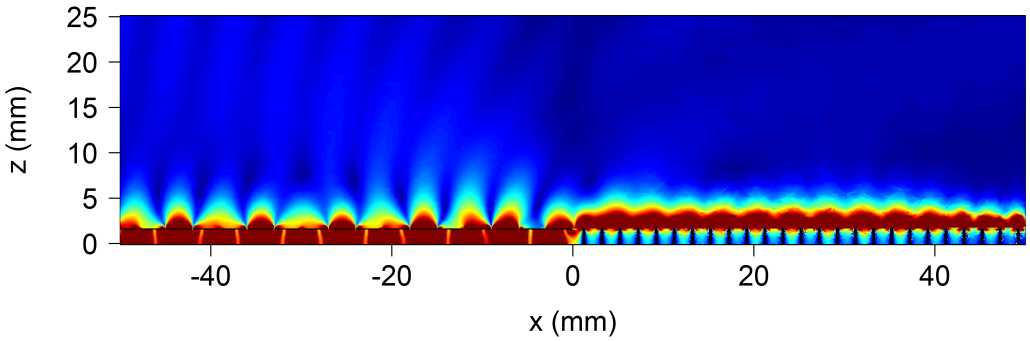

(b) 25 GHz

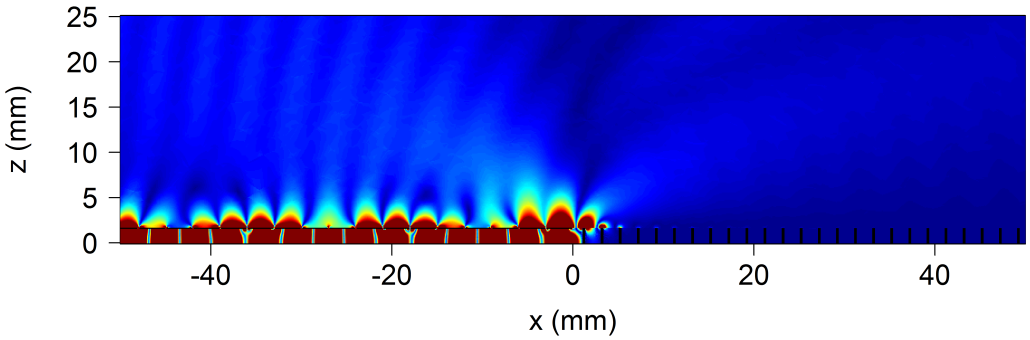

(c) 30 GHz

Figure 7.10: E_z-field extracted from FEM modelling of the 'impedance matched' metasurface both within the structures and above the metasurface interface (at $x = 0$ mm) at a) 20 GHz, b) 25 GHz and c) 30 GHz showing the scattered radiation in the $-x$-direction and the zero transmission due to the surface wave cutoff frequency of the metal post metasurface. Red indicates high field and blue indicates low field and black represents metal.

surface wave incident on the boundary between metasurfaces regions derived from the metal patch array and the Sievenpiper 'mushroom' metasurfaces is investigated. The metasurfaces used are an array of metal strips on a dielectric coated ground plane and an array of metal posts whose fundamental TM surface wave dispersions are shown to cross at two points. In the impedance approximation these surfaces are said to be 'impedance matched' at these frequencies and therefore no reflection is expected. However the reflection coefficient is in fact shown to be non-zero at these points. Not only is the reflection coefficient non-zero at these points, but there is also no observable reduction in the reflection coefficient at the frequencies associated with the crossings of the surface wave dispersions.

The inadequacy of the impedance description arises from the behaviour of the electric field within the metasurfaces which is not analytically described using the surface impedance approximation. The scattered radiation from the discontinuity is also shown to be similar in form to that from an infinitely high PEC termination of the metasurface. This is explained by the behaviour of the surface wave within the dielectric core of the two metasurfaces investigated, the vastly different field distributions leads to a near unity reflecting interface within the metasurfaces.

Chapter 8

Conclusions and Future Work

8.1 Summary of Thesis

This thesis describes the experimental investigation of the surface waves supported on metasurfaces, with a particular focus on the reflection of these surface waves from planar discontinuities. Various experimental techniques have been developed throughout this work to characterise surface-wave-supporting metasurfaces. A new technique for measuring the dispersion of metasurfaces is presented in section 3.5, involving the use of near-field coaxial probes as both sources and detectors of microwave surface waves, and a collimating mirror system. The near-field associated with the surface waves has also been characterised by combining the near-field coaxial probes with a 3-axis translation stage described in section 3.6. A device for launching planar phase front surface waves has been developed using a parallel plate waveguide and a dielectric lens presented in section 3.7 and finally a technique for measuring the surface wave reflection coefficient has been developed and discussed in section 3.8.

In Chapter 4 the dispersion of surface waves on a square array of square cross-section metal pillars has been fully characterised and compared to FEM modelling. The results show that a family of surface waves may be supported by pillar or crossed slit structures rather than just holes even though there is now no lowest cut-off frequency. A family of TM surface modes have been shown to exist with dispersions with asymptotic frequencies defined by the pillar heights (slit depth) and the refractive index of the material filling the slits. The concept of 'designer' surface plasmons at microwave frequencies has thereby been extended experimentally to a whole new class of structured metasurfaces. This work has subsequently been extended by Kim et. al. [143] to show that this class of metasurface can be designed to include self collimation and beam splitting of the surface waves supported by such a structure. The investigation of this structure focussed on the amplitude reflection coefficient of surface waves

incident on the termination of this metasurface to free space. A series of amplitude reflection coefficient peaks are shown to exist close to the surface wave asymptotes associated with standing waves defined by the depth of the slits. This structure served as a test-bed for experimental technique development and similar investigations were then performed with thin, lightweight metasurfaces which support surface waves in the microwave regime.

Chapters 5, 6 and 7 focussed on the surface wave properties associated with a square array of square metal patches on a dielectric coated ground plane and a Sievenpiper 'mushroom' metasurface. In Chapter 5 the amplitude reflection coefficient of surface waves incident upon the termination of these metasurfaces to free space has been determined. The electric field associated with both the surface waves and the scattered radiation has also been fully characterised using the field mapping techniques developed in this thesis and results show good agreement to FEM modelling. An analytical model for the amplitude reflection coefficient for the patch array metasurface agrees well with the experimental data. However for the Sievenpiper 'mushroom' metasurface the analytical model and experimental data strongly diverge at higher frequencies. This divergence is caused by the surface wave properties of the Sievenpiper 'metasurface', most notably the decrease in the surface wave propagation length at frequencies close to the asymptote of the fundamental TM mode. The reflection coefficient is shown to increase significantly with the confinement of the surface mode. The variation of this confinement with frequency is different for the two metasurfaces considered due to their dispersions. This increase in the reflection coefficient is caused by both the momentum mismatch of the surface wave compared to the freely propagating modes and the different field distributions of the two modes.

In Chapter 6 the reflection coefficient of surface waves supported on a metasurface incident upon a dielectric overlayer on that metasurface has been experimentally characterised for the metal patch array and Sievenpiper 'mushroom' metasurfaces. It is shown that the addition of a thin, significantly subwavelength, dielectric overlayer onto the metal patch array metasurface vastly perturbs the surface wave dispersion. The reflection coefficient of the surface waves, supported on the metal patch array metasurface, incident upon the dielectric coated metasurface are shown to vary significantly with both the frequency of the radiation and the thickness of the dielectric overlayer. The variation of the reflection coefficient with frequency is determined by the confinement of the surface wave with respect to the overlayer thickness and the power flow within the metasurface structure. This leads to two different regions within the reflection coefficient spectrum where initially the reflection coefficient is increasing with increasing frequency due to the increasing confinement of the surface wave whilst at higher frequencies the reflection coefficient decreases due to the increasing power

flow within the metasurface structure. It has been shown that the reflection coefficient, measured at a single frequency, as a function of overlayer thickness has an asymptotic limit. This maximum reflection coefficient value is larger for lower frequencies due to the reduced power flow within the metasurface by comparison to higher frequencies.

The reflection coefficient of a surface wave incident upon a coated Sievenpiper 'mushroom' metasurface is significantly different since the surface wave stop band of the Sievenpiper 'mushroom' metasurface leads to near complete reflection of the surface waves when their transmission is forbidden. The scattered radiation associated with the reflection coefficient of the surface waves supported on the Sievenpiper 'mushroom' structure has also been mapped. The reduction of the reflection coefficient for surface waves incident upon the interface between a coated and uncoated metasurface has applications in the design of efficient surface wave absorbing materials for the reduction of radar cross section. This technique for measuring the reflection coefficient of such overlayers can be implemented to characterise the performance of such absorbers.

Finally in Chapter 7 the impedance approximation, often used to describe metasurfaces, is investigated and shown to be an incomplete description for the surface waves supported on the metasurfaces used within this study. The amplitude reflection coefficient of a surface wave incident on the boundary between two metasurfaces derived from the metal patch array metasurface and the Sievenpiper 'mushroom' metasurface is investigated. The metasurfaces used are an array of metal strips on a dielectric coated ground plane and an array of metal posts whose fundamental TM surface wave dispersions are shown to cross at two points. In the impedance approximation these surfaces are said to be 'impedance matched' at these frequencies and therefore no reflection is expected however the reflection coefficient is shown to be non-zero at these points. Not only is the reflection coefficient non-zero at these points but there is also no observable reduction in the reflection coefficient at the frequencies associated with the crossings of the surface wave dispersions.

The inadequacy of the impedance description arises from the behaviour of the electric field within the metasurfaces which is not analytically described using the surface impedance approximation. The scattered radiation from the discontinuity is also shown to be similar in form to that from an infinitely high PEC termination of the metasurface. This is explained by the behaviour of the surface wave within the dielectric core of the two metasurfaces investigated; the vastly different field distributions lead to a near unity reflecting interface within the metasurfaces.

8.2 Future Work

Throughout this thesis the reflection coefficient of surface waves incident upon various planar discontinuities has been investigated from which a wealth of future research can be performed.

Techniques for suppressing the reflection of surface waves at planar discontinuities are of great interest for improving the efficiency of surface wave devices. It is expected that the simplest technique for reducing the reflection coefficient of surface waves incident upon discontinuities is to 'grade' the discontinuity. For the types of discontinuities presented in this thesis it is expected that this can be achieved for both the dielectric overlayer and the impedance discontinuity. For the dielectric overlayer the reflection coefficient can be significantly reduced by introducing a linear increase in the thickness of the overlayer over a distance greater than the wavelength of the surface wave. A full investigation of the form of the taper required to eliminate the reflection of such a system would be of use for designing surface wave absorbing overlayers. These surface wave absorbers would be useful in preventing the reflection of surface waves from the edges of the surface-wave-supporting metasurface characterised within this thesis and

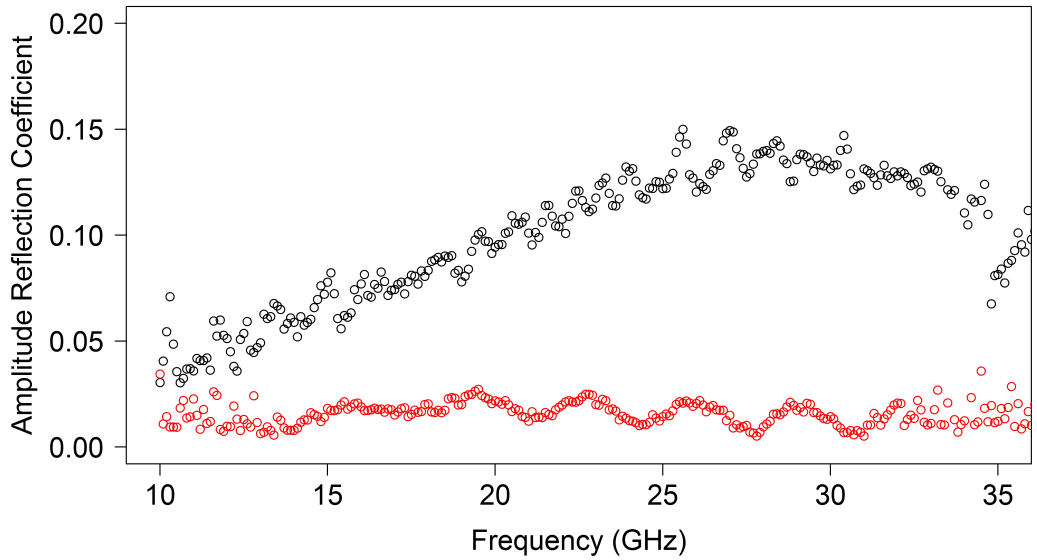

Figure 8.1: Experimentally measured amplitude reflection coefficient of a surface wave, supported on the metal patch array metasurface, incident upon a 2.85 mm thickness dielectric coating ($\varepsilon \approx 3.15$) (black points). The addition of a linear taper, of length 40 mm, reduces the amplitude reflection coefficient of a surface wave incident upon the dielectric coating (red points).

in other industrial applications. Initial experimental results showing the reduction of the reflection coefficient when a linear taper is added to a dielectric overlayer are shown in figure 8.1. The experimentally investigated system explores the reflection coefficient of a surface wave incident upon the 2.85 mm thick dielectric overlayer ($\varepsilon \approx 3.15$) on the metal patch metasurface investigated in Chapter 6. The addition of a linear taper in the thickness of the coating over 40 mm reduces the amplitude reflection coefficient at all investigated frequencies to less than 0.03.

Using this technique, combined with an engineered metasurface dispersion, it may be possible to create surface wave lenses to control the propagation of surface waves using dielectric coatings. In this application the reduction of the reflection of a surface wave incident on the lens would be a crucial factor in the performance of such a system.

The reduction of the reflection for the impedance discontinuity is a significantly more challenging prospect. For such a system it is required that the dispersion of the surface wave supported on the metasurface changes smoothly over a distance greater than a wavelength. Once again it is expected that the metasurface structure can be 'graded' to reduce the reflection coefficient of the interface. The height of the metal pillars can be slowly increased at the same time as the metal strip width can be gradually reduced. In this manner the surface wave dispersion is expected to vary much more slowly between the two meatusrfaces thereby reducing the reflection coefficient. Similarly the grading of the metasurface structure could be used to reduce the group velocity of the surface wave such that the surface wave may be absorbed without significant reflection. This technique could be utilised to produce surface wave absorbing structures that are lightweight and have significantly subwavelength thicknesses.

Finally the surface waves studied within this thesis are TM polarised, this study could be subsequently extended to study the reflection coefficients of TE surface waves supported on metasurface structures. The boundary conditions for such surface waves at the planar discontinuities discussed in this thesis will be significantly different than those for TM surface waves. As such the reflection coefficient for TE surface waves may be expected to have vastly different forms than those of TM surface waves.

Chapter 9

Publications and Conferences

9.1 Publications

- Berry, S.J., Campbell, T., Hibbins, A.P., Sambles, J.R. Surface Wave Resonances Supported on a Square Array of Square Metallic Pillars. *Applied Physics Letters*, **100**, 101107 (2012).

- Dockrey, J.A., Lockyear, M.J., Berry, S.J., Horsely, A.R., Sambles, J.R., Hibbins, A.P. Thin Metamaterial Luneburg Lens for Surface Waves. *Phys. Rev. B.*, **87**, 125137 (2013).

9.2 Conference Presentations

9.2.1 Oral Presentations

- PIERS 2013, Berry, S.J., Horsley, S.A.R., Hibbins, A.P., Sambles, J.R. Surface Wave Reflection, Transmission and Scattering from an Impedance Discontinuity. Stockholm, Sweden. August 2013.

- CIMTEC 2012, Berry, S.J., Campbell, T., Hibbins, A.P., Sambles, J.R. Surface Wave Resonances Supported on a Square Array of Square Metallic Pillars. Montecatini Terme, Italy. June 2012.

9.2.2 Poster Presentations

- ONYX 2011, Berry, S.J., Campbell, T., Hibbins, A.P., Sambles, J.R. Surface Wave Resonances Supported on a Square Array of Square Metallic Pillars. Bath, England. May 2011.

Appendices

Appendix A

Nicolson Ross Wier Derivation

Determining the complex permittivity and permeability of an unknown material is important in the design of both metamaterials and the absorbing and non-absorbing overlayers. The Nicolson-Ross-Weir (NRW) equations derive these material parameters from the complex reflection and transmission S-parameters for a slab of material completely filling the cross-section of a reflectionless waveguide. The derivation of these material parameters from the S-parameters is presented here for the particular case of a standard rectangular waveguide. Considering the sum of single interface Fresnel equations for both the interfaces of the material, figure A.1, the total reflection can be written as follows:

$$r_{13} = r_{12} + t_{12}r_{23}t_{21}exp(2i\alpha) + t_{12}r_{23}^2r_{21}t_{21}exp(4i\alpha) + ... \tag{A.1}$$

Equation A.1 can be written as the following sum:

$$r_{13} = r_{12} + t_{12}t_{21}r_{23}exp(2i\alpha)\sum_{n=0}^{\infty} r_{21}^n r_{23}^n exp(2ni\alpha) \tag{A.2}$$

Using the identity A.3 we can simplify equation A.2:

$$\sum_{n=0}^{\infty} x^n = \frac{1}{1-x} \tag{A.3}$$

$$r_{13} = r_{12} + \frac{t_{12}t_{21}r_{23}exp(2i\alpha)}{1 - r_{21}r_{23}exp(2i\alpha)} \tag{A.4}$$

A substitution can be made for the single interface Fresnel reflection coefficients and the phase factor, $exp(2i\alpha)$, in order to express the Fresnel reflection coefficient of the slab, r_{13}, in terms of the single interface Fresnel reflection coefficient for an infinitely thick slab of the material and a complex exponential related to the propagation constant

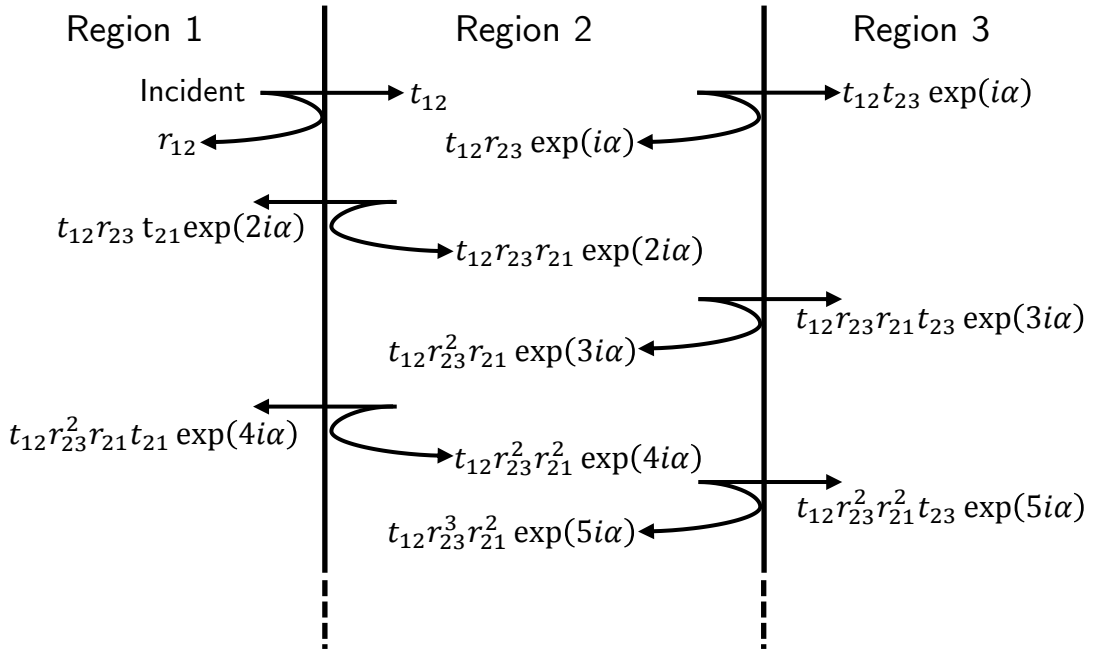

Figure A.1: Schematic diagram of the multiple reflections in a slab of material where r_{xy} and t_{xy} are the single interface Fresnel amplitude reflection coefficients where x is the index for the region of the incident and reflected wave and y is the index for the region of the transmitted wave.

within the material. The total Fresnel reflection coefficient, r_{13}, is equivalent to the reflected S-parameter, S_{11}, measured in experiment and the substitutions are shown in equations A.5 to A.9.

$$r_{21} = r_{23} = -r_{12} \; where \; r_{12} = \frac{Z-1}{Z+1} \tag{A.5}$$

$$\beta^2 = exp(-2i\alpha) \; where \; \alpha = 2\pi\gamma d \tag{A.6}$$

$$t_{12} = 1 + r_{21} \tag{A.7}$$

$$t_{21} = 1 + r_{12} \tag{A.8}$$

$$S_{11} = \frac{r_{12}(1-\beta^2)}{1 - r_{12}^2\beta^2} \tag{A.9}$$

Transmission through the slab of material within the waveguide can also be determined through another infinite sum of single interface Fresnel reflection coefficients. Another identical procedure can be used to determine the transmission S-parameter,

S_{21}, in terms of the single interface Fresnel reflection coefficient, r_{12}, and the complex exponential defined in equation A.6, β, as shown below:

$$t_{13} = \frac{t_{12}t_{23}exp(i\alpha)}{1 - r_{21}r_{23}exp(2i\alpha)} \tag{A.10}$$

$$\text{where } t_{23} = 1 + r_{23} \tag{A.11}$$

$$S_{21} = \frac{\beta(1 - r_{12}^2)}{1 - r_{12}^2\beta^2} \tag{A.12}$$

The two experimentally obtainable parameters S_{11} and S_{21} have been expressed in terms of the single interface Fresenel reflection coefficient r_{12} and a complex exponential term β. These two terms r_{12} and β are determined by the complex permittivity and permeability of the unknown material within the waveguide. Expressions for the two unknowns are obtained by a combination of the sum and difference of the S-parameters as shown below:

$$V_1 = S_{21} + S_{11} \tag{A.13}$$

$$V_2 = S_{21} - S_{11} \tag{A.14}$$

$$V_1V_2 = S_{21}^2 - S_{11}^2 = \frac{\beta^2 - r_{12}^2}{1 - r_{12}^2\beta^2} \tag{A.15}$$

$$V_1 - V_2 = 2S_{11} = \frac{2r_{12}(1 - \beta^2)}{1 - r_{12}^2\beta^2} \tag{A.16}$$

$$X = \frac{1 - V_1V_2}{V_1 - V_2} \tag{A.17}$$

$$\sqrt{X^2 - 1} = \frac{r_{12}^2 - 1}{2r_{12}} \tag{A.18}$$

$$r_{12} = X \pm \sqrt{X^2 - 1} \tag{A.19}$$

The choice of sign in equation A.19 is determined by the physical constraint that $|r_{12}| \leq 1$ since the amplitude of the reflection can never be greater than the incident amplitude. The characteristic impedance of the filled section of waveguide can now be calculated by rearranging equation A.5 to make the impedance Z the subject. r_{12} is now used along with S_{11} and S_{21} to determine β, the complex eponential:

$$V_1 - r_{12} = \frac{(1 - r_{12}^2)(\beta - \beta^2 r_{12}^2)}{1 - r_{12}^2 \beta^2} \tag{A.20}$$

$$1 - V_1 r_{12} = \frac{1 - \beta r_{12} + \beta r_{12}^3 - r_{12}^2}{1 - r_{12}^2 \beta^2} \tag{A.21}$$

$$\frac{V_1 - r_{12}}{1 - V_1 r_{12}} = \left(\frac{(1 - r_{12}^2)(\beta - \beta^2 r_{12}^2)}{1 - r_{12}^2 \beta^2} \right) \left(\frac{1 - r_{12}^2 \beta^2}{1 - \beta r_{12} + \beta r_{12}^3 - r_{12}^2} \right) \tag{A.22}$$

$$\frac{V_1 - r_{12}}{1 - V_1 r_{12}} = \frac{\beta(1 - \beta r_{12})}{1 - \beta r_{12}} = \beta \tag{A.23}$$

The complex exponential term is related to the propagation constant of the material within the waveguide, as shown in equation A.6. A simple rearrangement is performed to determine the propagation constant of the material. The addition of the integer m is used to take account of samples whose phase change is greater than 2π since the natural log has multiple roots the value m is used to differentiate between them. m is zero for all samples whose optical thickness is smaller than the wavelength of the radiation.

$$\beta^2 = exp(-i4\pi(\gamma d + m)) \text{ where } m \text{ is an integer} \tag{A.24}$$

$$\ln(\beta) = -i(2\pi\gamma d + 2\pi m) \tag{A.25}$$

$$\gamma = \frac{i \ln(\beta) - 2\pi m}{2\pi d} \tag{A.26}$$

The material's complex permittivity and permeability are determined from the sample thickness, d, propagation constant, γ, and the normalised characteristic impedance of the filled section of the waveguide, Z. Corrections must be made to the expressions which vary depending on the geometry of the waveguide and the field of the fundamental mode since the normalised characteristic impedance, Z, is compared to the impedance of the unfilled waveguide section. Below we present the equations to determine the material parameters for the rectangular waveguide system used in this study.

The wavelength inside a rectangular waveguide, λ_g, is different from the free space wavelength, λ_0, due to the quantisation of the fundamental waveguide mode across the guide cross-section. The quantisation, seen in figure 3.4, adds momentum in the y-direction such that the momentum of the mode in the direction of propagation is reduced.

$$k_x = \sqrt{k_0^2 - k_y^2} \tag{A.27}$$

$$\left(\frac{2\pi}{\lambda_g}\right) = \sqrt{\left(\frac{2\pi}{\lambda_0}\right)^2 - \left(\frac{2\pi}{\lambda_c}\right)^2} \tag{A.28}$$

$$\lambda_g = \frac{\lambda_0}{\sqrt{1 - \left(\frac{\lambda_0}{\lambda_c}\right)^2}} \tag{A.29}$$

Here λ_c is the wavelength of the low frequency cutoff of the TE_{10} mode within the rectangular waveguide which is equivalent to twice the length of the long side of the rectangle. The propagation constant of the material is related to the refractive index of the material filling the waveguide, N, and the wavelength of the TE_{10} mode propagating within the waveguide, λ_g.

$$\gamma = \frac{N}{\lambda_g} \tag{A.30}$$

Therefore it is possible to determine the refractive index of the material within the waveguide and by combining the refractive index of the material with its characteristic impedance the permittivity and permeability may be obtained.

$$\mu = N \times Z \tag{A.31}$$

$$\varepsilon = \frac{N}{Z} \tag{A.32}$$

The weakness in the derivation of the material parameters of the material filling the waveguide via this method is the knowledge of integer m. If the approximate values of the material parameters are not known then the value of m will be difficult to predict. This difficulty can be overcome by measurement of the time taken for a wave to be transmitted through the unknown material to estimate the refractive index and therefore the value of m required. These equations have been used to determine the material properties of various dielectric and magnetic composite materials used within this thesis, the method for which has been described in section 3.3.

A. Nicolson Ross Wier Derivation

References

[1] Wood, R.W. On a Remarkable Case of Uneven Distribution of Light in a Diffraction Grating Spectrum. *Proceedings of the Physical Society of London*, **18**, 269 (1902). 1, 5

[2] Fano, U. The Theory of Anomalous Diffraction Gratings and of Quasi-Stationary Waves on Metallic Surfaces (Sommerfeld. *Journal of the Optical Society of America*, **31**, 213 (1941). 1

[3] Zenneck, J. Über die Fortpflanzung ebener elektromagnetischer Wellen längs einer ebenen Leiterfläche und ihre Beziehung zur drahtlosen Telegraphie. *Ann. Phys*, **23**, 846 (1907). 1, 5

[4] Brillouin, L. Wave Guides for Slow Waves. *Journal of Applied Physics*, **19**, 1023 (1948).

[5] Elliott, R. On the Theory of Corrugated Plane Surfaces. *Transactions of the IRE Professional Group on Antennas and Propagation*, **2**, 71 (1954). 1, 6, 13

[6] Rotmant, W. A Study of Single-Surface Corrugated Guides. *Proceedings of the I.R.E*, **21**, 952 (1951). 13

[7] Harvey, A. Periodic and Guiding Structures at Microwave Frequencies. *IRE Transactions on Microwave Theory and Techniques*, pages 30–61 (1960). 6

[8] Sommerfeld, A. Ueber die Fortpflanzung elektrodynamischer Wellen längs eines Drahtes. *Annalen der Physik*, **303**, 233 (1899).

[9] Sommerfeld, A. Über die Ausbreitung der Wellen in der drahtlosen Telegraphie. *Annalen der Physik*, **333**, 665 (1909). 1

[10] Barlow, H.M. Surface waves. *Quarterly of Applied Mathematics*, **7**, 21 (1949). 1, 6

[11] Cullen, A.L. The excitation of plane surface waves. *Monograph Radio Section*, **13** (1954).

[12] Cutler, C. Genesis of the corrugated electromagnetic surface. *Proceedings of IEEE Antennas and Propagation Society International Symposium and URSI National Radio Science Meeting*, **3**, 1456 (1994). 1, 6

[13] Qiu, M. Photonic band structures for surface waves on structured metal surfaces. *Optics express*, **13**, 7583 (2005). 1, 57

[14] Hibbins, A.P., Evans, B.R., and Sambles, J.R. Experimental verification of designer surface plasmons. *Science (New York, N.Y.)*, **308**, 670 (2005). 6, 55, 56, 57, 68

[15] Garcia-Vidal, F.J., Martín-Moreno, L., and Pendry, J.B. Surfaces with holes in them: new plasmonic metamaterials. *Journal of Optics A: Pure and Applied Optics*, **7**, S97 (2005). 6

[16] Lan, Y.C. and Chern, R.L. Surface plasmon-like modes on structured perfectly conducting surfaces. *Optics express*, **14**, 11339 (2006). 7

[17] Hibbins, A., Lockyear, M., and Sambles, J. Coupled surface-plasmon-like modes between metamaterial. *Physical Review B*, **76**, 165431 (2007). 7

[18] Hao, J., Yuan, Y., Ran, L., Jiang, T., Kong, J., Chan, C., and Zhou, L. Manipulating Electromagnetic Wave Polarizations by Anisotropic Metamaterials. *Physical Review Letters*, **99**, 063908 (2007).

[19] Xue, L. and Fusco, V. Printed Holey Plate Luneburg Lens. *Microwave and Optical Technology Letters*, **50**, 378 (2007). 1, 5

[20] Pendry, J.B., Martín-Moreno, L., and Garcia-Vidal, F.J. Mimicking surface plasmons with structured surfaces. *Science (New York, N.Y.)*, **305**, 847 (2004). 1, 5, 6, 55, 56, 57, 68

[21] Maagt, P.D., Member, S., Vardaxoglou, Y.C., and Baracco, J.m. Electromagnetic Bandgap Antennas and Components for Microwave and (Sub) Millimeter Wave Applications. *IEEE Transactions on Antennas and Propagation*, **51**, 2667 (2003). 1

[22] Sievenpiper, D., Broas, R., Alexopolous, N., and Yablonovitch, E. High-impedance electromagnetic surfaces with a forbidden frequency band. *IEEE Transactions on Microwave Theory and Techniques*, **47**, 2059 (1999).

[23] Feresidis, A.P., Apostolopoulos, G., Serfas, N., and Vardaxoglou, J.C. Closely Coupled Metallodielectric Electromagnetic Band-Gap Structures Formed by Double-Layer Dipole and Tripole Arrays. *IEEE Transactions on Antennas and Propagation*, **52**, 1149 (2004).

[24] Abhari, R. and Eleftheriades, G.V. Metallo-Dielectric Electromagnetic Bandgap Structures for Suppression and Isolation of the Parallel-Plate Noise in High Speed Circuits. *IEEE Transactions on Microwave Theory and Techniques*, **51**, 1629 (2003). 1

[25] Rahmat-Samii, Y. Microstrip antennas integrated with electromagnetic bandgap (EBG) structures: A low mutual coupling design for array applications. *IEEE Transactions on Antennas and Propagation*, **51**, 2936 (2003). 1

[26] Qian, Y., Coccioli, R., Sievenpiper, D., Radisic, V., and Yablonovitch, E. A microstrip patch antenna using novel photonic band-gap structures. *Microwave Journal*, **66**, 1 (1999).

[27] Mosallaei, H. and Sarabandi, K. Antenna Miniaturization and Bandwidth Enhancement Using a Reactive Impedance Subsrate. *IEEE Transactions on Antennas and Propagation*, **52**, 2403 (2004).

[28] Erdemli, Y., Sertel, K., Gilbert, R., Wright, D., and Volakis, J. Frequency-selective surfaces to enhance performance of broad-band reconfigurable arrays. *IEEE Transactions on Antennas and Propagation*, **50**, 1716 (2002).

[29] Wang, S., Feresidis, A.P., Goussetis, G., and Vardaxoglou, J.C. Low-profile resonant cavity antenna with artificial magnetic conductor ground plane. *ELECTRONICS LETTERS*, **40**, 10 (2004). 1

[30] Lee, Y., Chauraya, A., Lockyer, D., and Vardaxoglou, J. Dipole and tripole metallodielectric photonic bandgap (MPBG) structures for microwave filter and antenna applications. *IEE Proceedings*, **147**, 395 (2000). 1

[31] Zhang, Y., von Hagen, J., Younis, M., Fischer, C., and Wiesbeck, W. Planar Artifical Magnetic Conductors and Patch Antennas. *IEEE Transactions on Antennas and Propagation*, **51**, 2704 (2003). 1

[32] Yang, F.r., Ma, K.p., Qian, Y., and Itoh, T. A Novel TEM Waveguide Using Uniplanar Compact Photonic-Bandgap (UC-PBG) Structure. *IEEE Transactions on Microwave Theory and Techniques*, **47**, 2092 (1999). 1

[33] Grant, R. Understanding Stealth and Aircraft Survivability. *IRIS Independent Research* (1998). 1

[34] Petrov, V.M. and Gagulin, V.V. Microwave Absorbing Materials. *Inorganic Materials*, **37**, 93 (2001). 1

[35] Niemand, P. and Odendaal, J.W. Characterization of Surface Wave Radar Absorbing Material. *Microwave and Optcial Technology Letters*, **20**, 131 (1999). 1

[36] Liu, Y. and Zhang, X. Metasurfaces for manipulating surface plasmons. *Applied Physics Letters*, **103**, 141101 (2013). 5

[37] Zheludev, N. The Road Ahead for Metamaterials. *Science (New York, N.Y.)*, **328**, 582 (2010). 5

[38] Uller, K. *Thesis*. Ph.D. thesis, University Rostock (1903). 5

[39] Wait, J.R. On the Excitation of Electromagnetic Surface Waves on a Curved Surface. *IRE Transactions on Antennas and Propagation* (1960). 5

[40] Murray, W. and Barnes, W. Plasmonic Materials. *Advanced Materials*, **19**, 3771 (2007). 5, 7

[41] Berry, S.J., Campbell, T., Hibbins, a.P., and Sambles, J.R. Surface wave resonances supported on a square array of square metallic pillars. *Applied Physics Letters*, **100**, 101107 (2012). 6, 68

[42] Barnes, W.L., Dereux, A., and Ebbesen, T.W. Surface Plasmon Subwavelength Optics. *Nature*, **424**, 824 (2003).

[43] Clavijo, S., Díaz, R.E., and Mckinzie, W.E. Design Methodology for Sievenpiper High-Impedance Surfaces : An Artificial Magnetic Conductor for Positive Gain Electrically Small Antennas. *October*, **51**, 2678 (2003). 24, 26

[44] Goussetis, G., a.P. Feresidis, and Vardaxoglou, J. Tailoring the AMC and EBG Characteristics of Periodic Metallic Arrays Printed on Grounded Dielectric Substrate. *IEEE Transactions on Antennas and Propagation*, **54**, 82 (2006). 18, 68

[45] Hendry, E., Hibbins, a., and Sambles, J. Importance of diffraction in determining the dispersion of designer surface plasmons. *Physical Review B*, **78**, 1 (2008). 62

[46] Hibbins, A.P., Lockyear, M.J., and Sambles, J.R. Surface-plasmon-like modes on ultra-thin metamaterials. *3rd International Congress on Advanced Electromagnetic Materials in Microwaves and Optics*, pages 357–359 (2009).

[47] Jiang, T., Shen, L., Zhang, X., and Ran, L. High-Order Modes of Spoof Surface Plasmon Polaritons on Peridoically Corrugated Metal Surfaces. *Progress in Electromagnetics Research*, **8**, 91 (2009). 57, 68

[48] Lockyear, M., Hibbins, A., and Sambles, J. Microwave Surface-Plasmon-Like Modes on Thin Metamaterials. *Physical Review Letters*, **102**, 1 (2009).

[49] Rance, H.J., Hooper, I.R., Hibbins, A.P., and Roy Sambles, J. Structurally dictated anisotropic designer surface plasmons. *Applied Physics Letters*, **99**, 181107 (2011). 6, 55, 56, 57, 68

[50] Cullen, A.L. and Barlow, H. Surface Waves. *Components* (1953). 6

[51] Zucker, F. Theory and Applications of Surface Waves. *Supplemento Al*, **IX**, 450 (1952). 6

[52] John, G. Electromagnetic surface waveguides a review. *IEEE Proceedings India*, page 139 (1977). 6

[53] Ulrich, R. Submillimeter waveguiding on periodic metal structure. *Applied Physics Letters*, **22**, 251 (1973). 6

[54] Attwood, S.S. Surface Wave Propagation Over a Coated Plane Conductor. *Jounral of Applied Physics*, **22**, 504 (1951). 6

[55] Williams, C.R., Andrews, S.R., Maier, S.a., Fernández-Domínguez, a.I., Martín-Moreno, L., and García-Vidal, F.J. Highly confined guiding of terahertz surface plasmon polaritons on structured metal surfaces. *Nature Photonics*, **2**, 175 (2008). 6

[56] Rodriguez, S., Schaafsma, M., Berrier, a., and Gómez Rivas, J. Collective resonances in plasmonic crystals: Size matters. *Physica B: Condensed Matter*, **407**, 4081 (2012).

[57] Bravo-Abad, J., Martín-Moreno, L., García-Vidal, F., Hendry, E., and Gómez Rivas, J. Transmission of light through periodic arrays of square holes: From a metallic wire mesh to an array of tiny holes. *Physical Review B*, **76**, 241102 (2007).

[58] Rivas, J.G. Terahertz: the art of confinement. *Nature Photonics*, **2**, 137 (2008).

[59] Abass, A., Rodriguez, S.R.K., and Maes, B. Tailoring Dispersion and Eigenfield Profiles of Plasmonic Surface Lattice Resonances. *American Chemical Society Photonics* (2013). 6

[60] García de Abajo, F. and Sáenz, J. Electromagnetic Surface Modes in Structured Perfect-Conductor Surfaces. *Physical Review Letters*, **95**, 233901 (2005). 7

[61] Maier, S., Andrews, S., Martín-Moreno, L., and García-Vidal, F. Terahertz Surface Plasmon-Polariton Propagation and Focusing on Periodically Corrugated Metal Wires. *Physical Review Letters*, **97**, 176805 (2006).

[62] Garcia-Vidal, F.J., Martin-Moreno, L., Ebbesen, T.W., and Kuipers, L. Light passing through subwavelength apertures. *Reviews of Modern Physics*, **82**, 729 (2010).

[63] Ruan, Z. and Qiu, M. Enhanced Transmission through Periodic Arrays of Subwavelength Holes: The Role of Localized Waveguide Resonances. *Physical Review Letters*, **96**, 233901 (2006).

[64] Zhang, S., Fan, W., Panoiu, N.C., Malloy, K.J., Osgood, R.M., and Brueck, S.R.J. Optical negative-index bulk metamaterials consisting of 2D perforated metal-dielectric stacks. *Optics Express*, **14**, 6778 (2006).

[65] Navarro-Cía, M., Beruete, M., Agrafiotis, S., Falcone, F., Sorolla, M., and Maier, S.a. Broadband spoof plasmons and subwavelength electromagnetic energy confinement on ultrathin metafilms. *Optics express*, **17**, 18184 (2009).

[66] Sainidou, R. and Garc, F.J. Plasmon guided modes in nanoparticle metamaterials. *Optics Express*, **16**, 229 (2008).

[67] Wu, J.J. Subwavelength Microwave Guiding by Periodically Corrugated Strip Line. *Progress in Electromagnetics Research*, pages 113–123 (2010).

[68] Rehwald, S., Berndt, M., Katzenberg, F., Schwieger, S., Runge, E., Schierbaum, K., and Zerulla, D. Tunable nanowires: An additional degree of freedom in plasmonics. *Physical Review B*, **76**, 085420 (2007).

[69] Hibbins, a.P., Hendry, E., Lockyear, M.J., and Sambles, J.R. Prism coupling to 'designer' surface plasmons. *Optics express*, **16**, 20441 (2008).

[70] Shelby, R.a., Smith, D.R., and Schultz, S. Experimental verification of a negative index of refraction. *Science (New York, N.Y.)*, **292**, 77 (2001). 7

[71] Sievenpiper, D. *High-Impedance Electromagnetic Surfaces*. Ph.D. thesis, University of California (1999). 7, 18, 26, 68

[72] Colin, R. *Field Theory of Guided Waves*. Wiley, New York, second edition (1990). 7

[73] Reitz, J., Milford, F., and Christy, R. *Foundations of Electromagnetic Theory*. Addison-Wesley, New York, fourth edition (1993). ISBN 0201526247. 7

[74] Neviere, M. and Popov, E. Electromagnetic resonances in linear and nonlinear optics : phenomenological study of grating behavior through the poles and zeros of the scattering operator. *Journal of Optics*, **12**, 513 (1995). 7, 34

[75] Hansen, R.C. and Hougardy, R. Scanning Surface Wave Antennas-Oblique Surface Waves Over a Corrugated Conductor. *IRE Trans. Antennas and Propagation*, **AP-6**, 370 (1958). 13

[76] Floquet, G. Sur les équations différentielles linéaires à coefficients périodiques. *Annales de l'École Normale Supérieure*, **12**, 47 (1883). 13

[77] Collin, R.E. *Field Theory of guided Waves*. Wiley, New York, second edition (1991). ISBN 0879422378. 16

[78] Zhu, B.O., Zhao, J., and Feng, Y. Active impedance metasurface with full 360 reflection phase tuning. *Scientific reports*, **3**, 3059 (2013). 16, 105

[79] Chu, T.s. and Kouyoumjian, R. Surface wave diffraction by a wedge. *IEEE Transactions on Antennas and Propagation*, **13**, 995 (1965). 31

[80] Chu, T.s. and Kouyoumjian, R.G. Scattering of a Surface Wave by a Discontinuity in the Surface Reactance on a Right Angled Wedge *. *Communications on Pure and Applied Mathematics*, **XIV**, 35 (1961). 67, 75

[81] Chu, T.s. and Karal, F. The Diffraction of Surface Waves by a Terminated Structure in the Form of a Right-Angle Bend. *IRE Transactions on Antennas and Propagation*, **14**, 679 (1962). 16, 31, 67, 105

[82] Tiberio, R. and Pelosi, G. High-frequency scattering from the edges of impedance discontinuities on a flat plane. *IEEE Transactions on Antennas and Propagation*, **31**, 590 (1983). 18

[83] Kittel, C. *Introduction to Solid State Physics*. Wiley, New York (1996). 18

[84] Parker, E.A. The Gentleman's Guide to Frequency Selective Surfaces. *Electronic Engineering*, pages 1–18 (1991). 24

[85] Marcuvitz, N. *Waveguide Handbook*. Peregrins, Stevenage, U.K. (1986). 25

[86] King, R., Thiel, D., and Park, K. The Synthesis of Surface Reactance Using an Artificial Dielectric. *IEEE Transactions on Antennas and Propagation*, **AP-31**, 471 (1983). 27

[87] Carne, A. and Brown, J. Theory of Reflections for the Rodded-Type Artificial Dielectric. *Radio and Telecommunication Section*, pages 107–114 (1958). 27

[88] Drude, P. Zur Elektronentheorie der Metalle. *Annalen der Physik*, **306**, 566 (1900). 27

[89] Voronko, A., Klimova, L., and Shkerdin, G. Reflection of Surface Polaritons at a Dielectric Barrier. *Solid State Communications*, **61**, 361 (1987). 31

[90] Marko, P. Propagation of surface plasmons through planar interface. *Metamaterials, proc. SPIE*, **7353** (2009). 31

[91] Rupert, F. and David, F.P. Scattering of Surface Plasmon Polaritons at Abrupt Surface Discontinuities : Implications for Nano-Scale Cavities. *The American Physical Society* (2007). 31

[92] Rojas, R.G. Wiener-Hopf analysis of the EM diffraction by an impedance discontinuity in a planar surface and by an impedance half-plane. *IEEE Transactions on Antennas and Propagation*, **36**, 71 (1988). 31

[93] Jamid, H. and Al-Bader, S. Reflection and transmission of surface plasmon mode at a step discontinuity. *IEEE Photonics Technology Letters*, **9**, 220 (1997). 31

[94] Maradudin, A.A., Wauis, R.F., and Stegeman, G.I. Surface Polariton Reflection and Transmission at a Barrier. *Solid State Communications*, **46**, 481 (1983). 31

[95] Stegeman, G.I., Maradudin, A.A., Shen, T.P., and Wallis, R.F. Refraction of a surface polariton by a semi-infinite film on a metal. *Physical Review B*, **29** (1984). 31

[96] Ansoft. Ansoft HFSS (1970). 33, 58

[97] Bao, G., Cowsar, L., and Masters, W.e. *Mathematical Modelling in Optical Science*. Society for Industrial and Applied Mathematics (1987). ISBN 0898714753. 34

[98] Humphries, S. *Finite-Element Methods for Electromagnetics*. John Wiley, New York (1990). ISBN 0-8493-1668-5. 34

[99] Applications, T. and Treatment, H. Microwave Absorption Of Carbon Black And Carbonyl Iron Composites With Polychloroprene. *Technology*, **45**, 415 (2006). 37

[100] Baker-Jarvis, J., Vanzura, E., and Kissick, W. Improved technique for determining complex permittivity with the transmission/reflection method. *IEEE Transactions on Microwave Theory and Techniques*, **38**, 1096 (1990). 38

[101] Belrhiti, M.D. and Mamouni, A. Complex Permittivity Measurement for Dielectric Materials at Microwave Frequencies Using Rectangular Waveguide. *European Journal of Scientific Research*, **49**, 234 (2011). 38

[102] Cho, H.s. M-Hexaferrites with Planar Magnetic Anisotropy and Their Application to High-Frequency Microwave Absorbers. *IEEE Transactions on Magnetics*, **35**, 3151 (1999).

[103] Fallahi, A., Member, A., Yahaghi, A., Benedickter, H.r., Abiri, H., Shahabadi, M., and Hafner, C. Thin Wideband Radar Absorbers. *Analysis*, **58**, 4051 (2010).

[104] Kasagi, T., Tsutaoka, T., and Hatakeyama, K. Dielectric properties of Permalloy granular composite materials. *Journal of the European Ceramic Society*, **30**, 401 (2010).

[105] Kasagi, T., Tsutaoka, T., and Hatakeyama, K. Negative permeability spectra in Permalloy granular composite materials. *Applied Physics Letters*, **88**, 172502 (2006).

[106] Kazemzadeh, A. Nonmagnetic Ultrawideband Absorber with Optimal Thickness. *IEEE Transactions on Antennas and Propagation*, **59**, 135 (2011).

[107] Kim, S. Magnetic and microwave absorbing properties of CoFe thin films plated on hollow ceramic microspheres of low density. *Journal of Magnetism and Magnetic Materials*, **271**, 39 (2004).

[108] Kim, S.S., Kim, S.T., Yoon, Y.C., and Lee, K.S. Magnetic, dielectric, and microwave absorbing properties of iron particles dispersed in rubber matrix in gigahertz frequencies. *Journal of Applied Physics*, **97**, 10F905 (2005).

[109] Korolev, K., Subramanian, L., and Afsar, M. Complex permittivity and permeability measurements of ferrite powders at millimeter waves. *2005 European Microwave Conference*, pages 3 pp.–1014 (2005). 38

[110] Mazaleyrat, F. Ferromagnetic nanocomposites. *Journal of Magnetism and Magnetic Materials*, **215-216**, 253 (2000).

[111] Tsutaoka, T., Kasagi, T., Nakamura, T., and Hatakeyama, K. High Frequency Permeability of Mn-Zn Ferrite and its Composite Materials. *Le Journal de Physique IV*, **7**, C1 (1997).

[112] Tsutaoka, T. Frequency dispersion of complex permeability in MnZn and NiZn spinel ferrites and their composite materials. *Journal of Applied Physics*, **93**, 2789 (2003).

[113] Tsutaoka, T., Kasagi, T., Hatakeyama, K., and Fujimoto, K. Negative Permeability Spectra of Magnetic Materials. *2008 International Workshop on Antenna Technology: Small Antennas and Novel Metamaterials*, pages 279–281 (2008). 37

[114] Ebara, H., Inoue, T., and Hashimoto, O. Measurement method of complex permittivity and permeability for a powdered material using a waveguide in microwave band. *Science and Technology of Advanced Materials*, **7**, 77 (2006). 38

[115] Weir, W.B. Automatic Measurement of Complex Dielectric Constant and Permeability. *Proceedings of the IEEE*, **62** (1974).

[116] Wolfson, B.J. and Wentworth, S.M. Complex permittivity and permeability measurement at elevated temperatures using rectangular waveguide. *Microwave and Optical Technology Letters*, **38**, 449 (2003).

[117] Wu, M., Yao, X., and Zhang, L. An improved coaxial probe technique for measuring microwave permittivity of thin dielectric materials. *Materials Research*, **1617** (2000).

[118] Haser, U.C. Permittivity Measurement of Thin Dielectric Materials From Reflection-only Measurement Using One-port Vector Networks Analysers. *Progress In Electromagnetics Research*, **95**, 365 (2009).

[119] Baker-Jarvis, J., Janezic, M.D., Grosvenor Jr., J.H., and Geyer, R.G. Transmission Reflection and Short-circuit Line Methods for Measuring Permittivity and Permeability (1993). 38

[120] Pozar, D. *Microwave Engineering*. Wiley, New York, fourth edition (2011). ISBN 9780470631553. 39

[121] Chen, H.Y., Deng, L.J., Zhou, P.H., Xie, J.L., and Zhu, Z.W. Improvement of Surface Electromagnetic Waves Attenuation with Resistive Loading. *Progress In Electromagnetics Research Letters*, **26**, 143 (2011). 39

[122] CHen, H., Zhou, P., Chen, L., and Deng, L. Study on the Properties of Surface Waves in Coated RAM Layers and Mono-Static RCSR Performances of a Coated Slab. *Progress In Electromagnetics Research*, **11**, 123 (2010).

[123] Kittel, C. On the Theory of Ferromagnetic Resoanace Absorption. *Physical Review*, **460** (1948). 39

[124] Saxler, J., Gómez Rivas, J., Janke, C., Pellemans, H., Bolívar, P., and Kurz, H. Time-domain measurements of surface plasmon polaritons in the terahertz frequency range. *Physical Review B*, **69**, 155427 (2004). 40

[125] Otto, A. Excitation of Nonradiative Surface Plasma Waves in Silver by Method of Frustrated Total Reflection. *Zeitschrift fur Physik*, pages 398–410 (1968). 40, 43

[126] Lockyear, M.J., Hibbins, A.P., Sambles, J.R., Hobson, P.a., and Lawrence, C.R. Thin resonant structures for angle and polarization independent microwave absorption. *Applied Physics Letters*, **94**, 041913 (2009). 43

[127] Brock, E.M.G., Hendry, E., and Hibbins, A.P. Subwavelength lateral confinement of microwave surface waves. *Applied Physics Letters*, **99**, 051108 (2011). 43

[128] Alexander, R.W., Kovenor, G.S., and Bell, R.J. Dispersion Curves for Surface Electromagneitc Wave with Damping. *Physical Review Letters*, **32**, 154 (1974). 45

[129] Arakawa, E.T., Williams, M.W., Hamm, R.N., and Ritchie, R.H. Effect of Damping on Surface Plasmon Dispersion. *Physical Review Letters*, **31**, 1127 (1973). 45

[130] Walther, A. *The Ray and Wave Theory of Lenses*. Cambridge University Press (1995). 45

[131] Kweon, G.I. and Kim, C.H. Aspherical Lens Design by Using a Numerical Analysis. *Journal of the Korean Physical Society*, **51**, 93 (2007). 46

[132] Savitzky, A. and Golay, M. Smoothing and Differentiation of Data by Simplified Least Squares Procedures. *Analytical Chemistry*, **36**, 1627 (1964). 50

[133] Garcia-Vidal, F.J., Martin-Moreno, L., and Pendry, J.B. Surfaces with holes in them: new plasmonic metamaterials. *Journal of Optics A: Pure and Applied Optics*, **97** (2005). 55

[134] Rance, H.J., Hamilton, O.K., Sambles, J.R., and Hibbins, A.P. Phase resonances on metal gratings of identical, equally spaced alternately tapered slits. *Applied Physics B*, **95** (2009). 55

[135] Rance, H.J. *Surface Waves on Periodic Structures at Microwave Frequencies*. Ph.D. thesis, University of Exeter (2013). 56

[136] Ruan, Z. and Qiu, M. Slow electromagnetic wave guided in subwavelength region along one-dimensional periodically structured metal surface. *Applied Physics Letters*, **90**, 201906 (2007). 57

[137] Farahat, A.E., Hussein, K.F.A., and El-Minyawi, N.M. Spatial Filters for Linearly Polarized Antenns Using Free Standing Frequency Selective Surface. *Progress in Electromagnetics Research*, **2**, 167 (2008). 99

[138] Govindaswamy, S., East, J., Terry, F., Topsakal, E., Volakis, J.L., and Haddad, G.I. Frequency-selective surface based bandpass filters in the near-infrared region. *Microwave and Optical Technology Letters*, **41**, 266 (2004).

[139] Ünal, E., Gökçen, A., and Kutlu, Y. Effective Electromagnetic Shielding. *IEEE Microwave Magazine*, pages 48–54 (2006). 99

[140] a.V. Osipov and a.N. Norris. The Malyuzhinets theory for scattering from wedge boundaries: a review. *Wave Motion*, **29**, 313 (1999). 105

[141] Patel, A.M. *Controlling Electromagnetic Surface Waves with Scalar and Tensor Impedance Surfaces*. Ph.D. thesis, University of Michigan (2013).

[142] Mattiucci, N., Bloemer, M.J., Aközbek, N., and D'Aguanno, G. Impedance matched thin metamaterials make metals absorbing. *Scientific reports*, **3**, 3203 (2013). 105

[143] Kim, K.J., Kim, J.E., Park, H.Y., Lee, Y.H., Kim, S.H., Lee, S.G., and Kee, C.S. Propagation of spoof surface plasmon on metallic square lattice: bending and splitting of self-collimated beams. *Optics Express*, **22**, 4050 (2014). 111